Attosecond real time observation of ionization and electron-electron interactions

Martin Schultze

München 2008

Attosecond real time observation of ionization and electron-electron interactions

Martin Schultze

Dissertation
an der Fakultät für Physik
der Ludwig-Maximilians-Universität
München

vorgelegt von
Martin Schultze
aus Wippershain

München, den 19.04.2008

Gutachter: 1. Prof. F. Krausz

                 2. Prof. E. Riedle

Tag der mündlichen Prüfung: 30.06.2008

Wie manchen Tag hab ich, wie manche schöne Stunden
Erfindungen geweiht und selber nichts gefunden

G.C. Lichtenberg

Nobody knows where it comes from, but it's probably quantum

Lord H. Vetinari

Eine Woche im Labor kann einem leicht einen Nachmittag in der Bibliothek ersparen

H. Schröder

Contents

Zusammenfassung

Der Austausch von Elementarladungen zwischen atomaren Systemen ist der grundlegende Prozess jeder chemischen Reaktion. Wie sich aus einzelnen Atomen basierend auf diesem Ladungstransfer Moleküle und letztendlich die uns umgebende Welt formen, ist seit den Anfängen der Wissenschaft eine Kernfrage. Wegen der enormen Geschwindigkeit, mit der diese Prozesse ablaufen, sind bisherige Untersuchungsmethoden darauf angewiesen, Ausgangs- und Endzustand zu vergleichen und über die zeitliche Entwicklung des Prozesses, der zum Endzustand geführt hat zu mutmaßen.

Diese Dissertation beschäftigt sich mit Methoden, die einen Einblick in den zeitlichen Ablauf der Ladungsmigration in Atomen ermöglichen. Sie ermöglichen es, ein fundamentales Verständnis der beteiligten Prozesse zu entwickeln und Vorhersagemodelle für den Ablauf chemischer Prozesse dramatisch zu verbessern.

Die Verwendung von Kurzpulslasern, auf der alle hier vorgestellten Techniken beruhen, ist aus zwei Gründen naheliegend: Zum einen ist die Wechselwirkung von Elementarladungen mit elektrischen Feldern präzise analytisch zu erfassen, was zur Interpretation der gewonnen Meßdaten unerläßliche Voraussetzung ist. Andereseits sind die nur noch wenige Feldoszillationen umfassenden, sichtbaren Lichtpulse moderner Kurzpulslaser die kürzesten reproduzierbar erzeugbaren Signale und somit prädestiniert zur Untersuchung ultraschneller Prozesse. Basierend auf der Frequenzkonversion hochintensiver Laserpulse in Strahlung im extremen ultravioletten Spektralbereich (XUV), einhergehend mit einer weiteren Verkürzung der Pulsdauern, wurden im Rahmen dieser Arbeit eine Reihe von Untersuchungen zur Ladungsträgermigration in Atomen unternommen, die im folgenden kurz zusammengefasst sind:

- Tunnelzeit: Die in Kapitel 4.1 vorgestellte Messung untersucht das laserinduzierte Tunneln eines Elektrons aus dem Bindungspotential des Atomkerns. Die Messung bestimmt eine Obergrenze für die Zeit, die ein Elektron benötigt, um unter dem Einfluß eines starken elektrischen Feldes den Bereich, in dem der Atomkern anziehend wirkt, zu verlassen.

- Der kürzeste Laserpuls: Die Zeitauflösung der Messtechnik ist durch die Dauer des kürzesten verfügbaren Laserpulses bestimmt. Kapitel 3.4 und 3.5 beschäftigen sich mit Experimenten, an deren Ende die Entwicklung einer zuverlässigen, intensiven Quelle für die küzesten, laserartigen Röntgenlichtpulse steht. Die Pulsdauer beträgt nur noch 80 Attosekunden, 80 x 10^{-18} Sekunden.

- Dynamik der Elektronenhülle: Nach dem Entfernen eines Ladungsträgers aus der ein Atom umgebenden Elektronenhülle konfiguriert sich das Ensemble der verbleibenden Elektronen neu. Diese Prozesse können sehr komplex und mit dem Verbleib einzelner Elektronen in angeregten Zuständen verbunden sein. Kapitel 4.2 stellt die erste Messung vor, die den Zeitverlauf einer solchen Anregung aufzuklären versucht.

- Laserionisation: Die Entfernung mehrer Elektronen aus der Hülle eines Atoms, die Mehrfach-ionisierung, wird in Kapitel 4.3 mit einer neuartige Technik untersucht, die zum ersten Mal erlaubt, die Entwicklung zu höheren Ladungszuständen in Abhängigkeit einer wohldefinierte Intensität zu verfolgen. Nahezu die gesamte sichtbare Materie im Universum ist ionisiert (Plasma), die Untersuchung des Ionisationsvorganges berührt deshalb fundamentale Fragen der Physik.

Die im Rahmen dieser Dissertation entstandenen Veröffentlichungen sind im Anhang aufgeführt.

Abstract

The exchange of elementary charges between atomic systems constitutes the basic process of any chemical reaction. The question, how molecules and finally the world surrounding us is formed based on this charges transfer, is a driving force since the beginning of science. Due to the enormous speed that characterizes those processes, the methods to investigate them so far where restricted to comparing the initial and the final state of the system and had to guess the interim evolution.

This thesis focuses on methods which allow investigating the temporal evolution of charge-transfer inside atoms. Based on them, it is possible to develop a better understanding of the involved processes and to improve the theoretical models describing them.

Employing short-pulse lasers for such studies is advantageous for two reasons: First of all, the interaction of charged particles with electric fields is well understood, facilitating the analysis and interpretation of the acquired data. Secondly, modern short-pulse laser sources emit pulses that merely comprise 1.5 field cycles of visible light. They are therefore sources for the routine generation of the shortest controllable signals and thus ideal tools for the investigation of ultrafast processes. Based on the frequency conversion of high-power laser pulses by high-order harmonic generation, the spectral extent of the light is shifted into the extreme ultraviolet (XUV). This shift is accompanied by an additional shortening of the pulse duration and enables a series of experiments regarding the charge transfer in matter that where performed in the framework of this thesis.

- Tunneling-time: Chapter 4.1 introduces a measurement that aimed on investigating the laser induced tunneling of an electron through the potential barrier formed by the atomic core. The Measurement defines an upper limit for the time it takes the electron to leave the attractive potential of the atom in the presence of an external field.

- The shortest Laser pulse: the temporal resolution of the metrological technique is dictated by the duration of the shortest available laser pulse. Chapter 3.4 and 3.5 present developments that led to the demonstration of a source for the routine generation of XUV laser pulses with a duration of only 80 attoseconds.

- Dynamics in the electron sheath: Removing an electron from an atom is in general followed by the rather complex rearrangement of the configuration of electrons remaining bound to the core. These processes can result in electrons occupying an excited final state; chapter 4.2 introduces the first measurement that tries to elucidate the time-dependence of such a process.

- Laser ionization: Multiple ionization induced by intense laser radiation is investigated in chapter 4.3 by means of a new technique that allows testing the evolution towards higher charged states depending on a well defined intensity for the first time. Almost all visible matter in the universe is ionized; the analysis of ionization therefore touches fundamental questions of physics.

The publications emerged in the framework of this thesis are listed in the addendum.

Introduction

Light surrounds us everywhere and information transferred via light constitutes the main part of our perception. Since the first demonstration of a laser some 40 years ago, these sources of coherent light play an important role in science. Based on laser sources, a plurality of effects in atomic and molecular physics has been studied and light-matter interaction in general is a fast growing field with many important implications and applications. The discovery of the photoelectric effect by Einstein opened the field of research that deals with the interplay of matter and light.

After the advent of pulsed laser sources (mode-locking: 1964) the attainable pulse duration decreased and approaches nowadays the ultimate limit of a single field oscillation, which corresponds to ~ 2.5 femtosecond (10^{-15} s) for visible light. During this development, the advances in optical technology opened more and more fields in not only atomic, but also molecular and solid-state physics and, awarded with the Nobel prize to Zewail in 1999, real-time chemistry. Ultrashort laser pulses not only serve scientists as a fast shutter in terms of the sharp temporal confinement, but also feature another characteristic making them interesting for science: they offer unprecedented intensity. Focused short pulse lasers provide electric fields that rival the attractive electrostatic potential that binds electrons to nuclei, and are at the same time fully controllable making them an ideal tool for steering and controlling charge in atoms and molecules.

For many intra-atomic processes, femtosecond temporal resolution is not yet satisfactory. Attosecond science holds the promise to push the available temporal resolution by at least an order of magnitude and allows extending conventional ultrafast spectroscopy and strong-field coherent control from the cycle-averaged to the sub-cycle domain of visible light. Attosecond technology is based on the nonlinear response of atoms exposed to ultra-intense laser fields and is usually described as the absorption of many low-energetic (laser) photons followed by the emission of a single high-energetic photon.

Emitting light confined to short pulses introduced two interesting aspects to the field of time resolved investigations. Firstly, the pulses permit time-resolved studies with an inherent time resolution defined by their duration. Secondly, the recently developed ability to compress the pulses to a duration that is comparable to the oscillation period while keeping the energy contained in the pulse high, allocates an artificially generated electric field of strength comparable to the atomic binding potential.

Chapter 1

Technological prerequisites for attosecond metrology

The expanding applications of ultrafast laser science increasingly demands for the ability to control a variety of parameters of ultrashort laser pulses. The established techniques to adjust the spatial and temporal intensity pulse profile as well as the sweep of the carrier frequency (chirp) across the electric field inherently require diagnostic techniques for ultrashort pulses. Widely proliferated techniques allow for the complete characterization of the envelope and the chirp of the pulses (like demonstrated in section 2.1.2), more extensive techniques ("attosecond streak camera" as presented in 1.3.2) even facilitate the complete reconstruction of the light wave oscillation. Strong field applications that are sensitive to the strength of individual light wave-cycles within the laser pulse rather than to its intensity envelope desire for full control of the optical waveform, even adjustment of the time-dependant polarization state of the pulse field can be required.

Intense ultrashort waveforms of light that can be produced with an exactly predetermined electrical field are essential in laser-driven sources of high-energy attosecond radiation. In particular, the reproducibility of the field in each consecutive laser shot requires the control of the relative timing between the intensity envelope and the carrier field oscillation, the control over the carrier-envelope-phase (CEP). As modern short-pulse laser sources approach the single-cycle regime, the electric field strength of consecutive optical half cycles varies substantially from peak to peak. Given the high nonlinearity of the conversion of visible light into X-ray radiation, the generation of attosecond light pulses in the deep ultraviolet is necessarily very field-sensitive.

Ultrashort visible laser pulses hold the potential to synthesize isolated attosecond pulses and therefore are the basis of attosecond metrology. This chapter is devoted to the development of the theoretical aspects that are connected to the generation (section 1.2) and the measurement (1.3) of attosecond light pulses, chapter 2 introduces the technical realization of a source for ultrashort laser pulses with a precisely controlled evolution of the electric field underneath the intensity envelope.

Atoms in strong fields – the physics of attosecond laser pulses.

Attosecond laser pulses (1 attosecond = 10^{-18} seconds) share important characteristics with laser pulses in the visible spectral range as coherence and temporal and spatial confinement. Their generation mechanism, however, is fundamentally different from a traditional laser that forms pulses by electronic energy decay inside a laser cavity. The generation of attosecond pulses is based on Fourier synthesis of high-order harmonic radiation arising from the interaction of atoms with the strong electric fields procured by ultrashort intense laser sources. Understanding attosecond laser pulses requires the discussion of light-matter interaction, in particular the behavior of atoms in the presence of high-intense ultrashort laser pulses

1.1 Atoms in intense laser fields

With the advent of modern short pulse lasers that, for the first time, permit the generation of electric fields with an enormous strength comparable to the potentials, that bind electrons to the atom's nucleus, many unusual phenomena have been discovered. Laser sources nowadays routinely deliver pulses of femtosecond (10^{-15} seconds) duration at peak powers at the terawatt (10^{12} Watt) level. The focused laser intensity exceeding intra-atomic potentials has opened a new regime of light-matter interaction [1-5]. Laser intensity I [W/cm²] and field-strength E [V/cm] are related as

$$I = \frac{1}{2}\varepsilon_0 c E^2$$

ε_0 permittivity of free space

c speed of light

For hydrogen, the coulomb electric field is about 5×10^9 V/cm, corresponding according to the above formula to an intensity of $\sim 3 \times 10^{16}$ W/cm². The following section summarizes strong field processes at laser intensities of $10^{12} - 10^{16}$ W/cm².

1.1.1 Multi-photon ionization

After the invention of the laser as a source for high-intense and collimated light, multi-photon ionization (MPI) and multi-photon transitions were the first to be investigated [6,7]. Atoms can be ionized by radiation fields even though a single field quantum (photon) has significantly smaller energy then the ionization potential. By absorbing multiple photons, the electron can still be released; the photoelectron spectrum shows a peak at

$$E = n\hbar\omega - I_p .$$

n minimal number of photons needed to overcome I_p

I_p Ionization potential

This scenario is depicted in Fig. 1.1 a. Very accurate theoretical descriptions based on lowest-order perturbation theory were developed. With increasing laser intensity, different experimental phenomena become apparent. The first experimental evidence for the absorption of more photons than needed for ionization [8] showed a heavily structured photoelectron spectrum with peaks separated pursuant to

$$E = (n + s)\hbar\omega - I_p .$$

n minimal number of photons needed to overcome I_p

s number of above threshold photons

Where s denotes the number of photons that were absorbed in excess of the amount needed to ionize the atom. At these intensities around 10^{13} W/cm², perturbation theory breaks down as a clear result of the fact, that binding potential and laser field become comparable in strength.

For ever stronger fields, the influence of the electric field on the intra-atomic structure more and more governs the behavior of the atom, the atomic bound states start to be shifted in an oscillatory way driven by the oscillation of the external electric laser field. The magnitude of this shift known as (dynamic) AC-Stark shift depends on coupling between the atomic states and the light field and becomes larger for weakly bound states. The shift in energy of the bound states can sweep them near to a resonance or even into resonance with the light electric field. The analysis of the rather complex experimental signature of this fact can be found for the example of Hydrogen in [9].

1.1.2 Tunnel ionization and barrier suppression

Higher laser intensities cause a dramatic distortion of the atomic potential such that a potential barrier is formed featuring a local maximum called the saddle point (Fig. 1.1 b). If the laser field frequency is low enough, the electron can escape from the atom by tunneling through the potential barrier. The tunneling ionization rate is usually treated in the framework of the quasi-static strong field approximation; there are two main analytical approaches to calculate the ionization rates: Keldysh-like theories [10, 11, 12] and Ammosov-Delone-Krainov (ADK) theories [13]. The latter includes the effect of the Coulomb potential and therefore leads to better agreement of the calculated data with experimental results in the tunneling regime [14].
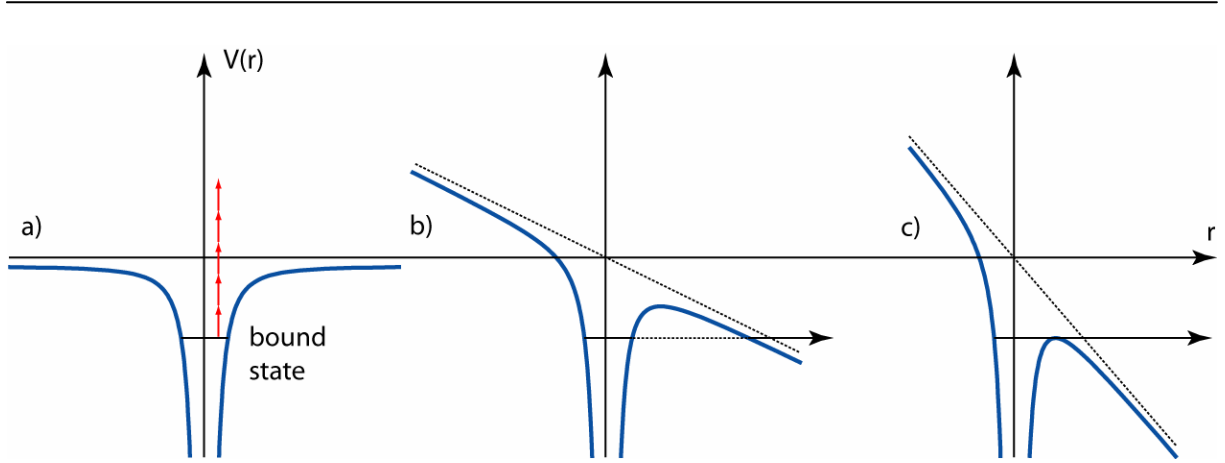
Figure 1.1: Photo ionization mechanisms in the presence of a strong laser field. The blue curve represents the atomic binding potential (Coulomb potential) in the presence of a static electric field as a function of the distance between electron and atomic core (all three panels). With increasing laser intensity, the atomic potential gets more and more distorted and the dominant ionization process evolves from (a) multi-photon-ionization at intensities up to 10^{14} W/cm² to (b) tunnel-ionization at an intermediate intensity range up to 10^{15} W/cm². Panel (c) shows the behavior for intensities, where the electric field of the laser not only rivals but overcomes the atomic binding potential, referred to as over-barrier-ionization. This regime usually sets in only for intensities exceeding 10^{15} W/cm². For a laser pulse, the distortion of the binding potential is dynamic and oscillates with the period of the light field. The black dotted lines represent the linear potential exerted by the laser field on the electrons. The dotted arrow in panel (b) suggests, that the electron has to overcome the attractive potential before finally being ionized (tunneling).

Chapter 4.1 discusses the first time-resolved experiment investigating the time evolution of tunneling ionization. The retrieved upper limit for the "tunneling-time" of 380 as (< 0.2 laser field oscillations) justifies in first order the quasi-static-approximation.

Finally, for intensities exceeding a certain limit (Fig. 1.1 c), the potential barrier is lowered until the ground state is no longer bound. This regime enables the so-called over-the-barrier ionization. The critical field for the inset of this scenario is obtained by equating the saddle-point energy induced by the laser field to the electron binding energy in the ground state. The corresponding intensity is found to be

$$I_c = 4 \times 10^9 \frac{I_p^{\,4}}{Z^2} \qquad\qquad \text{Z charge state of the atom}$$

For rare gas atoms, this value is around 10^{15} W/cm² in the ground state. The work of Keldysh introduced an adiabacity parameter to distinguish the relevant ionization processes. It is expressed (for a definition in SI-units see introductory part of chapter 4.1) by

$$\gamma = \sqrt{\frac{I_p}{2U_p}}$$

Where U_p is the cycle averaged kinetic energy of a free electron oscillating in an electric field of intensity I:

$$U_p = \frac{e^2 E^2}{4m\omega^2}$$

e electron charge

E amplitude of the electric field

m electron mass

ω laser field angular frequency

This quantity is known as the *ponderomotive energy* and, measured in electron volts, it becomes $U_p \sim 10^{-14}$ I [W/cm²] λ^2 [μm]. The Keldysh parameter ascertains multi-photon ionization to be dominant for $\gamma > 1$ where the intensity is low and/or the frequency is high, while for a high-intensity / low frequency laser field ($\gamma < 1$) tunnel-ionization prevails.

In real experiments the ionization rate is integrated over the laser pulse time evolution and the spatial distribution in the interaction region. Current understanding predicts that the target atoms can be depleted before the laser field fully vanishes, and therefore prognoses a saturation of the ionization process. Chapter 4.4 addresses ongoing experimental studies to overcome the limitations arising from the spatial integration over a detection volume that typically is larger than the laser focus and therefore contains a vast range of intensities. For long pulses in the ps-range the intensity rise is so slow, that usually saturation sets in before the pulse envelope reaches a value that would permit the initiation of tunnel-ionization and the experimental data are dominated by MPI signature. The strongly nonlinear dependence of the ionization process determines that electrons are preferentially released around the laser electric field oscillation peaks. The emission is temporally confined to a fraction of a half-cycle of the driving laser field; a laser pulse therefore emits electrons only within a certain number of time-intervals corresponding to the number of field cycles that can overcome the ionization potential of the target matter (Fig. 1.2).
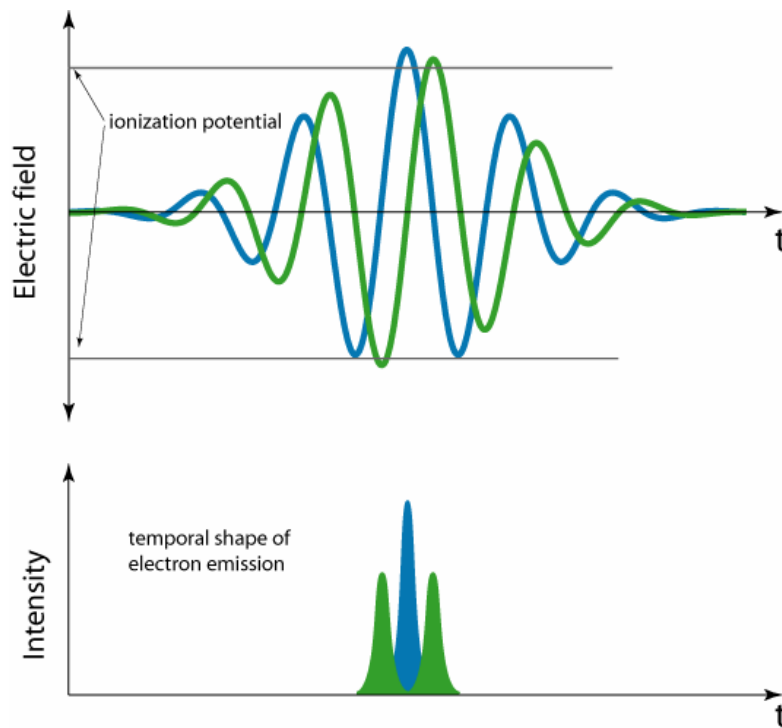
Figure 1.2: Electron release in the tunnel-ionization regime. Due to the highly nonlinear intensity dependence, tunnel-ionization takes only place around the maxima of the electric field of a laser pulse. Here a situation is depicted where field-strength rivals the ionization potential only once (blue) or twice (green case). The two cases represent two different settings of the carrier-envelope phase, namely a cosine-like pulse as the blue line and a sinusoidal pulse as the green line, but for the same temporal width and energy of the laser pulse. The electron emission is temporally confined to short intervals around the field maxima. For the ideal conditions suggested here, electron emission takes only place once for a cosine-like pulse, electron recolliding with the parent ion would therefore emit only a single burst of high-harmonic radiation (see text).

As 800 nm, the central wavelength for Ti:Sapphire lasers that are most widely used as high-power short pulse sources, corresponds to a period of 2.7 fs, the temporal width of a wavepacket released via tunneling ionization can be shorter then 1 femtosecond, thus entering the attosecond regime. Once set free, the electron behaves like a free classical charged particle in the presence of an electric field (for a treatment see section 1.3.2). Following the ionization, the electron is strongly accelerated away from the ion and, after half an optical cycle when the electric field changes its sign, the electron is enforced to return. With a rather low but not vanishing probability, the electron returns to the vicinity of its parent ion and is absorbed again into the ground state, whilst its kinetic energy gained during the acceleration in the laser field is emitted as a high-energetic photon. This process is called high-order-harmonic-generation (HHG) and constitutes, if accurately handled, a main tool to achieve the temporal resolution needed for the studies presented here. It is studied in detail in the following chapter. For the

14

sake of completeness, two further processes shall be mentioned: High-order above threshold ionization (HATI), where the released electron is elastically scattered from the ion by absorbing additional ionizing photons. The other process that occurs under the described conditions is non-sequential double ionization, where the returning electron is inelastically scattered from the atom transferring part of its energy to a bound electron, thus promoting the second electron into the continuum.

1.2 Generating attosecond light bursts

Low-order nonlinear frequency conversion processes such as second-harmonic generation, i.e. wave-mixing of the fundamental with the nonlinear dipole response of the interacting medium, leads to the emission of frequency shifted light already at comparably low laser intensities. In contrast to that, high order harmonics result from the highly nonlinear interaction of ultra-intense laser pulses with typically a gaseous target medium [15]. Coherent radiation is emitted at frequencies that are integer multiples of the laser frequency and the shortest wavelength demonstrated so far corresponded to the ~1000th harmonic [16]. Since the atom in the gas phase is inversion symmetric, only odd harmonics of the fundamental are emitted, the total harmonic signal is the coherent superposition of the contribution of different individual atoms interacting at different intensities and phases. After the interaction region, only those harmonics propagate that fulfill the phase-matching condition and therefore interfere constructively. Spectrally, the emission is manifested in a strong fall-off after the first few orders followed by a extended plateau-region where adjacent harmonics have almost constant intensities. The highest energetic part of the spectrum is characterized by a "cut-off" region, where the harmonic structure disappears and the spectral intensity drops linearly. Measured high-harmonic spectra around the cut-off area are shown for example in Fig. 3.5, there the low energetic spectral part is filtered out.

1.2.1 High-order harmonic generation – The three step model

The basic generation mechanism for high-order harmonics is successfully described by the "three-step-model" introduced by Corkum and Kulander and summarized in Fig. 1.3. The three steps including tunnel ionization, the motion of the electron inside the laser electric field and the subsequent recombination with the parent ion are individually addressed in the following part:

• Optical field ionization

As pointed out above, the tunnel ionization rate is only high around the maxima of the field oscillation. Even though, in principle, possible at every instance, for suitable experimental settings the release of electrons is confined to this time intervals. In addition, it is reasonable to believe that the tunneling ionization immediately releases an electron into the continuum. (In fact, this statement does not withstand a rigid investigation; see for example the experimental studies on this in chapter 4.1 and the theoretical framework of this experiment and the discussion about theoretical treatment of "tunneling time" [17,18]. However theoretical models suggest an exponential dependence of the ionization rate on the intensity and therefore indicate an emission in a time interval very much confined around the field peaks; instantaneous to a very good extend)

• Acceleration of the electron inside the laser field

The electron set free with zero initial velocity via tunnel ionization is accelerated away from its parent ion by the laser electric field. It moves along a classical electron trajectory (for mathematical treatment see chapter 1.3.2) in the laser field and as soon as the electric field reverses, the electron is first decelerated and then accelerated back towards its parent ion. Given that the electron is released at a phase setting of the electric field that allows for this trajectory to return to the ionic core, the maximum kinetic energy that can be achieved can be calculated using classical [19] or quantum mechanics [20]. It is given by (the more accurate quantum mechanical treatment introduces a factor of ~1.3 to the ionization potential)

$$E_{cutt-off} = \hbar\omega_{max} = I_p + 3.17U_p.$$

The highest attainable energy is composed by the binding energy of the electron (I_p) and the maximum kinetic energy of the electron upon its return to the core (3.17 U_p). This takes place for a phase of 17° (referring to the oscillation period) close to the highest field oscillation, where also the ionization rate is highest.

• Recombination with the ion

Recombination of the electron with its parent ion can lead to the emission of a broadband extreme-ultraviolet (XUV) photon. One photon per electron is emitted carrying the sum of the ionization potential and the electron's kinetic energy. The recombination event itself is rather unlikely, the conversion efficiency therefore low (~10^{-6} in the cut-off range). From the defini-

tunnel ionization

acceleration in the
laser field

$$h\nu = I_p + W_{kin}$$

recombination and
photoemission
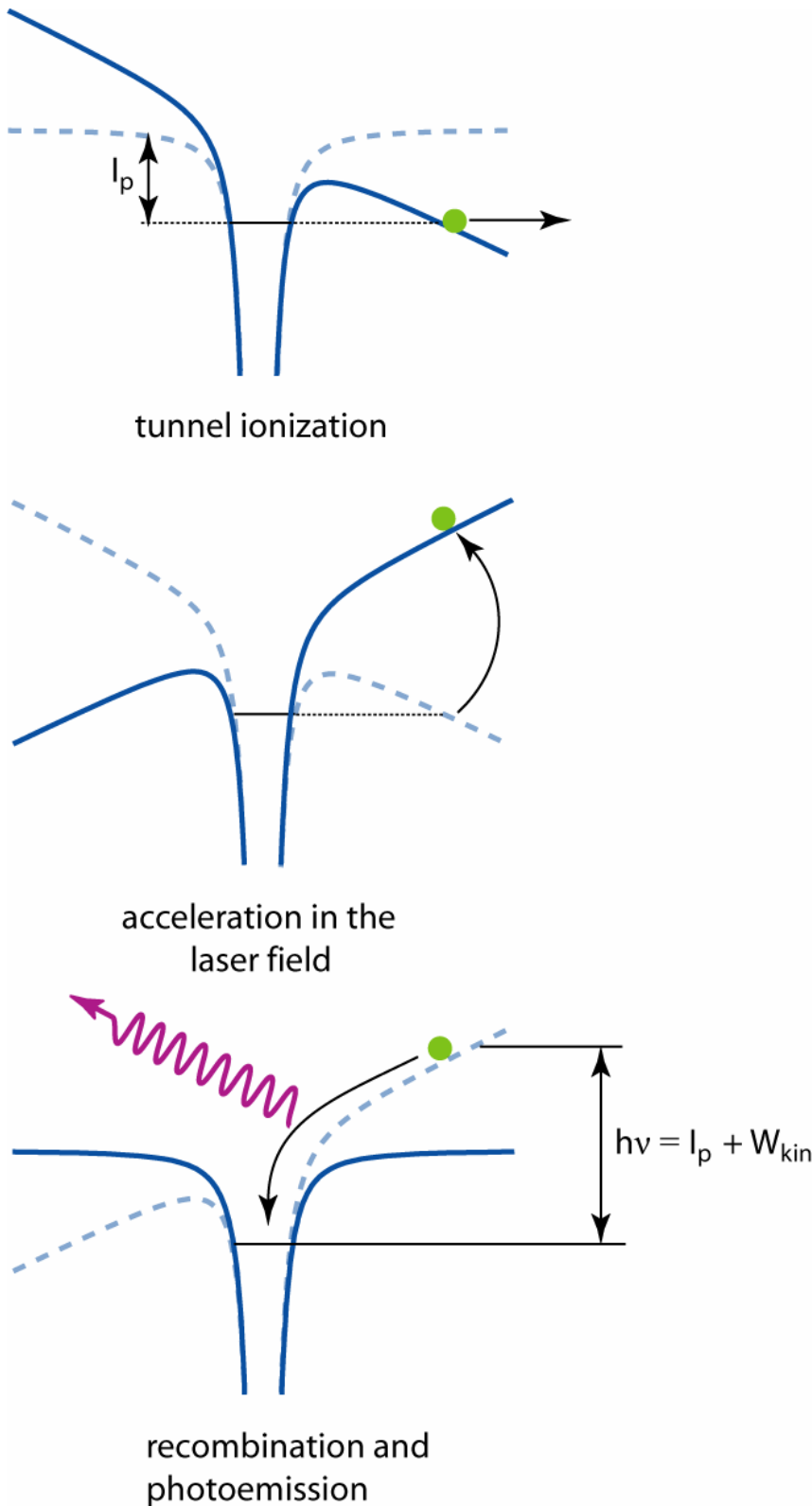
Figure 1.3: Illustration of the three-step-model for high-harmonic radiation. First (upper panel) the laser electric field releases the electron from the atomic attractive potential via tunnel ionization. Then, changing its sign after half a laser period, the electric field accelerates the electron first away from the ion and then back. The lower panel shows the recombination of the electron with the ion and the emission of a high-energy photon. The attainable energy of the emitted photon depends on the ionization potential and the kinetic energy the electron gained during its acceleration in the laser electric field.

tion of the ponderomotive potential above and the estimation for the highest reachable recombination energies it is apparent, that both the laser frequency and intensity determine the cutoff energy. Concluding that a longer driving laser wavelength at the same peak intensity triggers the emission of higher energetic photons led to several attempts to confirm this experi-

mentally [21-24]. Newer experimental results see the generation of high-harmonic-radiation with short wavelengths in favor again [25, 26], as a rule of thumb, the efficiency scales as $1/\lambda^5$, while the cut-off grows according to λ^2. The high photon energies that can be achieved in this process together with the preserved temporal confinement of the emission make high-harmonic generation the ideal source for ultrashort high-energetic XUV bursts. However, the large excursion the electron undergoes to accumulate kinetic energy exceeding the fundamental photon energy several times leads to a substantial spread of the free electron wavepacket reducing the recombination probability drastically. This wavepacket dispersion is estimated by [1, 5] and justifies the little re-absorption probability of the electron as devoted to its quantum nature.

High-harmonic generation exhibits two important features that were neglected up to now: The emission is the superposition of the response of several atoms under influence of several field cycles. In case of multi-cycle laser pulses, the electrons encounter the parent ion every half-cycle of the electric field which results in a series of emissions that manifest themselves in the spectral domain as high harmonic structure. The emission of a single atom can be described as Bremsstrahlung radiation based on the inelastic scattering of an accelerated electron on the heavy nucleus. The single-atom high-harmonic spectrum is thus not expected to exhibit any particular feature.

1.2.2 From attosecond pulse trains to isolated attosecond pulses

Since the generation of high-harmonic radiation is repeated every half-cycle of the laser field, the spectrum consists of odd harmonics of the fundamental (effectively generation takes place with the double frequency $\leftrightarrow$ double spacing in the spectrum; reciprocity of the Fourier transform). Fig. 1.4 shows a schematic view of a high-harmonic spectrum generated with a multi-cycle laser pulse. It is important to notice that for a rather long (>5 fs) driving pulse, the cut-off range shows the harmonic spacing as well. Applying these insights to the time-space it is evident that a discrete HHG-spectrum corresponds to the emission of a train of attosecond pulses [27-30]. Their spacing in time of half a laser period $T/2$ corresponds to the spacing of $2\hbar\omega_{\mathrm{laser}}$ in the spectrum.

In contrast, when a few-cycle laser pulse comes into play, the energy of the emitted wavepackets from consecutive recombination events close to the peak of the pulse can vary substantially.
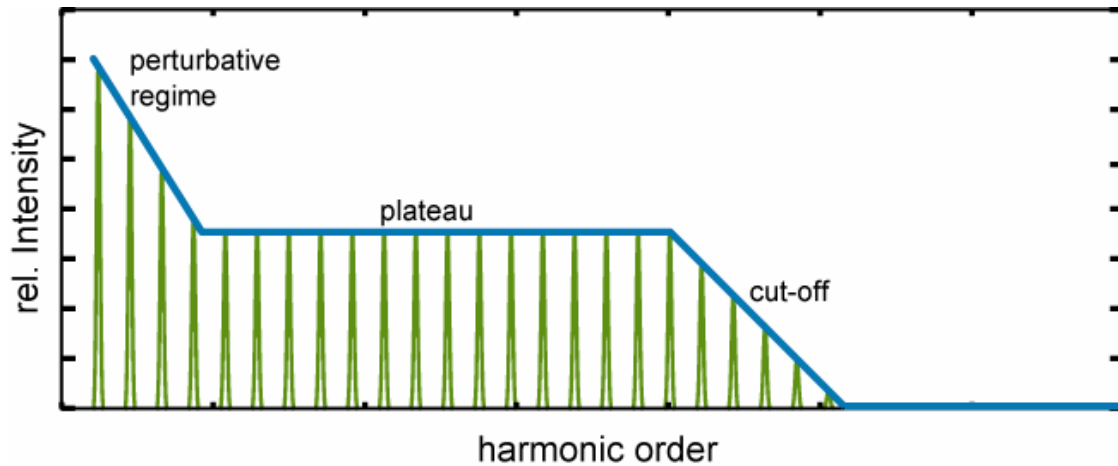
Figure 1.4: Schematic high-harmonic spectrum. The harmonic spacing of twice the fundamental frequency results from the temporal periodicity of high-harmonic emission with half the laser oscillation period. The spectrum is divided into three parts characterized by different ideas: the perturbative regime at low harmonics is characterized by the nonlinear dipole response of the medium. The plateau-region for intermediate harmonic orders arises from the described recollision / reabsorption process and the cut-off radiation at highest orders is only emitted by those electrons that undergo acceleration within the few most intense half cycles of the laser field.

By setting the carrier envelope phase (CEP) of a few-cycle laser pulse such that the field maximum coincides with the maximum of the pulse envelope (resulting in a substantial modification of U_p for consecutive recombination events) - referred to as cosine pulse - it is possible to restrict the emission of the most energetic light wavepackets to take place only once per laser pulse (cp. Fig. 1.3). By contrast, in a sinusoidal-shaped laser field two re-colliding electron wavepackets lead to emission at the highest photon energies, resulting in two XUV bursts separated by half a period of the laser field. A comprehensive description accounting for recent experimental developments of CE-phase related effects on the high-harmonic generation can be found e.g. in [31]. For ever shorter driving pulses, the radiation in the cut-off range of the emitted spectrum can become continuous since it is only generated by one laser half cycle. A prerequisite to enter this regime is not only the ability to generate short laser pulses, but, in addition, their waveform has to be adjusted to be identical for every pulse. The technical aspects of this "phase-stabilization" are addressed in chapter 2.

The shortest available laser pulses, as presented in chapter 3, comprise merely 1.5 cycles of the laser field. The enormous contrast between the amplitude of adjacent field oscillations (max 21% for a 3.5 fs pulse) of these waveforms dictates the formation of the cut-off radiation in a way that substantially differs from the understanding developed for longer driving pulses.

A detailed treatment of the influence of changes in the carrier-envelope phase of almost single cycle driving pulses to HHG radiation is presented in chapter 4.2.

1.3 Measurement of attosecond light pulses

Characterization of attosecond pulses – qualitatively and quantitatively - is a crucial question in experiments that want to make use of the potentially extreme temporal resolution that such pulses can offer. In contrast to the characterization of attosecond pulse trains, identifying the essential parameters of single attosecond light pulses puts stronger demands on the retrieval scheme, both experimentally and numerically. The result of a full characterization of 80 as pulses is given in chapter 4; the following section introduces the underlying idea, the attosecond streak camera.

1.3.1 The streak camera methodology

Conventional streak cameras are used to measure the temporal behavior of optical events at very short time scales. Typically, picosecond resolution can be achieved by these devices, only limited by the ability to generate fast rising voltage ramps and by space charge effects. Fig. 1.5 illustrates the principle of conventional streak cameras, combining ideas used in oscilloscopes (deflection of electrons by a time dependant voltage) and conventional film cameras (relative movement of the exposed spot and the recording medium). Abdicating the ability to resolve one spatial dimension, the time evolution of the motive can be observed instead. Laser light shines on a photocathode generating a photoemission of electrons at the rear side of the cathode. Based on the fact, that the response time of the emission is negligible, the electron emission imitates the temporal and intensity shape of the laser pulse. In Fig. 1.5 two pulses with different amplitude are shown to demonstrate the idea. The generated electrons enter a capacitor where a fast ramping electric field deflects them by an amount depending on their transition time through the capacitor. Assuming the field ramp is faster or at least comparable to the electron bunch duration, the overall lateral displacement of electrons at the trailing edge and electrons at the leading edge of the pulse will be significantly different. The projection of the electrons to a phosphor screen leads to a transversally elongated spot resulting from the effect of the field ramp to the electron bunch. Provided exact knowledge of the tem-

poral evolution and the synchronization of field ramp and electron bunch, the temporal shape of the laser field hitting the photocathode can be traced back by the evaluation of the streaked image, the best temporal resolution presented so far is in the order of several hundreds of fs. The key limitation that prevents the use of similar techniques at shorter time scales is the lack of perfect synchronization between the field ramp and the generated electron replica of the optical pulse. Additional problems arise from space-charge and energy dispersion of the electron bunch.
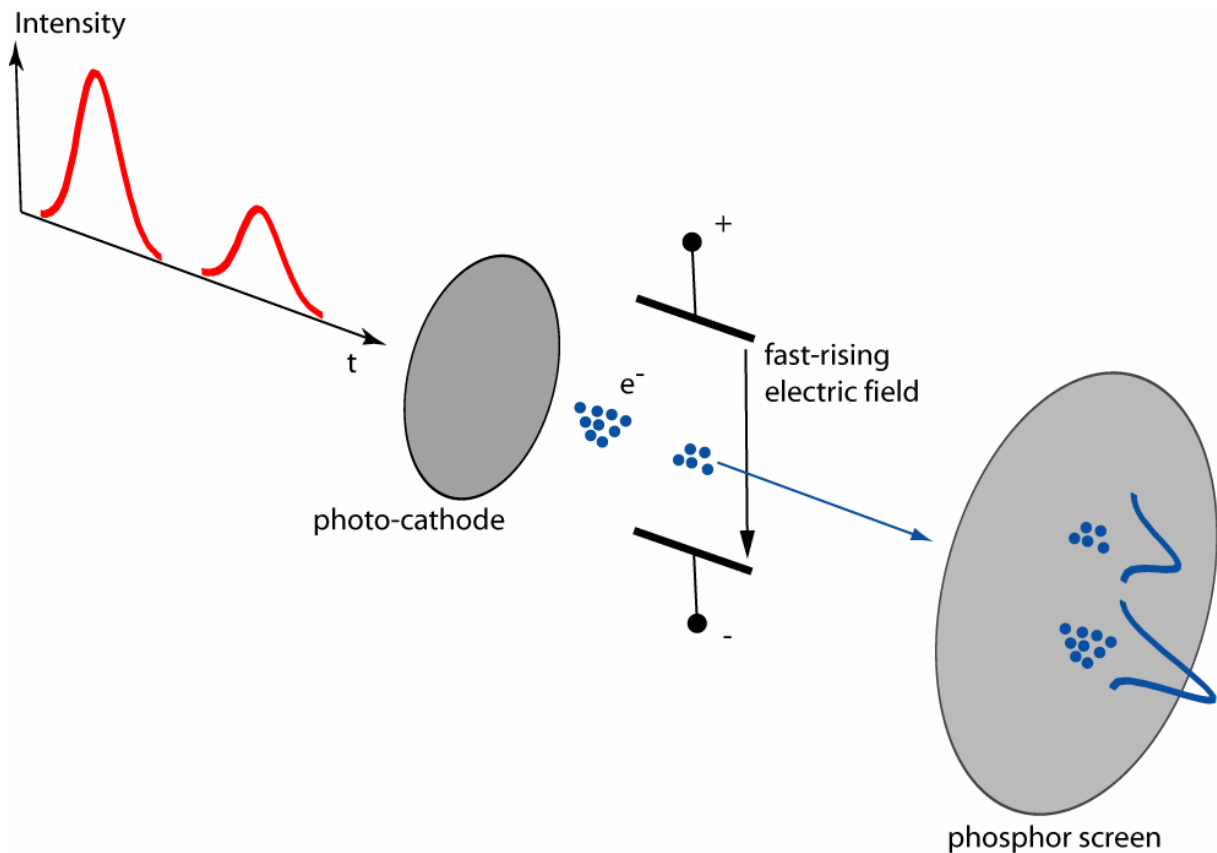

Fig. 1.5: Schematic of a conventional streak camera. Electrons released from a photo-cathode by an impinging laser pulse (here a double pulse to illustrate the working principle) are accelerated towards a phosphor screen. The electron emission imitates the temporal and the intensity profile of the laser pulse. Before hitting the phosphor screen, the electrons pass a capacitor where, synchronized with their traversing, a fast ramping voltage is applied. The electric field formed by this voltage inside the capacitor deflects the passing electrons by an amount depending on the instant they travel through the capacitor. Electrons at the leading or trailing edge of the pulse are deflected non-uniformly, if the voltage rise time is at least comparable to the laser pulse-duration. The phosphor screen acts as a spatially sensitive detector to observe this asymmetry which is directly associated with the pulse duration and intensity evolution of the laser light.

1.3.2 Streak camera on attosecond time-scale

Several limitations have to be overcome to apply similar techniques as presented associated with the conventional streak camera on an attosecond timescale. The necessity to improve the temporal resolution compared to established schemes by at least 3 orders of magnitude, calls for fundamental modifications to make the idea applicable. Corkum [32] proposed the *attosecond streak camera* based on the idea that the field ramp that probes the electron bunch could be formed by the sub-cycle electric field slope of a laser pulse. The initial proposal aimed on the characterization of XUV attosecond pulses that imprint their temporal structure on a bunch of photoelectrons released by ionizing rare gas atoms.

A bunch of photoelectrons exactly imitates the attosecond pulse only, if the cross section for the ionization is uniform over the entire spectral bandwidth of the attosecond XUV pulse and if the photoelectric effect can be considered to be instantaneous. In fact, chapter 4 shows how the first requirement, which is not fulfilled for very short (i.e. broadband) XUV pulses can be overcome and it presents in addition studies on a possible timing in the photo-ionization process. In the absence of resonant processes including auto-ionization and Auger effects, the first condition is fulfilled to a good extent. The experiment relies furthermore on the fact that the light field applied simultaneously to streak the electron bunch leaves the ionization yield of the atoms unchanged.

Provided that an electron bunch can be generated that mimics the temporal structure of the attosecond XUV pulse, the electric field to probe these electrons similar to the streaking field in the conventional streak camera scheme, has to be precisely synchronized to the attosecond electron bunch. An elegant way is to use the same laser pulse to first generate the attosecond XUV pulse and later probe it in an interferometric setup that enables one to control the delay between the two pulses when they are focused into a rare gas target. The technological implementation of such a scheme has interesting features; first of all, the simultaneity of the two pulses is inherent in the generation process. Experimentally, it is furthermore of great importance that both the XUV and the laser electric field are reproducible since a single acquisition is not sufficient to retrieve the desired information about the attosecond pulse. A technical aspect that comes into play in the experiments described here, is the fact that the laser electric field and the attosecond XUV burst feature parallel polarization, hence the laser field does not affect the trajectory of the electrons but rather modifies their final kinetic energy instead. In analogy to record the spatial extend of an electron bunch as presented in the conventional stre-
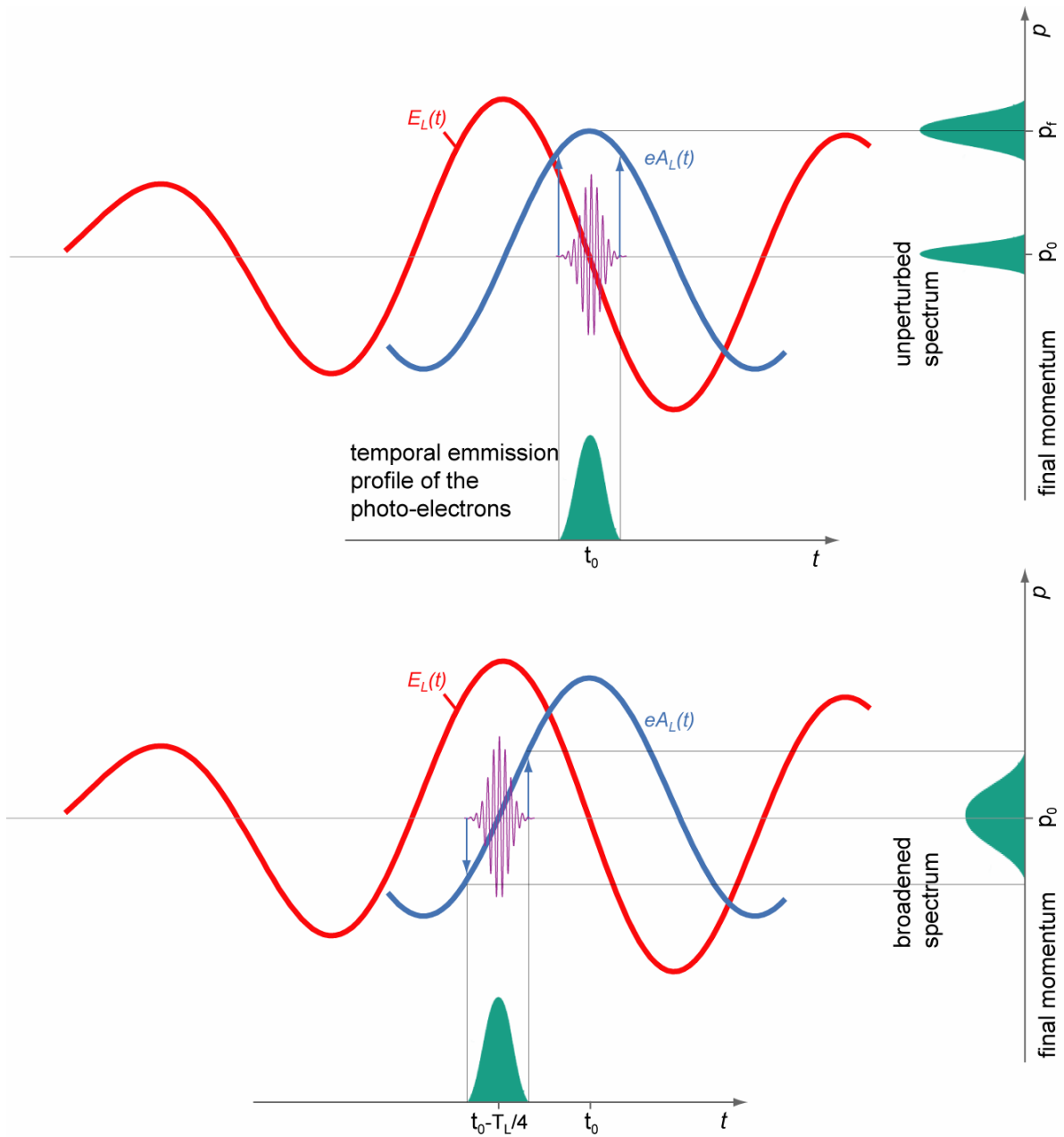
Fig. 1.6: Attosecond streak camera. An attosecond XUV pulse photo-ionizes a rare gas sample and the re-
leased electrons form a bunch with initial momentum distribution according to the green profile that imitates
the temporal characteristics of the XUV pulse. The electron bunch is probed by a laser pulse around a zero-
crossing of its field oscillation (red line). The change in the final momentum distribution of the electron bunch
for this case is depicted in the upper panel. Compared to the unperturbed spectrum, the electron bunch suffers
a shift to higher energies and a slight broadening due to the curvature of the vector potential (blue line). The
lower panel shows the action of the laser field on electrons released around a field maximum. The initial mo-
mentum distribution gets smeared out (broadening) but the central energy is not modified.

ak camera, recording this momentum change gives insight into the impact of the electric field on the electrons. Modern electron energy spectrometers as introduced in chapter 3 provide descent accuracy; recording electron energy instead of spatial deflection therefore appears advantageous.

To investigate the effect of a light field on an electron bunch, it is advantageous to adopt a few useful formulas associated with the motion of a single electron inside an oscillating electric field. Under the assumption, that photo ionization by the XUV pulse and dynamics of the electron in the electric field can be treated independently, a generalization of these equations applies also for a distribution of particles; the treatment is hence applicable for the scenario of the attosecond streak camera.

Integrating the classical equation of motion for the displacement x of an electron with mass m and charge e

$$m\ddot{x} = qE = -qE_L = -qE_a(t)\cos\omega_L t$$

adds up to

$$\dot{x} = -\frac{e}{m}\int_{t_{ion}}^{\infty} E_a(t)\cos(\omega_L t)dt \,.$$

Here $E_L(t) = E_a(t)\cos(\omega_L t)$ is the electric field of the laser oscillating with frequency ω_L. The release instance of the electron t_{ion} represents the moment from which on the electron can be considered not to be affected by the attractive atomic potential anymore, the motion therefore is governed only by the external electric field. It should be noted, that as a consequence of momentum conservation, a free electron suffers no momentum change at all if a full physical waveform is acting on it. Congruously, the integral expression above vanishes for $t_{ion} \to -\infty$. After the end of the pulse and under the adiabatic approximation that postulates a smooth field variation according to $dE/dt \ll E_L\omega_L$, the velocity component that is added to the final velocity of the electron parallel to the electric field is [32]

$$u_L = \frac{e}{m}\frac{E_L(t)\sin(\omega_L t_{ion})}{\omega_L} = \sqrt{\frac{4U_P(t_{ion})}{m}}\sin(\omega_L t_{ion})$$

where the ponderomotive potential U_P comes into play again.
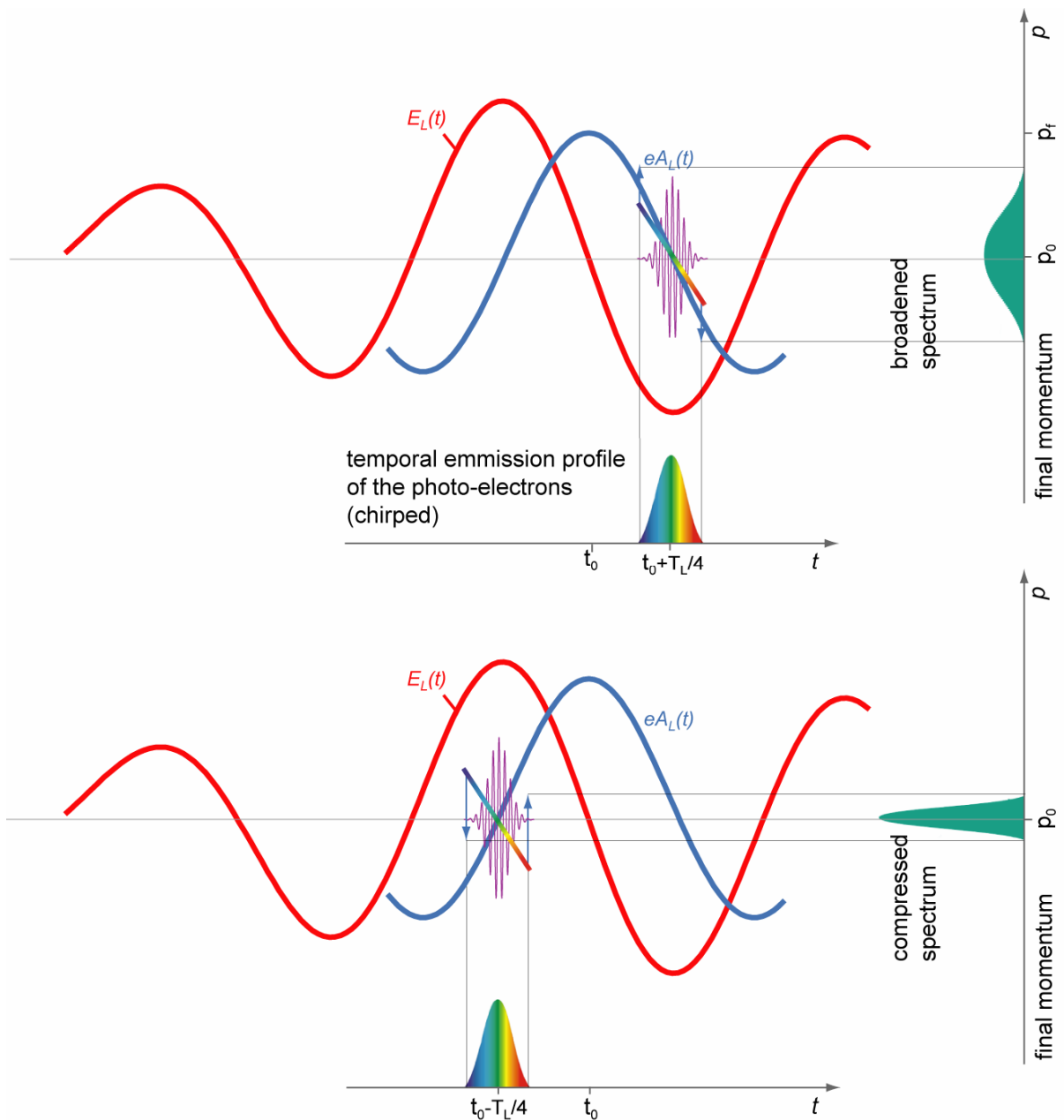
Fig. 1.7: Attosecond streak camera in the presence of (linear) chirp. If the photon energy of the attosecond XUV pulse is changing during its duration (usually referred to as "chirp"), the electron replica released by this pulse subsequent to photo ionization carries this information as chirp of its momentum distribution. The figure shows the influence of this chirp to the resulting momentum distribution for the two most extreme cases. The upper panel considers the emission around a laser field oscillation with slope parallel to the chirp. In this case, the vector potential leads to a broadening of the electron momentum distribution. The opposite case is depicted in the lower panel. Here, the slope of the vector potential counteracts the chirp of the electron bunch and compresses the momentum distribution. In a measured streaking spectrogram with a chirp of the attosecond pulse (i.e. the XUV pulse duration is not Fourier limited), the spectrogram therefore looks asymmetric in the slopes of the streaking field. Chapter 4 compares experimental traces with and without chirp for the first time (asymmetric trace in Fig 3.24).

The final energy W_f can be computed from the initial electron energy W_0 according to

$$W_f = W_0 - U_p(t_{ion}) + U_p(t_{ion})\cos(2\omega_L t_{ion}) + \sqrt{8W_0 U_p(t_{ion})}\sin(\omega_L t_{ion})$$

provided that $\omega_L \ll \omega_{XUV}$ (trivial). W_0 is the excess energy that a XUV photon transfers to the released electron after the ionization potential is vanquished and for the experiments presented here, this energy is always far in excess of the ponderomotive potential; formal: $W_0 > U_P(t_{ion})$. This condition is immediately comprehensible taking into account, that the photon energies of the XUV pulses demonstrated in this thesis are in the range of 90 eV. As a result of the ionization potential of rare gases around 20 eV (Neon 21.6 eV, Helium 24.6 eV) the excess energy carried by the released electrons is therefore in the order of 70 eV. The ponderomotive potential represents the cycle-averaged quiver energy imparted by the laser field to the electron and hardly exceeds 20 eV even for laser electric field strength of 10^{14} W/cm². The total energy change therefore can be written as

$$\Delta W = W_f - W_0 \approx \sqrt{8W_0 U_p(t_{ion})}\sin(\omega_L t_{ion})$$

From the above formula it is apparent that the total momentum oscillates according to a sine function in time, being the oscillation of the light field (cosine) shifted by $\pi/2$. Despite proper normalization, this oscillating function can be recognized as the vector potential of the light field defined as

$$A_L(t_{ion}) = \int\limits_{t_{ion}}^{\infty} E_L(t)dt\,.$$

The integral in the above definition indeed introduces the phase shift of $\pi/2$, the total momentum change Δp therefore can be expressed as

$$\Delta p(\vec{r},t) = e\int\limits_{t_{ion}}^{\infty} E_L(\vec{r},t)dt = eA_L(\vec{r},t_{ion}) = \frac{eE_A(\vec{r},t_{ion})}{\omega_L}\sin(\omega_L t_{ion})$$

The equation dictates that no momentum exchange between the laser electric field and the electron can happen if the electron is not released during the laser pulse. This is a consequence of the fact that free particles do not absorb radiation. The expansion of the above formalism to a bunch of electrons with an intrinsic energy distribution leads to the insight that photo ionization and subsequent electron emission imitates the temporal characteristics of an XUV pulse in terms of the initial momentum distribution of the electron bunch. Detailed

analysis on the applicability of the above introduced concepts to an ensemble of electrons can be found in [32, 33, 34, 35]. The reproduction of the reflections on this topic here does not lead to a better understanding of the process and is therefore disregarded, in particular since the result is intuitive. As already mentioned, the whole technique is based on the fact that the attosecond XUV emission is reproduced by the electron emission subsequent to ionization. Experimentally, the possible influence of space charge effects that would necessarily lead to a dispersion of the electron bunches is effectively excluded because the available sources in combination with the low ionization cross-sections only permit the release of one electron per XUV pulse on average.
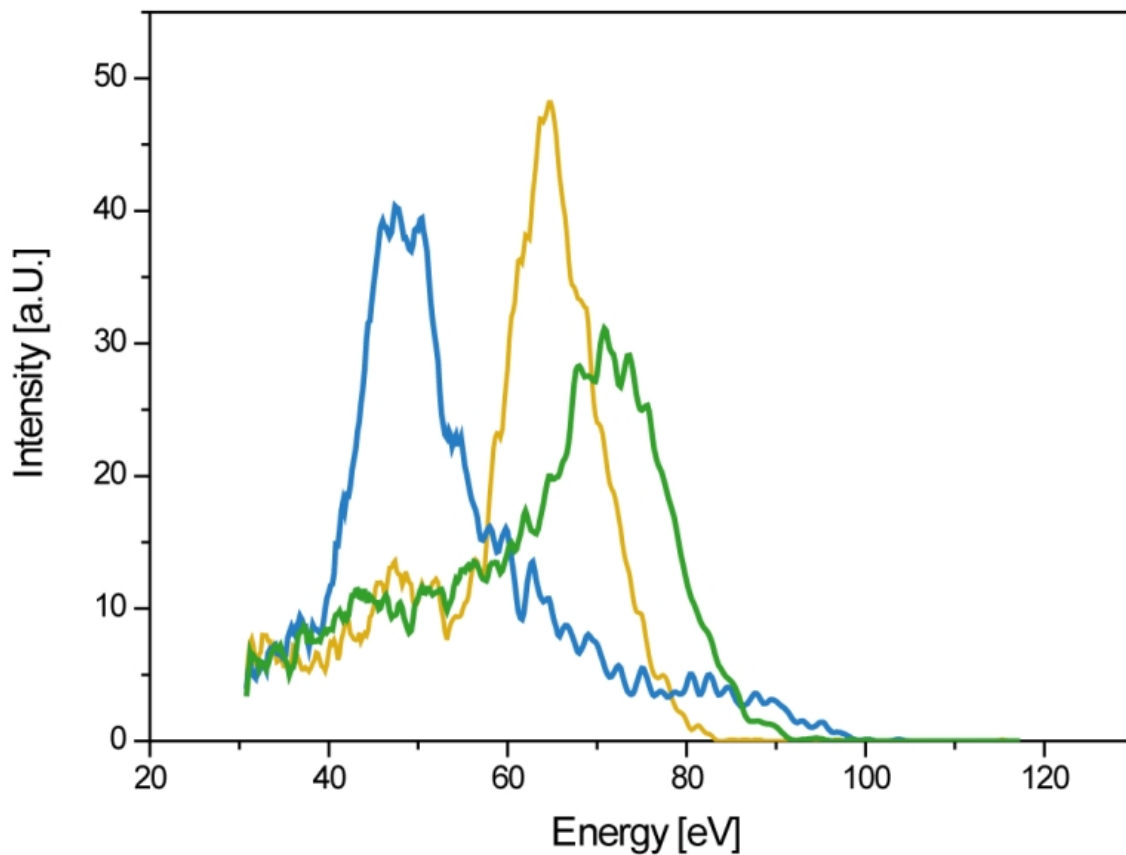
Figure 1.8: Electron spectra in the presence of a streaking field. The yellow curve shows the unperturbed spectrum arising from the photoexcitation. The blue curve is the same spectrum recorded in the presence of a streaking field pointing away from the electron detector and thus decelerating the electrons. The green curve shows the action of a streaking field set such, that the electrons gain momentum after their release, the spectrum is therefore shifted towards higher energies.

1.3.3 Streaking for Fourier limited attosecond pulses

Fig 1.6 illustrates the effect of the laser electric field on an attosecond electron bunch synchronized with the field. It is important that the method only works for electron bunches that are shorter than a half-cycle of the streaking laser field. The figure shows a setting where the electron momentum is observed along the polarization of the laser and distinguishes two cases of the relative timing between electron bunch and laser field oscillation. To support an intuitive picture, from now on only the vector potential will be considered since it is directly proportional to the electron momentum change according to the above calculation. Electrons released at different moments in the laser pulse accumulate different momentum changes (blue arrows in Fig. 1.6). If the electron bunch is synchronized with a zero transition of the vector potential, the corresponding final momentum distribution is broader as compared to the spectrum recorded without applied laser field. If the electron bunch is probed at the consecutive zero transition (shift by π) the broadening is identical to the previous case.

1.3.4 Streaking of chirped attosecond pulses

Fig. 1.7 sketches the case of a chirped attosecond pulse. In the generation process, it is in accordance with the classical picture that the contribution of the different electron trajectories to the formation of the attosecond pulse is not timed but has rather a dependence on the energy of the re-colliding electron and therefore on the energy of the emitted photon. This scenario, referred to as "chirp" leads consequently to a "chirp" or sweep in the energy distribution of the released electron bunch in the streaking experiment. Low energy electrons at the leading edge of the bunch and high energetic ones at the trailing edge as suggested in Fig. 1.7 corresponds to a positive chirp, it has to be mentioned, that this chirp by no means has to be linear as depicted here. In the case of a linear chirp, the arising asymmetry leads to an asymmetric broadening of the final electron momentum distribution when probed at adjacent zero crossings of the vector potential. Fig. 1.7 points out this asymmetry. In Fig. 1.8, two streaked electron spectra are shown besides a spectrum recorded without any laser field applied. The shift in central energy and the deformation of the spectra is clearly visible; all streaking spectrograms shown in this work are based on such flight-time spectra. Fig. 3.24 shows the experimental evidence of this idea. In fact, the experimental implementation allows concluding on the temporal chirp of the attosecond XUV pulse from a measurable parameter. In the same way as for a linear chirp, the experimental trace bears the information about higher order chirp in terms of asymmetric distortions of the electron spectra under the influence of a laser

light field. In the opposite sense, the absence of a chirp evident in a measured trace by a symmetry of the recorded spectra at adjacent zero crossings of the vector potential allows to conclude that the attosecond emission is close to the Fourier limit within the boundaries of experimental resolution. This information justifies to safely estimate the duration of the attosecond XUV pulse by calculating the inverse Fourier transform of the field free momentum distribution (bandwidth) of the electron bunch.

Chapter 3.5 introduces a more sophisticated way to retrieve information about the temporal shape of the attosecond pulses and the spectral and temporal phase. Based on a retrieval algorithm similar to frequency resolved optical gating in the visible domain, both the XUV pulse and the laser pulse are fully characterized. The algorithm allows allocating an error on the retrieved data and enables to identify the chirp inherent to the emission process of the high-harmonic radiation. Based on this information, by introducing filter material with the proper dispersion, a further temporal compression of the attosecond pulse can be achieved.

An introduction to alternative measurement techniques making use of the unprecedented temporal resolution of isolated attosecond pulses is given in combination with the experimental results in chapter 4.1 (Attosecond Tunneling Spectroscopy) and 4.2 (Attosecond Streaking Spectroscopy).

Chapter 2

Absolute phase controlled few-cycle pulses

Experiments on the attosecond timescale, particularly those utilizing the generation of high harmonic radiation, are necessarily very sensitive to the overall waveform of the driving laser field. As described in the previous chapter, the measurement and the precise and reproducible control of the carrier envelope phase, or, more general, the waveform of the laser pulses is the key aspect of the laser sources employed in the experiments. The shorter the laser pulses are, the stronger effects of changes in the carrier envelope phase emerge in the experiments.

2.1 The laser system

Detailed descriptions of the laser source employed can be found in [36, 37]. This chapter gives a survey over the general characteristics and capitalizes on the obtained improvements in the course of this work. To achieve the few cycle NIR pulses needed for the experiments presented a modified version of the commercially available chirped-pulse-amplification system (Femtopower Compact Pro, Femtolasers Produktions GmbH) was employed. The Amplifier system is seeded by an ultra broadband Ti:Sapphire oscillator, emitting pulses of about 6 fs with an output power of 300 mW at 78 MHz [38]. To obtain the error signal needed for the phase stabilization (section 2.2) the oscillator pulses are focused into a periodically poled crystal that broadens the spectrum and generates the difference frequency simultaneously (section 2.2.2) [39]. For seeding the amplifier (seed power ~1 nJ) the oscillator pulses are dispersively stretched to 15 ps in bulk material and then amplified to 1.2 mJ / 3 kHz in 9 passes through a Ti:Sa crystal pumped with ~24 W / 3 kHz at 532 nm. Subsequent recompression takes place in a hybrid prism- / positive dispersive mirror-compressor. The prism compressor is modified to overcompensate the positive chirp of the amplified pulses, therefore the pulses maintain their negative chirp throughout the final prism and are not object to self-phase modulation (SPM) which would cause a narrowing of the spectrum. The full compression takes place by reflection on positive dispersive chirped mirrors where SPM does not occur. Thereby, sub-25 fs pulses (full-width at half maximum FWHM) extending over a spectral width of 61 nm and energy of 900 μJ [40] are achieved. The carrier-envelope-phase stabiliza-

tion mandatory for the performed experiments is realized by branching of approximately 4% of the amplified pulses after the chirped mirror compressor that are sent into a collinear f-2f interferometer (chapter 2.2.3) that serves as phase-monitor and for the feedback loop of the phase-stabilisation. Fig. 2.1 shows the layout of the oscillator / amplifier system.
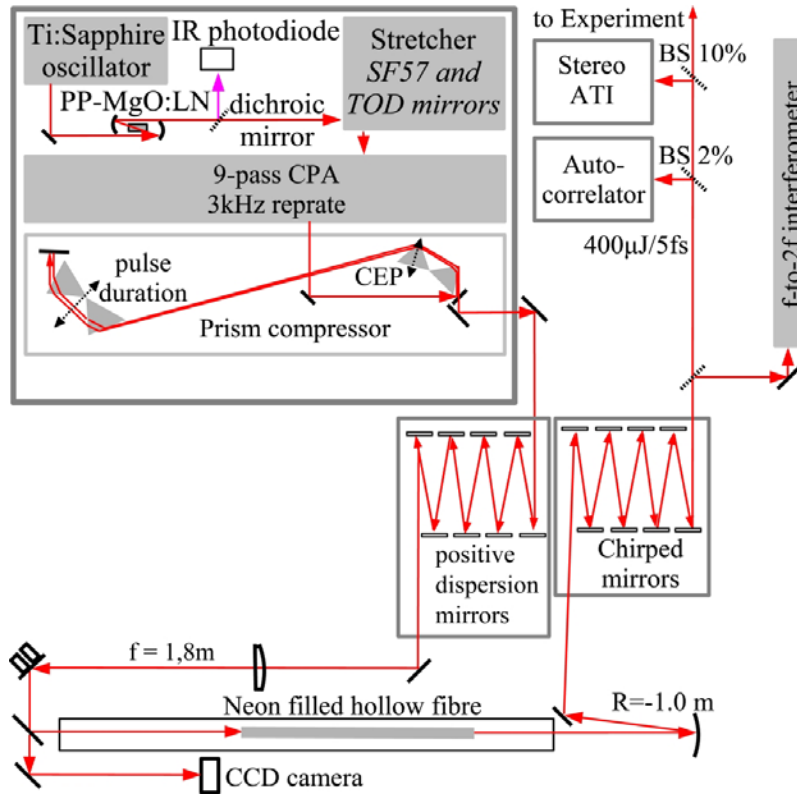

Fig. 2.1: Laser setup schematic. The Ti:Sapphire oscillator generates 6 fs pulses with 320 mW of average power at a repetition rate of 78 MHz. The pulses are stretched to 15 ps and amplified to 1 mJ / 3 kHz pulse energy and subsequently recompressed to 20 fs in a hybrid prism- / positive dispersion mirror compressor. Substantial spectral broadening is provided by a neon filled hollow fiber that is followed by a set of (negatively) chirped mirrors that compress the pulses down to <5 fs.

2.1.1 Pulse compression

After the amplifier, the pulses are focussed into a 1 m long hollow-core fiber with inner diameter of 250 μm filled with neon at a pressure of ~ 2 bar. The intense pulses broaden their spectrum (see Fig. 2.1) due to self-phase-modulation and the wider spectrum is recompressed to sub 5 fs using a set of low-loss chirped mirrors covering a wavelength range of 550 to 950 nm [41]. The transmission through the fiber is above 50 % resulting in pulse energies of 400 μJ after recompression.

2.1.2 Temporal and spatial pulse characterisation

For the continuous monitoring of the temporal pulse characteristics and dispersion adjustment, around 4 % of the power are split after the fiber and the chirped mirror compressor and sent to an interferometric second order autocorrelator. From the measured second-harmonic yield of the stepwise time-delayed interference of two pulse replica, the pulse duration can be calculated. Fig. 2.2 shows a typical measured autocorrelation trace. Fringe resolved autocorrelation traces (ACF) can be calculated [42] and compared with the measured ones to get an approximation of the pulse length. In case of the ACF shown in Fig. 2.2, this comparison yielded a pulse length of 3.9 fs. Even though ACF is the most widely used technique in determining the duration of short laser pulses, it suffers certain weak points.
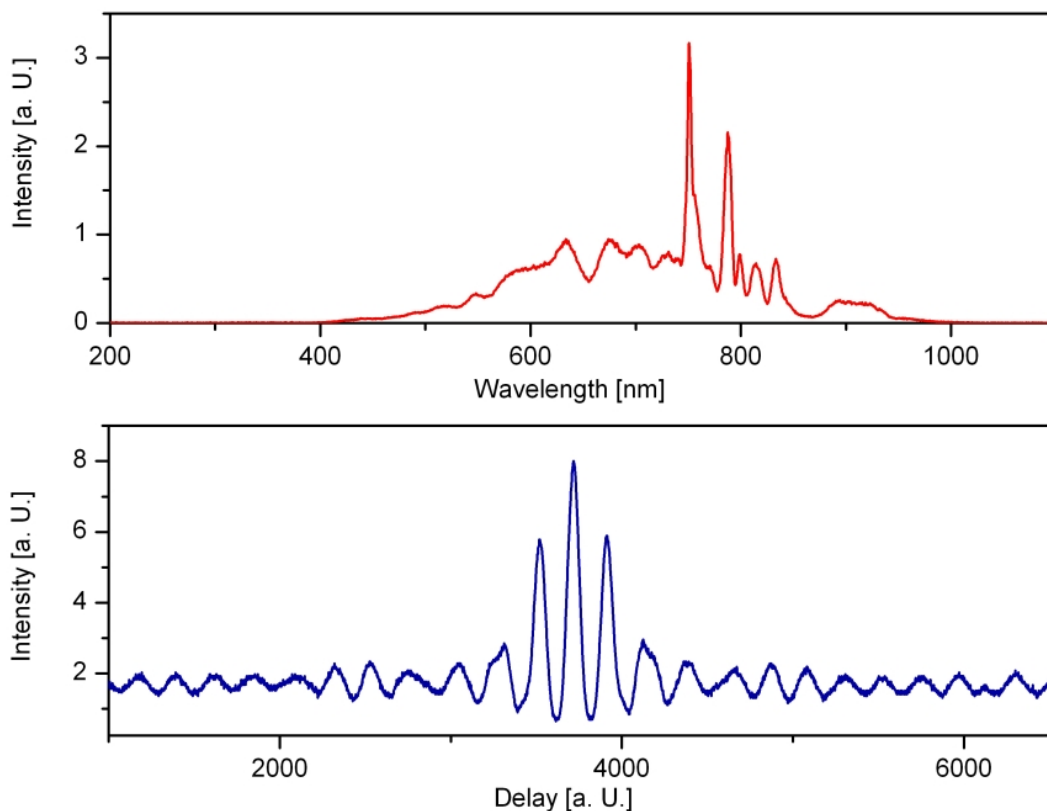

Fig. 2.2: Spectrum measured after the hollow-core fiber extending from 400 to 1000 nm (upper panel). A second order autocorrelation function (ACF) measured after compressing the pulses in the chirped mirror compressor is shown in the lower panel. Comparison with calculated ACF´s using the input spectrum leads to a pulse length estimation of 3.9 fs.

Laser pulses of this short duration comprise only ~1.5 cycles of the light electric field and since they are so sharply localized in the time domain, they necessarily cover a wide range of frequencies. As can be seen in Fig. 2.2, the spectrum of the light that composes the pulse is

spread over one octave requiring very precise control of the dispersion of the different colours. Since the fringe resolved ACF is not wavelength dispersive, inchoate compensation of the dispersion can only be observed in a change of the retrieved trace. Sign and order of a possible chirp can hardly be retrieved; in addition, bandwidth limitations and nonlinearities of the employed optics raised further questions on the reliability of the retrieved pulse characteristics.
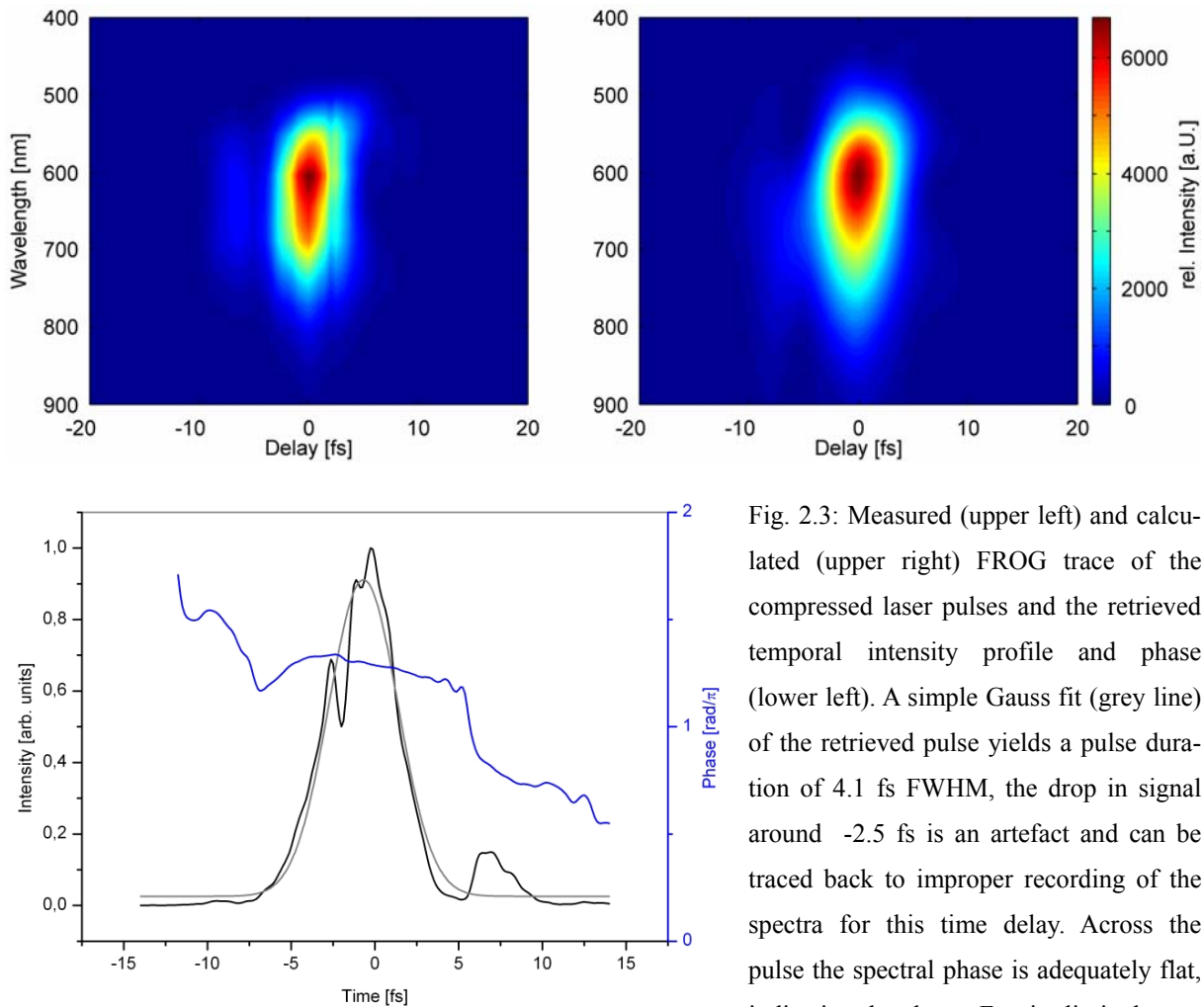

Fig. 2.3: Measured (upper left) and calculated (upper right) FROG trace of the compressed laser pulses and the retrieved temporal intensity profile and phase (lower left). A simple Gauss fit (grey line) of the retrieved pulse yields a pulse duration of 4.1 fs FWHM, the drop in signal around -2.5 fs is an artefact and can be traced back to improper recording of the spectra for this time delay. Across the pulse the spectral phase is adequately flat, indicating the almost Fourier limited compression of the pulses.

In order to overcome these limitations, measurements with a self diffraction frequency resolved optical gating device (FROG) [43] were performed. The fully reflective setup introducing no additional dispersion in the beam path and a self-made quartz plate fire polished down to 5 μm thickness acting as nonlinear medium widened the supported bandwidth to cover the full spectrum contained in the pulses. Fig. 2.3 shows the results obtained using commercial retrieval software (Frog3, Femtosoft technologies) based on adaptive algorithms.

The comparison with the measured, frequency resolved trace is striking; even weak modulations in the background of the false colour representations are reproduced by the algorithm. For the measurement shown, the obtained pulse length amounts to 4.1 fs in good agreement with the ACF for almost perfectly dispersion compensated pulses. Despite certain ambiguities of the retrieval, the method is clearly predominant in comparison with ACF. Since the pulse still measures itself in this technique, the absolute timing is concealed as well as the absolute phase of the pulse; the insight into the spectral phase however will lead to major improvements in the design of particularly adapted chirped mirrors. In the obtained results for the actual setup, the spectral phase already shows only small deviations of a flat function that can be contributed to little amount of residual higher order dispersion.

A good focusability and tight focussing are crucial for experiments where high intensities are required. As an example, only applications involving laser-plasma and multiphoton processes, laser ionization, or the discussed high harmonic generation shall be cited. The spatial quality of the compressed laser beam was characterized by means of the M^2 parameter. Using a CCD-Camera in combination with a microscope objective, the focal spot size was accurately determined and the beam diameter as a function of the distance to the focus was obtained using the knife-edge method.
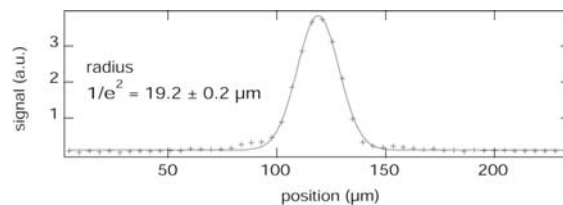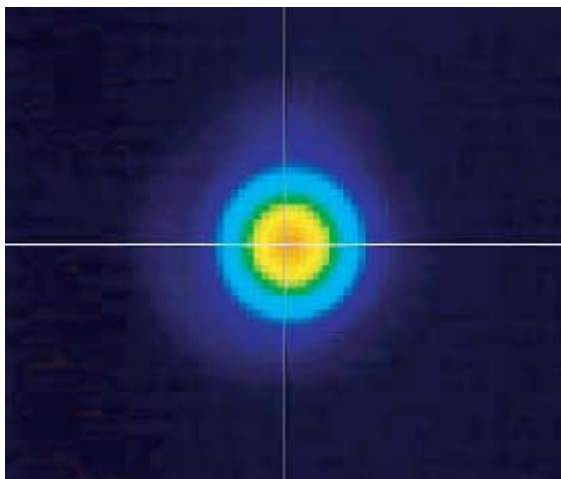
Fig. 2.4: Beam profile observed after the fiber (left) and beam profile in the focus (right) with a fit assuming a Gaussian profile with 19 μm width.

The measurement resulted in a very small M^2 value of $M^2 = 1.8$ +/- 0.1 with a Bessel-like beam profile caused by the hollow core fiber acting as spatial filter that improves the beam characteristics. Fig. 2.4 shows the beam profile observed after the hollow core fiber and the beam profile in the focus.

2.2 Carrier-envelope phase

2.2.1 Mode-locked pulse trains: the CE phase

For laser pulses that last only for a few oscillations of the light field, the actual evolution of the electric field becomes relevant rather than the intensity envelope. Although there is no universal definition of the absolute phase of light, short waveforms are usually described in terms of their carrier envelope phase (CEP). Staying with the definition used in the previous chapter and assuming an envelope function (e.g. Gaussian function) $E_a(t)$, a linearly polarized field with frequency ω can be described as

$$E_L(t) = E_a(t)\cos(\omega t + \varphi)$$

where φ allegorizes the offset between the oscillation $cos(\omega t)$ and the center of the envelope function $E_a(t)$. In Fig. 1.2, a sketch of the different settings is represented. For a broadband laser pulse the propagation in a medium is connected to dispersion, usually expressed as a wavelength-dependent index of refraction. In general, the propagation velocity v_p (phase velocity) of the individual partial waves is not constant but dependant on their frequency ω and their wave vector k ($v_p = \omega/k$), respectively. The propagation velocity of the whole wave packet, the group velocity v_g, is accordingly defined as the velocity (Rayleigh)

$$v_g = \left.\frac{d\omega}{dk}\right|_{k=k(0)} \qquad \begin{array}{l} k(0) : \text{medial wave number} \\ \text{of the wave packet} \end{array}$$

During propagation, the difference in phase and group velocity results in a slippage of the carrier wave under the envelope.

Inside a laser cavity, only the modes can exist that fulfill the condition that cavity length l and wavelength λ are only different by an integer number [44]. Translated into the frequency domain, this corresponds to the constraint that the frequency v of a laser mode has to be an integer multiple of the repetition rate $f_{rep} = 1/T$ with T as the cavity roundtrip time. In case of a mode-locked laser, this would inherently ensure that all pulses are emitted through the output coupler with the same CE phase, however, with the gain medium introducing dispersion, the cavity modes are shifted to be no longer an integer multiple of the repetition rate. This fact is illustrated in Fig. 2.5, the offset frequency f_{offset} corresponds to a phase shift between two consecutive pulses that are emitted from the oscillator.
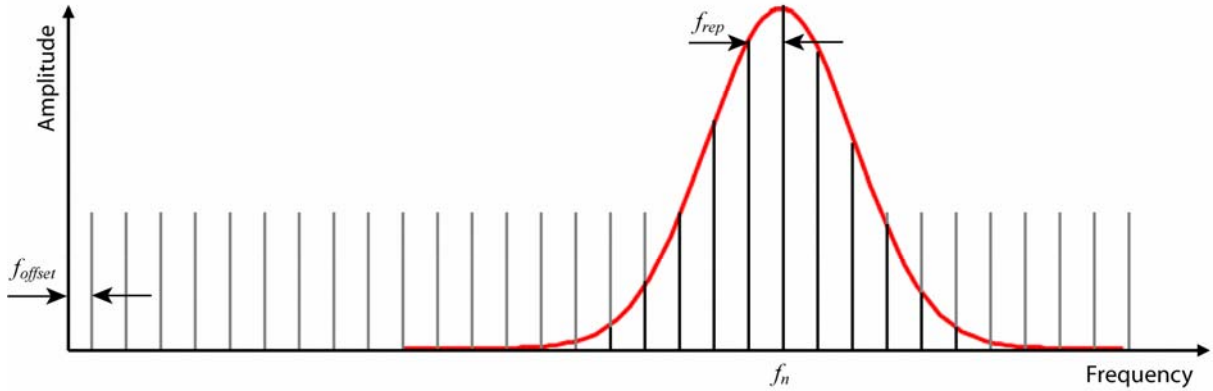
Fig. 2.5: Symbolic spectrum of a laser cavity, the cavity modes are separated by f_{rep}. In grey, the frequency comb is extrapolated to make its offset from zero visible. The offset frequency f_{offset} is the spectral manifestation of the phase slippage from pulse to pulse.

The nth mode has accordingly a frequency of

$$f_n = nf_{rep} + f_{offset}$$

and with f_{offset} usually differing from zero the change $\Delta\varphi$ in CE phase for two successive pulses is expressed as

$$\Delta\varphi = \frac{2\pi f_{offset}}{f_{rep}} \,.$$

This formula adverts immediately that measuring and controlling f_{offset} provides the opportunity of full control over the waveform the laser emits. The schemes presented here to stabilize the CE phase of the oscillator (section 2.2.2) and the amplifier (section 2.2.3) rely both on the measurement of this quantity by self-referencing techniques. In both cases, a heterodyne mixing of the fundamental light and its second harmonic gives access to f_{offset} if the fundamental light is broad enough to allow for spectral interference between its short wavelength components and the long wavelength components of the frequency doubled light. In accordance with the mathematical representation, called the f-to-2f technique:

$$2f_n - f_{2n} = 2nf_{rep} + 2f_{offset} - (2nf_{rep} + f_{offset}) = f_{offset}$$

Following the same outline, another scheme of retrieving f_{offset} can be derived dubbed the f-to-zero technique [43]. Provided the spectrum of the pulses to measure is broad enough, the dif-

ference frequency of two modes in the oscillator can be generated and overlapped with a long wavelength mode. Again in the mathematical representation:

$$(mf_{rep} + f_{offset}) \otimes (kf_{rep} + f_{offset}) \to (m-k)f_{rep}$$

The laser mode $mf_{rep}+f_{offset}$ is overlapped with the laser mode $kf_{rep}+f_{offset}$ to result in the difference frequency signal. The mixing signal of this with the long wavelength laser mode $nf_{rep}+f_{offset}$ for m, k and n integers fulfilling $m-k=n$ again carries the beat signal at the frequency f_{offset}.

$$(m-k)f_{rep} \otimes nf_{rep} + f_{offset} \to f_{offset}$$

2.2.2 The f-to-zero technique: Phase stabilizing the oscillator output

In the case of the ultra broadband output of femtosecond oscillators the f-to-zero technique can be employed to stabilize the CE-phase [34]. The output spectrum is focussed into an appropriate crystal (here a periodically poled one) that serves for two aspects: First, it is optimized to efficiently generate the difference frequency mixing and, secondly, its self-phase modulation characteristics broaden the spectrum additionaly. As described, the long wavelength carries then the modulation with f_{offset} that can easily be detected using an optical long pass filter. Consequently, almost all the energy emitted by the oscillator can then be send into the amplifier, an additional benefit is the fact that this detection scheme acts on the full laser pulse and does not have to rely on weak reflections that not necessarily preserve the CE phase. The beat signal is measured by a photodiode and analyzed by locking electronics (Menlo Systems) that generate an error signal proportional to the deviation of f_{offset} from the desired value. The error signal is used to feedback the pumping power of the laser oscillator and such to influence the intra cavity dispersion, Fig. 2.1 shows the location of the crystal (PP-MgO:LN) and the photo diode inside the laser system.

Fig. 2.5 implies, that for a given phase shift $\Delta\varphi$ from pulse to pulse, a certain waveform has a recurrence period of $2\pi/\Delta\varphi$ pulses. In the case of the oscillator used in this work, every forth pulse had, in principal, the same CE phase, the stabilization is used to counteract phase drifts that occur due to instabilities, drifts, thermal changes etc. For the amplification that supports just a repetition rate of 3 kHz, only a small number of the oscillator pulses is used. Out of the pulse train with 78 MHz repetition rate exiting the oscillator, a pockels cell picks only pulses that have the same phase and reduces the repetition rate to 3 kHz.

2.2.3 The f-to-2f technique. Phase stabilizing the laser amplifier output

While the stabilization of the oscillator CE phase under the terms of the described scheme is quite robust in the case of the very compact oscillator in terms of space and amount of optical components, in the amplification process several sources of phase noise occur. Following the oscillator, the pulses are first dispersively stretched to ~ps duration and the subsequent amplification in 9 passes through a Ti:Sa crystal comprises an extensive propagation through air and optical components. Furthermore, the compression using a standard prism compressor setup combined with positive dispersive mirrors as sketched in section 2.1 adds a considerable amount of material dispersion. The schemes to compensate for those phase disturbances so far relied on splitting of a small amount of power after the prism compressor and to send it into an interferometer designed according to the f-to-2f technique. The results demonstrated guaranteed phase stability at the output of the laser of typically 250 mrad within one standard deviation from the desired value.
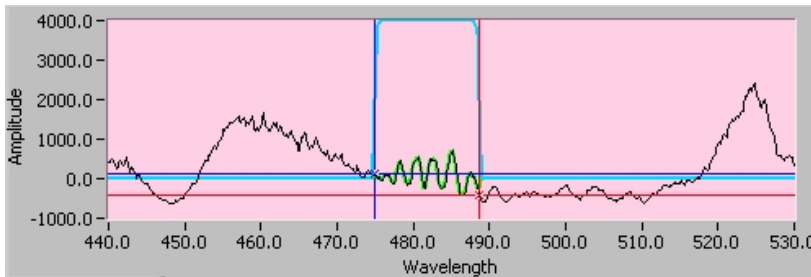

Fig. 2.6: Spectral region where the fundamental laser spectrum overlaps with the 2nd harmonic spectrum generated in a BBO crystal. The interference around 480 nm contains the information about the CE phase.

In the course of this work it was intended to overcome two main disadvantages of the implementations presented so far: The relatively narrow output spectrum of the laser amplifier does not allow for a direct f-to-2f measurement but needs the spectrum to be broadened in a filament by means of white light generation. This filament is usually realized in a sapphire plate and is very sensitive to fluctuations of the intensity; this dependency translates intensity fluctuations into artificial phase noise in the detection. Another drawback is the fact that in this stabilization scheme, the detection cannot account for phase changes introduced in the hollow core fiber and the chirped mirror compressor. In the realization presented here, the detection was moved to the exit of the chirped mirror compressor and as the output spectrum of the fiber is octave spanning, no additional spectral broadening is necessary. Fig. 2.7 shows a picture of the compact setup implemented in the laser system. Experimentally, f_{offset} is observed as interference pattern in the spectral region where the fundamental and the frequency doubled light overlap. The period and phase of this interference pattern can be analyzed using a

simple Fourier transform of this part of the spectrum and by its evolution, a feedback signal is processed using a LabView program. The observed fringe pattern is shown in Fig. 2.6. As implied in Fig. 2.1, the feedback signal is converted into a displacement of one of the prisms inside the prism compressor. Displacing the prism perpendicular to the beam using a piezo translation stage leaves the beam direction almost unchanged, but at the same time it adjusts the amount of material dispersion the pulses accumulate. A standard proportional controller algorithm takes care of adjusting the prism position such that the CE phase changes are counteracted. The achieved phase stability was better then 100 mrad, the improvement can be mainly accredited to the avoidance of the sapphire plate to broaden the spectrum and the location of the whole setup at the end of the laser chain. The significantly enhanced stability of the CE phase is observed as well in the XUV spectra recorded after the high harmonic generation (Fig. 3.5) that is, as described in the previous chapter, very sensitive to small changes of the carrier envelope phase.
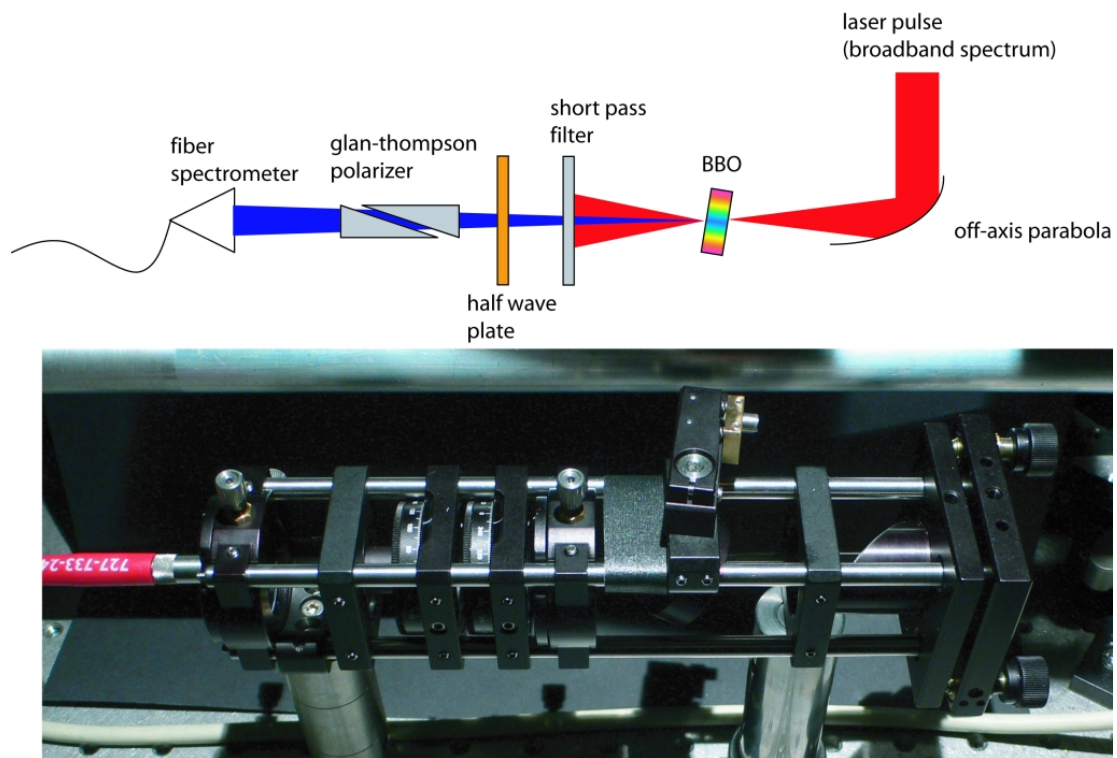
Fig. 2.7: Compact f-to-2f setup. Around 4% of the amplified and broadened light after the fiber and the chirped mirror compressor are focussed by a parabolic mirror into a BBO crystal. The second harmonic light is filtered by a short-pass filter and its polarization is turned to be parallel to the blue part of the fundamental spectrum. A Glan-Thompson polarizer is used to balance the relative intensity and the interference pattern carrying the CE-phase information is observed by a fiber spectrometer and analyzed by a software (cp. Fig. 2.6).

Chapter 3

State of the art of attosecond metrology: the AS-1 beam line at MPQ

The advances in the laser source development leading to potentially shorter attosecond (as) pulses, higher XUV flux, and the progress towards higher photon energies after the first experiments in the attosecond regime required analogous advances in the experimental setup. During this thesis, a new experimental setup was developed, relying on the pump-probe scheme [34, 46, 47] that has proven its unprecedented capabilities in allowing insight into ultra fast atomic processes but focused on advancing the technical standard of the setup towards three directions. The main goal of the improvement was to achieve UHV conditions in the experimental area to ensure the substantially improved contrast between the desired signal obtained in a specific gaseous target and influences of residual substances. Furthermore ensuring a reduced gas load through the whole apparatus was aspired to reduce the reabsorption of the generated XUV light und thus providing a higher photon number in the target. The third main objective was the improvement of the overall mechanical stability as well as the accomplishable time-step resolution to eliminate timing jitter effects in the measurement due to mechanical vibrations on the one hand and to access sufficient sampling for fast processes on the other hand. The four core constituents of the setup as described in this chapter are: i) the efficient generation of XUV light based on few cycle laser pulses ii) the capability of a direct spectral characterization of the light emitted iii) focusing and spectral selection of both the XUV and the laser light in perfect synchronization and iv) electron and ion mass spectroscopic tools. Fig 3.1 shows the basic layout of the attosecond beam line developed.

The last section of this chapter introduces the recent development towards ever shorter attosecond pulses and presents the demonstration of the shortest pulse so far, lasting only 80 attoseconds.
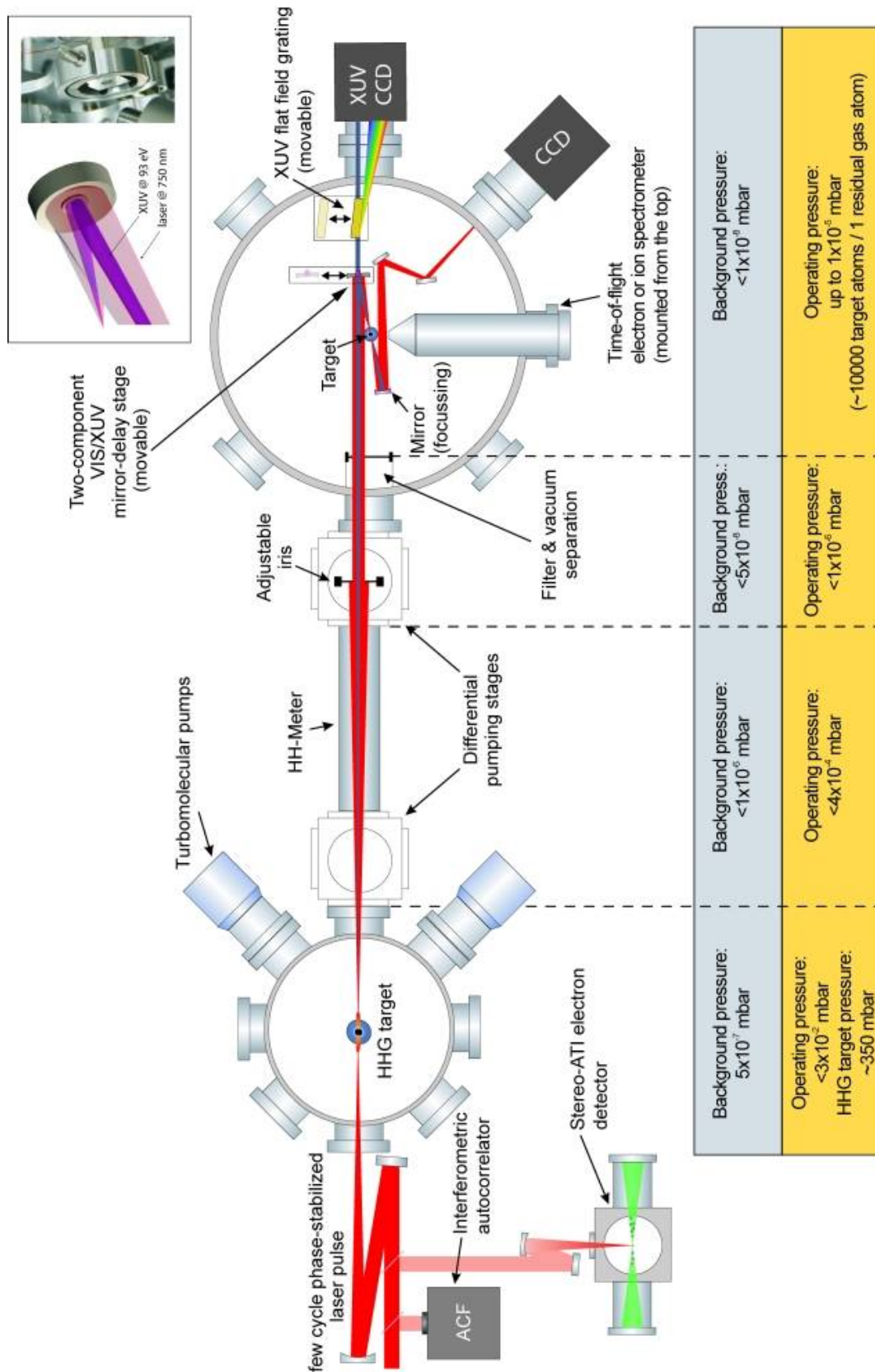
Fig. 3.1.: Layout of the experimental system AS-1. For a detailed discussion see text.

3.1 Vacuum pump-probe apparatus

Since a duration of 100 as corresponds to only 30 nm spatial displacement via the speed of light, special attention was turned to the implementation of vibration damping and isolation. To provide the required rigidity of the system, the optical tables inside the vacuum chambers are supported on separate posts directly mounted to the optical table that carries the experiment. These posts are connected to the chamber bottom and the walls only by edge welded bellows, unavoidable vibrations of the chamber walls due to the mounted turbo pumps are therefore not transmitted to the optical components inside the vacuum chambers. The roughing pumps are connected to the system using long flexible corrugated hoses that are vibration damped by bins filled with silica sand.

3.1.1 High-order-harmonic generation setup

The generation of the high harmonic photons is based on focusing the few cycle driver pulse into a nickel tube filled with neon at a constant pressure. The interaction length is optimized to achieve the highest conversion efficiency before dephasing and destructive interference lead to a decrease of the XUV flux. For the parameters presented, a propagation length of 2-3 mm at a pressure of ~ 350 mbar turned out to be the optimum value. Since even the theoretical efficiency of the HHG-process is in the range of 10^{-7} to 10^{-8}, the minimal possible reabsorption should be achieved to have a useful amount of photons in the experimental target. According to [48], reabsorption has to be taken into account for pressures $> 10^{-3}$ mbar. To remove the expanding gas jet as close to the generation area as possible, special turbo pumps (Alcatel ATH31+) are employed, that support a high gas flow maintaining the pressure below 10^{-2} mbar in the HHG-chamber. Based on the focus intensity around 8×10^{14} W/cm² at a focus diameter of 100 μm (for a 50 cm focal length mirror) the number of emitted photons per pulse is estimated to be just below 10^8 in good agreement with a measurement based on the calibrated quantum efficiency of a CCD camera (see section 3.2.2). Since it supports efficient emission of XUV light in the range of 12 nm wavelength (80-100 eV), neon has been chosen as target gas. According to the XUV generation taking place only in the most intense part of the driver laser focus (typically ~15 μm diameter [49]) and the small wavelength, the divergence can be extracted from the image of the XUV spot on the CCD camera (Fig. 3.2) 1,8 m behind the target to be <1mrad.
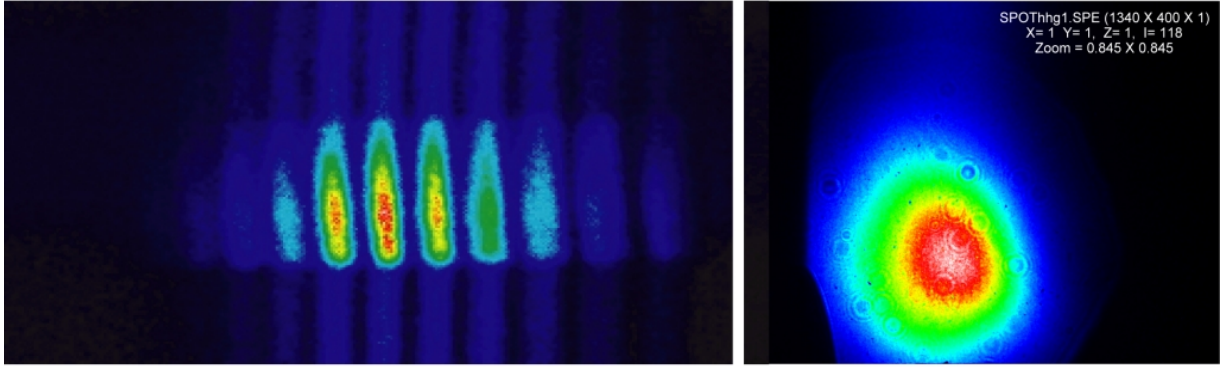
Fig. 3.2.: Harmonic spot 1.8 m downstream the generation volume with an estimated $M^2 < 2$. The decagonal structure (right panel) around the beam spot is the shadow of the aperture located at the entrance of the experimental chamber. The left picture shows the harmonic spectrum as observed after inserting the flat field grating into the beam.

Around 10 cm behind the HHG target, the well collimated XUV beam as well as the remaining IR field propagate collinearly through the first differential pumping stage. The reabsorption up to this point is estimated to be below 2%. In the subsequent beam path, the remaining pressure is too low to play a significant role.

Between the two differential pumping stages shown in Fig. 3.1 a residual gas ionization detector ("HH-Meter") inspired by the ionization chamber detectors at large accelerator facilities monitors the XUV flux and provides an efficient feedback on fluctuations of the strength of the HHG source. A conductive wire along the tube with a small voltage applied collects the electrons that are liberated by ionization of the remaining gas and an amplifier capable of measuring nano-ampere currents gives the desired measure of the XUV flux. The second differential pumping stage removes the remaining gas stream down to $\sim 5 \times 10^{-7}$ mbar and includes a motorized aperture to control the strength of the IR field entering the experimental chamber. Typical values for the laser pulse energy that can be set by the aperture are between 0 to ~ 50 µJ

3.1.2 Experimental chamber

Entering the experimental chamber, the two beams pass a variable filter setup that allows separating the beams into the central XUV part and the annular IR part by inserting a 2 µm laser pellicle with a 150 nm thick Zr foil (3 mm diameter) mounted properly at the center of the pellicle (Fig. 3.3). The extensively different divergence of the two beams is used in combination with the propagation through the vacuum system for the spatial separation of the two beams and subsequent recombination and focusing with an adjustable time delay being the key aspect of the experimental setup. The inset in Fig. 3.1 shows the double mirror assembly

whose inner part is multilayer coated to reflect and focus the XUV light. The outer part of the mirror assembly is coated with silver for dispersion-free reflectivity of the laser pulses. The multilayer coated XUV mirror [50] in the center is mounted on a very precise piezo stage allowing positioning with a resolution of better than 4 nm setting the ultimate limit for the smallest possible time step to the equivalent of 28 as. The whole double mirror assembly is motorized along and perpendicular to the incoming beam and has two independently adjustable angles such to precisely position the focus of the two beams under the entrance aperture of the different electron and ion spectrometers used in the experiments (section 3.3).
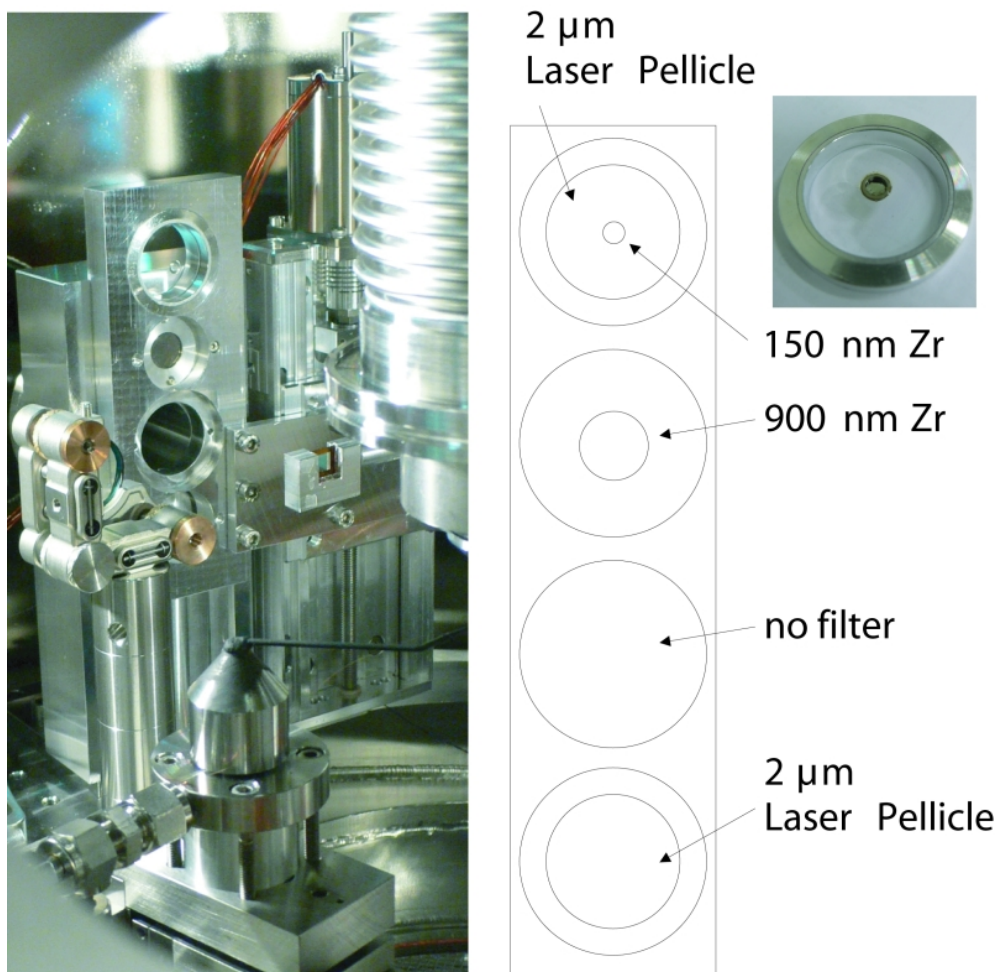
Fig. 3.3.: Filter slider and different filters exchangeable under vacuum. The upper filter allows separating the XUV light from the annular infrared light. A thick Zirconium filter can be introduced for observing the direct XUV beam as well as the spectrum with the XUV-CCD camera and a standard laser pellicle to block the XUV light.

For the experiment it is crucial to perfectly overlap the two foci not only along the beam, i.e. in time but also to accurately superpose their direction. Due to its shorter wavelength and better collimation, the focus of the XUV light (~ 25 μm) is safely smaller then the laser focus (~

100 μm).The inset in Fig. 3.4 shows how the two foci are imaged to align the overlap when the laser illuminates both mirrors. The figure shows a side view of the experiment in operation. The gas nozzle and the gas supply are visible as well as the electron-TOF and the double mirror assembly.

By observing the interference pattern and adjusting the two angles of the outer mirror, a perfectly symmetric interference pattern ensures excellent overlap of the two beams.
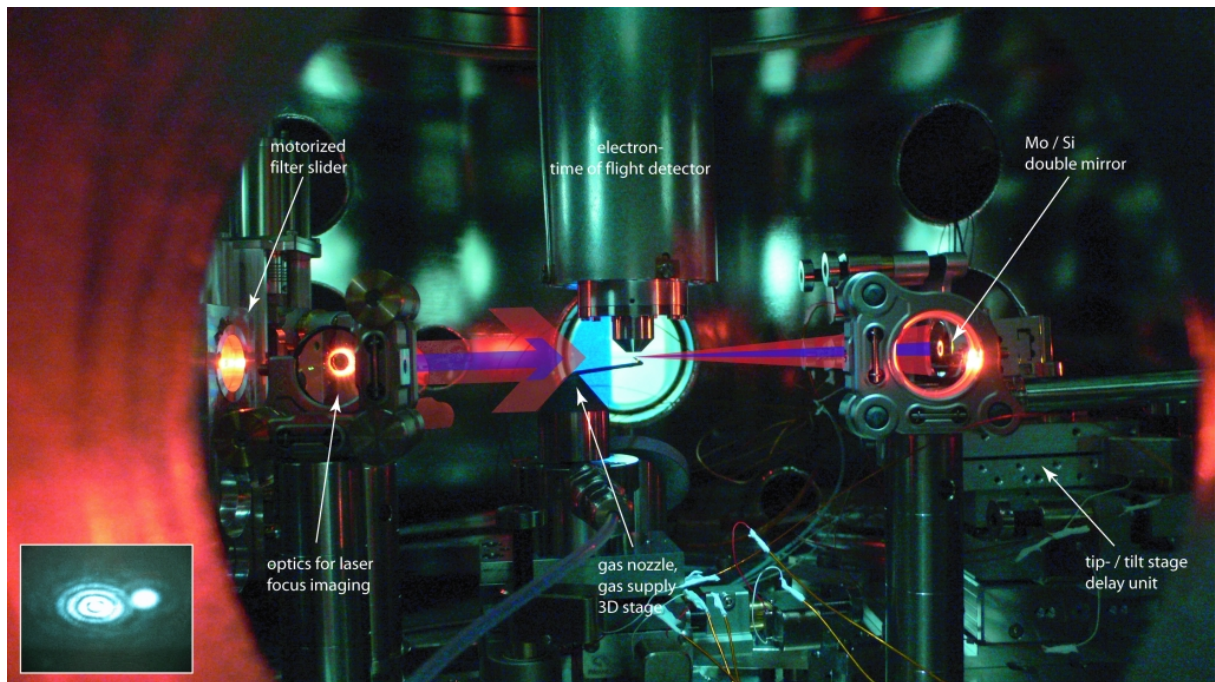

Fig. 3.4: Side view into the experimental chamber. The red arrow displays the incoming laser beam from the left and the focusing after the curved double mirror assembly. The blue arrow represents the beam path of the XUV light. The focus right in front of the entrance of the electron-TOF is approached from the side by the gas nozzle that ensures a high target gas density in the interaction volume. On the left hand side, the filter slider with the pellicle-/Zr-filter moved into the beam as well as the optics that are used to image the foci on a CCD-chip outside the chamber as shown in the inset are visible. Here the two foci of the inner and outer part of the mirror are displaced for demonstration.

The double mirror focuses the two beams under a slight angle (< 5°) such that the focus is located a bit aside the incoming beams, the astigmatism and the waveform distortion that result from this aberration is negligible. The focal region is located in the acceptance volume of an electron-time-of-flight detector or an ion-reflectron (see Section 3.3) at the same time. Given the little absorption cross sections in this energy range and the limited number of photons, the gas pressure in the focal volume should be as high as possible without deteriorating the vacuum conditions over an extended region. To this end, a metal coated glass nozzle with

inner diameter of ~ 30 μm ejects the experimental gas as a confined jet perpendicular to the laser beams. This technique guarantees furthermore that averaging effects over an area larger then the focus can be avoided. Since most of the experiments presented here are sensitive to a longitudinal phase delay [51], the Gouy-phase of the laser beam, which inverts within the confocal parameter of the laser, is of major importance.

3.2 Characterization of XUV light

For adjustment and optimization of the XUV source, a direct observation of the beam, its direction and its spectral behavior is essential. For these purposes, an imaging spectrometer based on a grazing incidence flat field grating [52, 53] and a back illuminated CCD camera are located at the exit of the experimental chamber. After the double mirror assembly is moved out of the beam, the XUV light can be monitored (Fig. 3.2). Either the direct beam, or, after inserting the grating the spectral extend of the generated XUV light is recorded.

The imaging spectrometer has an overall efficiency (grating ~85%, CCD-chip ~40%) of 35% and its minimal acquisition time to achieve a useful spectrum is limited by the shortest exposure time of the camera around 50 ms. The spectrometer is therefore, at the same time, one of the fastest CE-phase monitoring devices by requiring the accumulation of only 150 pulses to provide information about changes in the CE-phase. The calculated resolution is around 0,1 eV, the typical structure spacing of twice the fundamental photon energy (750 nm correspond to 1.6 eV) in the harmonic spectra can be clearly resolved as shown in panel *e* of Fig. 3.5. In order to prevent saturation of the CCD chip, the laser light is filtered out using a 1.5 μm zirconium foil at the entrance of the spectrometer. In Fig. 3.5 the drop of the signal at low energies is due to the transmission characteristics of this foil [54].
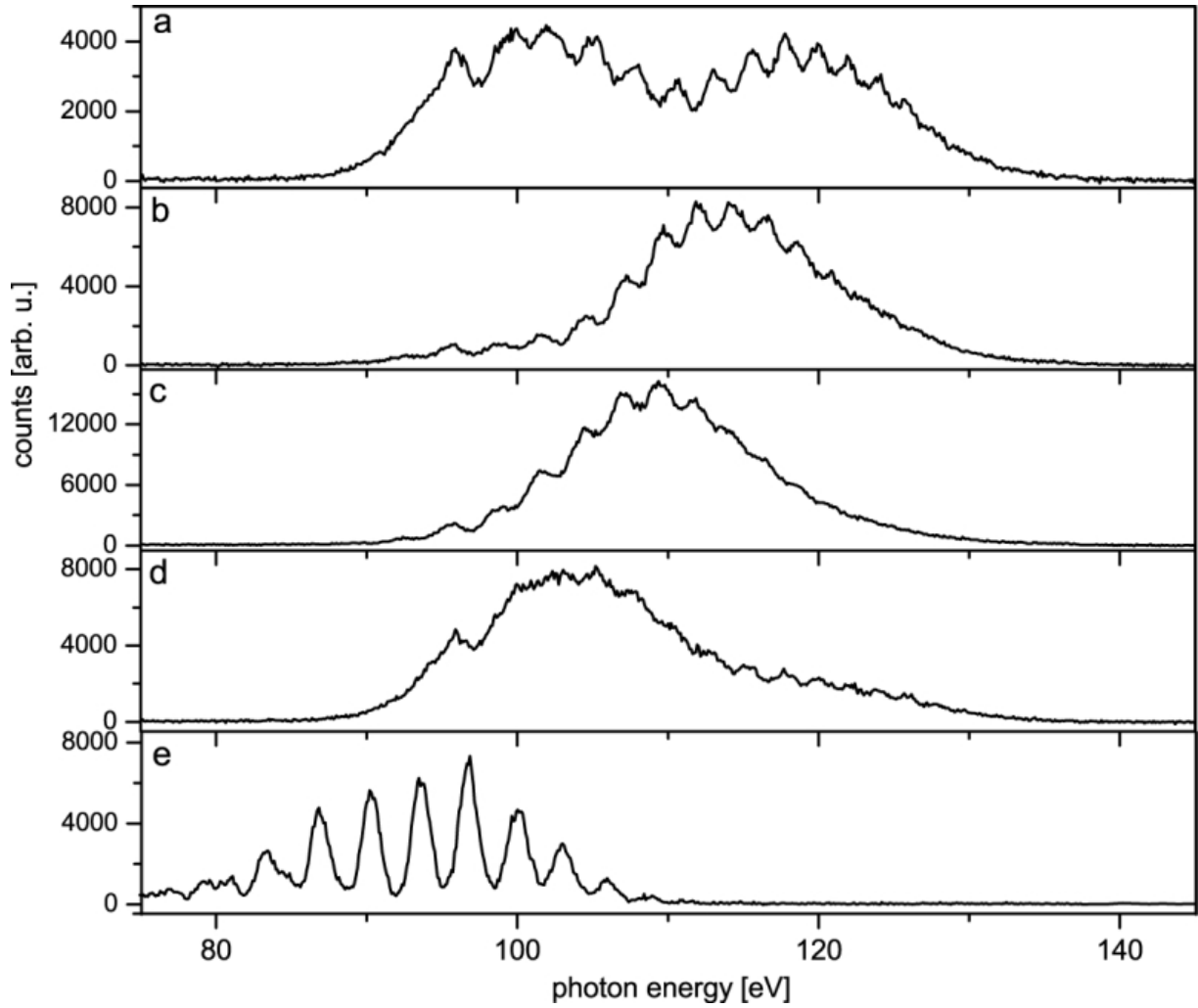
Fig. 3.5: CE phase dependence of the XUV spectrum [40]. A XUV spectrum for an initial value φ of CE phase, which is believed to be close to zero (corresponding to a near cosine-shaped waveform), is shown in panel (a). Corresponding spectra for the CE phases $\varphi = \varphi_0 + \pi/4$, $\varphi = \varphi_0 + \pi/2$, $\varphi = \varphi_0 + 3\pi/4$ are shown in panels (b), (c), and (d) respectively. In general, the spectral features are strongly dependent on the CE phase and the effective cut-off energy shifts by more than 10 eV as the CE phase is varied. An XUV spectrum generated by relatively long NIR driver pulses is shown in panel (e). Deep modulation in this HHG spectrum, evoked by the the use of long driver pulses (15 fs), demonstrates the resolution of the spectrometer.

3.2.1 Spectral filtering of the XUV light

To make use of the extreme temporal resolution that attosecond pulses offer, an experiment needs to be capable to spectrally select and to focus the generated radiation. Given the low conversion efficiency, the focusing should not drastically compromise the intensity and the temporal characteristics should be preserved. For isolating single attosecond pulses, it is fur-

thermore necessary that the XUV optics filter out the non-continuous part of the spectrum corresponding to a train of attosecond pulses (see Section 1.2.2).

To meet these ambitious demands, multilayer mirrors are used. These mirrors consist of a series of layers of alternating materials (here Molybdenum and Silicon) coated on a curved substrate. By adjusting the relative layer thicknesses, the sequence of materials and the number of layers, the reflectivity can be shaped to meet the necessary conditions. Furthermore, to achieve pulses as short as the Fourier limit of the reflected spectra, the spectral phase has to be controlled. In this work, different multilayer mirror designs were used (see Section 4.2 and 4.3) that, in combination with careful adjustment of the harmonic cut-off, made the reliable generation of isolated attosecond pulses with durations well beneath 200 as possible. Our recent developments led to the realization of the first source for sub 100 as pulses that now can routinely be used in experiments that so far suffered from a less precise time resolution.
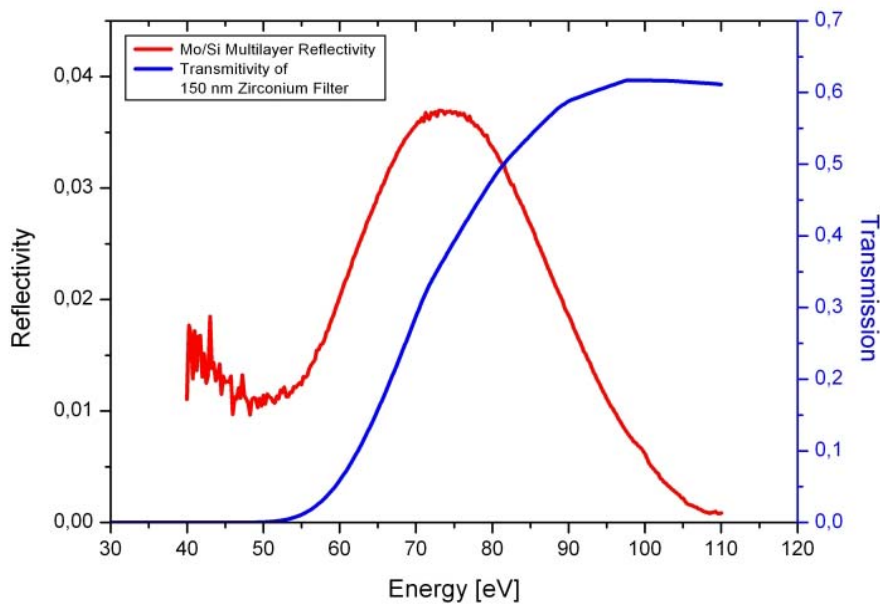
Fig. 3.6: Reflectivity curve of the Mo/Si Multilayer mirror employed in the experiment (red) and transmission characteristics of a 150 nm zirconium foil used as high pass filter in the experiment. The bandwith selectivity of the mirror in combination with the suppression of low harmonic radiation due to the Zr filter makes multilayer mirrors a perfect tool for the synthesis of isolated attosecond pulses.

In Fig. 3.6, a typical reflection curve of a multilayer mirror employed in the experiments is shown as well as the transmission characteristics of the zirconium filter. Due to the complete absorption of photons with energies below 60 eV in combination with the reflectivity characteristics of the mirror it is possible to select a spectral band in which, with carefully chosen parameters of the generating laser field, the emission corresponds to only one single half cycle

of the laser pulse and thus forms an isolated pulse. With the advances in the laser source development towards pulse durations containing less than two cycles of the laser field, the generation of a more extended continuous spectrum became feasible. In combination with multi-layer mirrors that support a substantially increased spectral bandwidth as compared to the first experiments shorter and shorter attosecond pulses could be achieved. Fig. 3.7 shows an example of such broadband radiation selected by the mirror/zr-filter system centered at 75 eV extending over 25 eV full width at half maximum (FWHM) potentially supporting pulses as short as 75 as. The experimental uncertainties together with an inherent chirp in the generation process (high energetic photons are produced later within the emission) lead to the minimal retrieved pulse length of 85 as, close to the Fourier limit for the employed spectrum of 83.1 as.
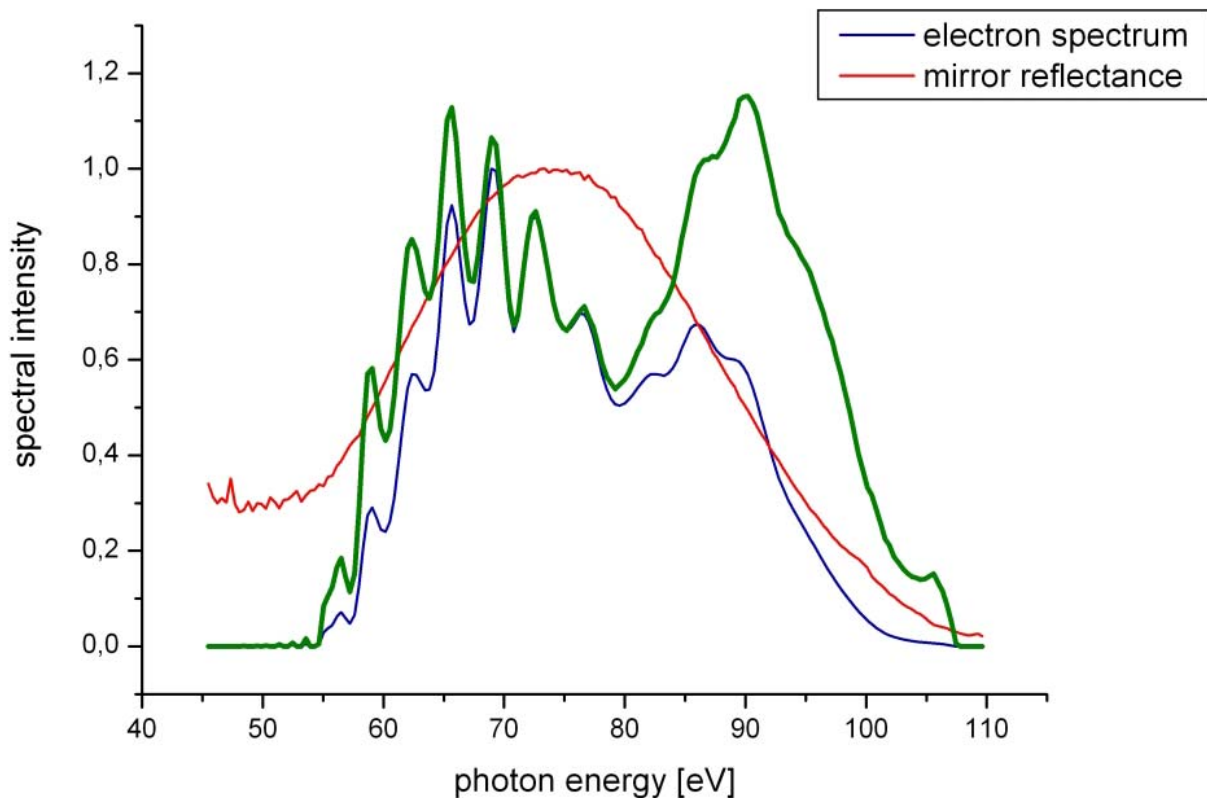
Figure 3.7: The measured electron spectrum (blue line) shifted up by the amount of the ionization potential corresponds to the spectral intensity of the XUV pulse that ionized the rare gas sample. The deconvolution with the normalized mirror reflectivity (red line) represents the spectral shape of the light impinging on the mirror. This spectrum (green line) is transmitted through the metal foil filter.

3.2.2 XUV pulse intensity

Core hole excitations followed by dynamics evolving on an attosecond timescale are, in general, characterized by little absorption cross sections. Direct-photo ionization of helium 1s electrons at 90 eV photon energy has a partial cross section of 5×10^{-1}, the first shake-up satellite (n=2) 4×10^{-2}, respectively (cp. chapter 4.2).

Experimentally, these low cross sections translate into low count rates in the described cross correlation experiments. Changes in the generation scheme of the high harmonic light therefore have to be reviewed in consideration of the generated flux within the useful energy band. The number of photons that form the attosecond pulse, however, is not directly amenable to experimental techniques and hence often subject to estimations along general lines. The following section describes a strategy to obtain the energy per attosecond pulse taking into account the actual spectral shape of the light produced as well as the reflectance curve of the XUV mirror and the energy dependant transmittance of the involved metal filter foils. The calibrated XUV-sensitive camera used to observe the spectra shown in Fig. 3.5 can record images of the direct XUV beam as shown in Fig. 3.2.
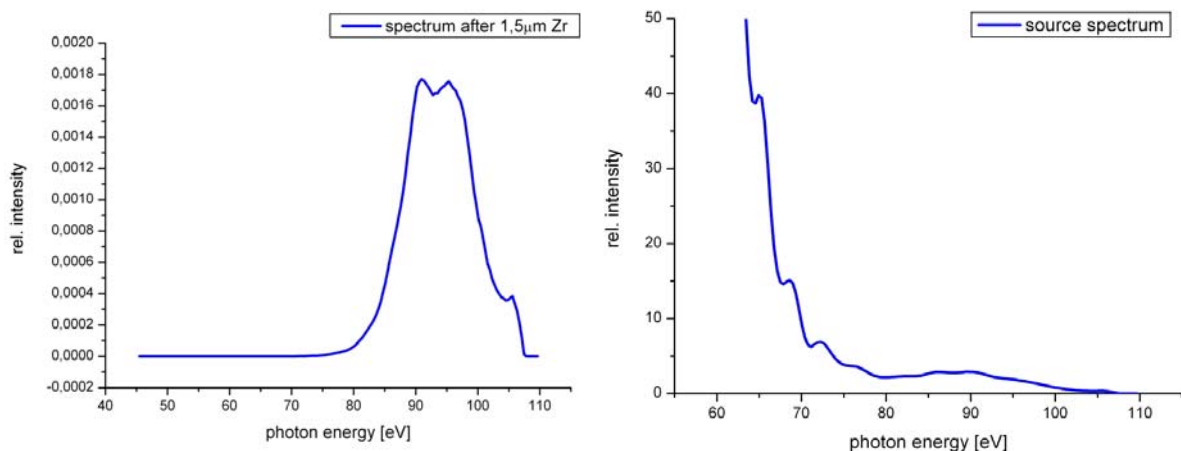
Figure 3.8: The photon spectrum after mathematically applying the transmittance of 1.5 μm Zirconium (left). The right hand side shows the source spectrum after the mathematical removal of all filters from the measured spectrum. It's clearly visible that the need to use only the photons in the "cut-off"-area of the generated harmonic radiation limits the efficiency.

After proper background subtraction and considering the known quantum efficiency of the camera and the integration time, an absolute number of photons after the filters in front of the camera can be extracted. The spectral shape of the attosecond pulse is accessible using the electron spectrometer. The knowledge of the filter transmittance (300 nm Zirconium for recording the e⁻-spectrum and 1.5 μm for recording the photon spectra) allows retrieving the

spectral intensity of the XUV light reflected by the mirror by shifting the measured electron spectrum up by the ionization potential and multiplying with the inverse mirror reflectance. (Fig. 3.7).

This spectral distribution is used and the filter transmittance is artificially adjusted by dividing by the transmittance of the thin filter used to record the spectrum and multiplying with the transmittance of the thick filter that was used to take the camera picture of the harmonic beam. This technique provides the opportunity to access the photon number that forms the attosecond pulse. The comparison of the integral of the photon spectrum after the mirror with the one of the spectrum that reaches the camera determines the factor that converts the number of photons measured by the camera into the absolute number forming the attosecond pulse.
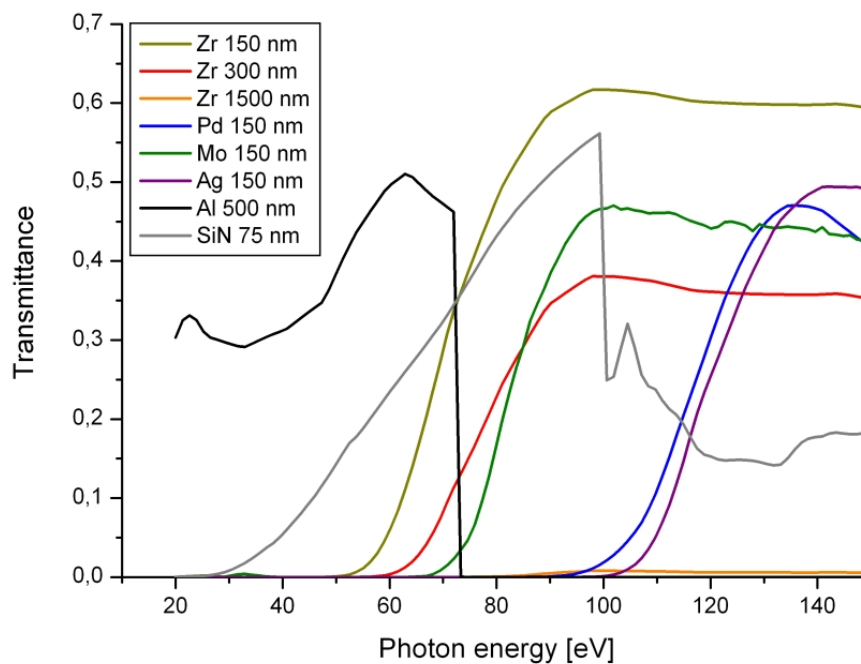
Figure 3.9: Filter transmittance vs. photon energy. The black and the grey curve depict the transmittance of Aluminum and Silicon-nitride that are by reason of their sharp absorption edges suited for a calibration of both the electron- as well as the photon spectrometer. The colored curves show the transmission properties for different metals that where used within the scope of this work in the thickness specified in the caption of the graph. Comparing the curves for zirconium shows that duplication of the filter thickness introduces a considerable variation of the transmission to higher energies.

Fig. 3.8 shows the small fraction of the spectrum that is detected by the camera, the overall intensity is dramatically reduced and due to the exponential dependence of the spectral transmittance on the filter thickness a clearly visible shift towards higher energies is apparent. By

mathematically un-applying all filter foils in the beam path, the shape of the harmonic radiation spectrum in the source is attainable. The number of photons generated fades dramatically towards higher energies. As already suggested in chapter 3.2.1, only a sufficient suppression of the low-energetic photons in the plateau-region of the generated spectrum allows for the generation of isolated attosecond pulses. Choosing of the right filter material in combination with a given mirror reflectivity is therefore a crucial point in the reproducible generation of isolated attosecond pulses. A comparison of the transmittances of the different filter materials employed in the experiments presented here is shown in Fig. 3.9.

3.3 Electron- and ion-TOF – Choosing the measurand

For the experiments presented in this work, two different detection schemes were employed. During the measurements aiming at the achievement of shorter attosecond pulses and the shake-up measurement in Helium, an electron time of flight spectrometer was employed. In the course of studying tunnel ionization, the produced ions were selected as measured variable and detected by a reflectron type time of flight ion spectrometer (R-TOF).

3.3.1 The electron time-of-flight spectrometer

As a general tool for studies in the energy domain of charged particles, the time-of-flight scheme is well established in a wide scope of science. The principle of this spectrometry draws on the fact, that charged particles of different mass or kinetic energy undergo a different acceleration in an external electric field. The time-of-flight describes the method used to measure the time that it takes for a particle to reach a detector while traveling over a known distance. In the case of electron time of flight spectrometry, the kinetic energy of the electrons under scrutiny is determined by measuring their arrival time on a detector placed in a known distance from the generation volume.

The time resolved detection of their arrival gives direct access to their kinetic energy - if Δt is the smallest detectable time unit, the energy resolution ΔE is given as:

$$\Delta E = \frac{2\sqrt{2}\Delta t}{m_e L} E^{3/2}$$

m_e : electron mass

L : length of drift tube
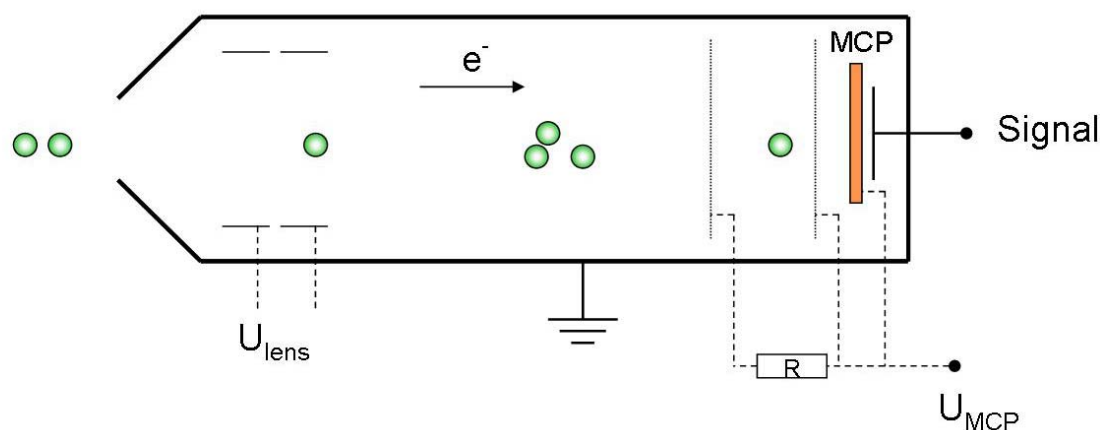
Fig. 3.10: Schematic of the time of flight spectrometer (TOF). The electrons enter the drift tube after passing the electric lens that helps to compensate for flight time dispersion. After passing the drift tube, they are accelerated and hit the multi channel plate (MCP).

Since the range of kinetic energies of interest is set by the photon energy employed in the excitation lowered by the ionization potential of the experimental gas, the highest energetic photons to detect have a kinetic energy of about 90 eV. According to the above formula, the energy resolution is about 1% (Δt =250 ps, L =360 mm) in the range of 50-100 eV, for low energetic electrons it is better. This resolution is satisfactory for the experiments carried out, even though it sets a limit to the observable structures on the spectra recorded that might give additional insight to the processes involved (section 3.5.2). Fig. 3.10 shows a schematic of the time of flight spectrometer used for the experiments presented [55]. It has a magnetic shielded drift tube of 365 mm length and a subsequent acceleration area of 70 mm length. This post acceleration ensures a sufficient velocity of all the electrons hitting the detector to avoid nonlinearities in the MCP response. The detector consists of a 40 mm Burle MCP stack. At the entrance of the flight tube, an electrostatic lens allows to increase the acceptance angle of the electron collection. The signal measured at the MCP collector is digitized using a multiscaler card (FAST COM) with minimal time discretisation of 250 ps. It turned out, that the use of additional amplifiers has to be avoided since even very fast amplifiers with careful adjustment of the trigger levels occasioned distorted electron flight-time spectra.

Fig. 3.11 shows a typical electron time of flight spectrum recorded by ionizing neon using the mirror that corresponds to the reflectivity curve shown in Fig. 3.6. The central photon energy of 75 eV is revealed in the electron spectrum centered at 54 eV corresponding to the ionization potential of the neon 2p state that amounts to 21.56 eV.
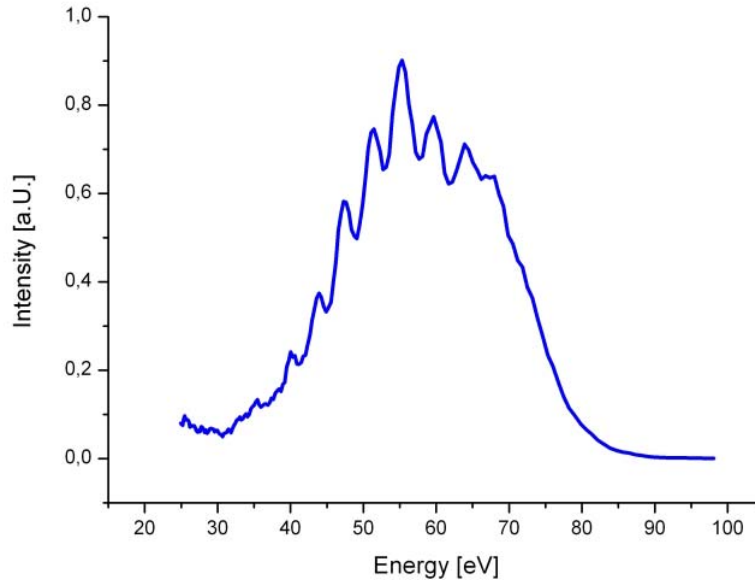
Fig. 3.11: Electron spectrum measured with the TOF electron spectrometer. It shows the distribution of photo-electrons generated by XUV light reflected of a multilayer mirror shown in Fig. 3.6. The structure in the low energy part corresponds to interferences in the incoming spectrum indicating that not all of the photons reflected are emitted in one single recollision process. The observed modulation gives rise to a ~5% satellite pulse in intensity.

The spectrum shows a remaining structure at the low-energy part that corresponds to the spectral interference of XUV photons generated in two adjacent half cycles of the driving laser field. In the time domain, this interference is manifested as a satellite pulse shifted half a laser period with respect to the main burst. From the modulation depth, the amplitude ratio of the two pulses can be estimated to be around 20:1 in good agreement with the ratio retrieved by a XFROG algorithm (3.5.2). As the modulation does not extend over the full bandwidth, the satellite pulse is shifted towards lower energies with respect to the main pulse and, due to its lack of bandwidth, its time structure is decisively longer.

3.3.2 The reflectron-type ion time-of-flight spectrometer

For studying the temporal evolution of charge state distributions, a R-TOF was employed. Its working principle is based on time of flight mass spectrometry where ions are accelerated in an electrical field to the same kinetic energy with the velocity of the ion depending on the mass-to-charge ratio. Thus, the time of flight can be used to determine the mass-to-charge ratio. Ions of a specific atom but with different charge states are flight-time-separated as well, therefore, after ionization, the ratio between different charge states can be determined. The principal limitation of a linear ion-TOF spectrometer is the relatively low mass resolution

achievable because of the energy spread of the generated ion packet and other experimental factors such as delayed ion formation and space charge effects.
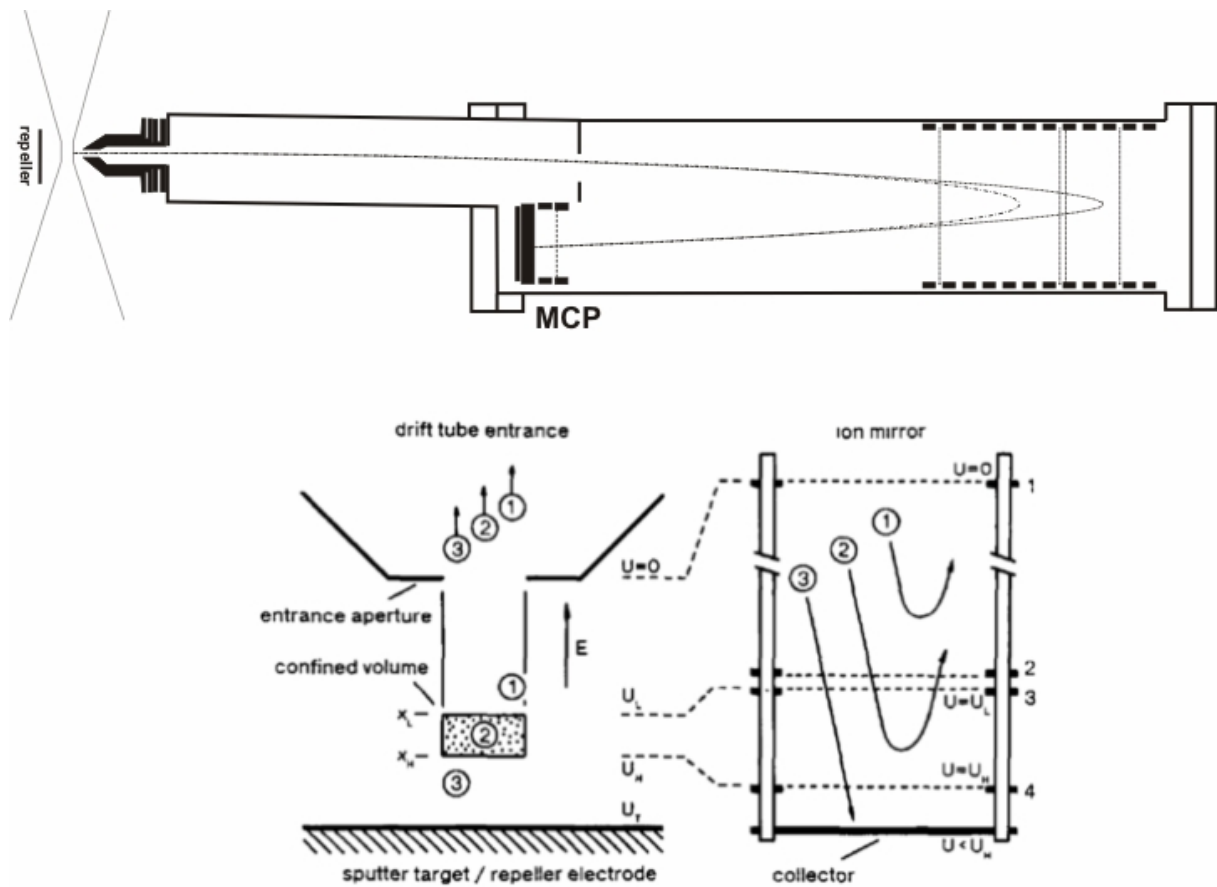

Fig. 3.12: Layout of the reflectron ion mass spectrometer. A cross cut of the spectrometer shows the location of the laser focus between the repeller and the entrance aperture of the spectrometer (extractor) and two different ion trajectories inside the spectrometer for ions of different initial energy. The lower panel shows the behavior of ions generated in three different regions of the ionization zone. The energy filtering capacity of the ion mirror can be used to separately detect ions originating from a certain axial area. Its width and location can be tuned by adjusting the applied voltages.

In order to improve the performance of the time-of-flight mass spectrometer, in a reflectron spectrometer an ion mirror is added. The reflectron makes use of an electrostatic field to reflect ions through a small angle towards a second detector. Ions with same mass-to-charge ratio but higher kinetic energy penetrate deeper into the reflector, delaying their time of arrival at the reflector detector relatively to the slower low-energy ions. Fig. 3.12 shows a layout of the employed reflectron [56] and the working principle of the ion mirror. This concept aims to achieve flat ion flight time dispersion over a broad range of energies and is similar to the idea of chirped mirrors in the temporal compression of dispersed optical pulses. As can also be seen in the lower panel of Fig 3.12 as well, the reflectron idea comprises in addition possi-

ble access to the origin of the ions created. A steep field gradient between repeller and extractor imprints a linear shift in the kinetic energy of the ions.

The place of birth of the ions along the spectrometer axis between repeller and extractor is therefore encoded in the ion kinetic energy and using the ion mirror as an energy filter enables to restrict the detection to ions created in a specific volume.

This technique was employed in the experiments in regard to charge state distributions in high intense laser fields drafted in Section 4.3. Fig 3.13 depicts a typical mass spectrum taken for xenon. The photon energy of the XUV pulses used there was centered at 93 eV and exhibited a bandwidth of 9 eV corresponding to pulses of ~250 as length. The data are accumulated using an amplifier in combination with a multiscaler card. The overall resolution of the spectrometer and the detection electronics allows a *Δm/m* ratio of better than 10^{-3}.
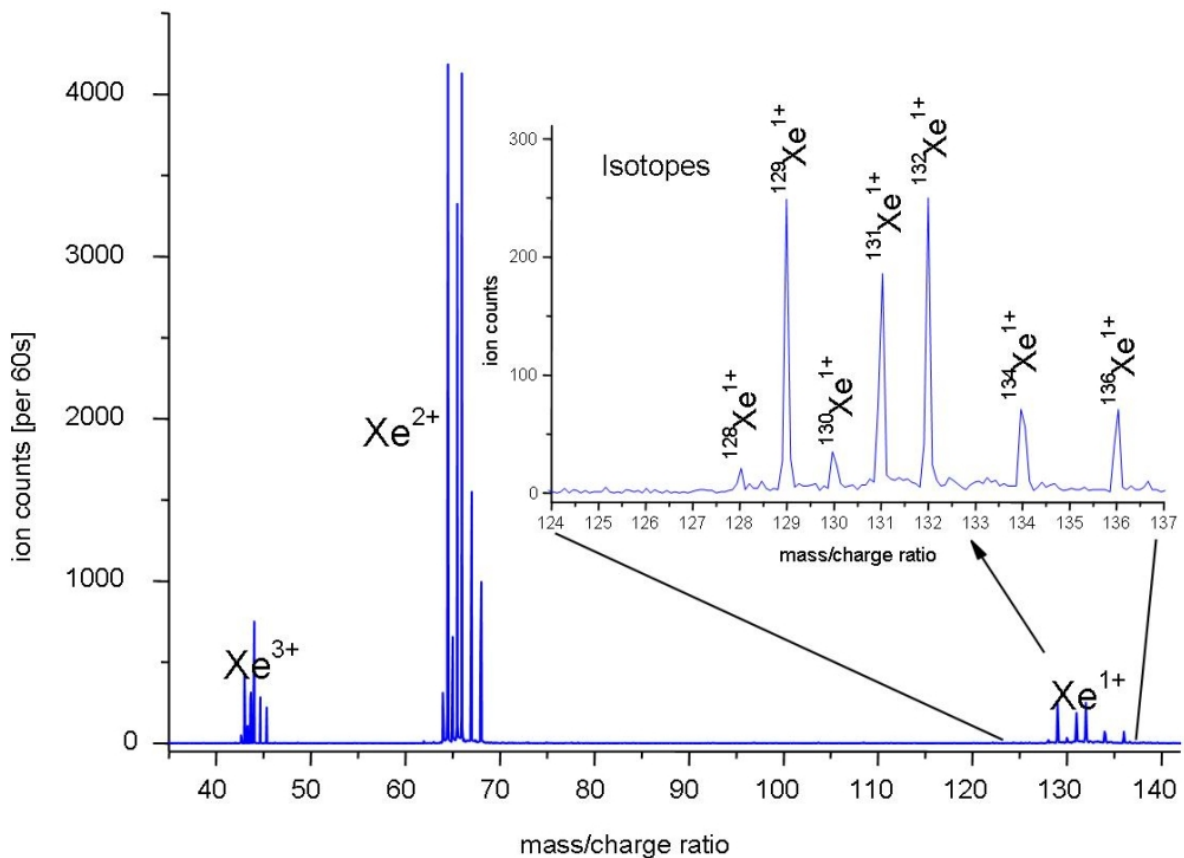
Fig. 3.13: Mass spectrum recorded in xenon after XUV excitation around 93 eV. Three charge states of xenon can be observed, the relative intensity shows a distinguished correspondence with the interaction cross sections known from synchrotron studies. The inset shows a close up of the generated Xe+ ions. Seven isotopes can be discriminated; there are two more (mass 124 and 126 respectively) with natural abundances below 0.1%. The resolution of the spectrometer is specified as *Δm/m = 10^{-3}*.

3.4 Advancing towards shorter pulses – Attosecond streaking

The strong-field interaction of a few cycle light wave with free electrons released by a sub-femtosecond XUV excitation results in broadening and shifting of their final momentum distribution. Recording those streaked spectra of the emitted photoelectrons versus delay between the visible laser pulse and the XUV pulse allows retrieving the XUV pulse and the laser field. The following section follows chronologically the major advances towards shorter pulses / higher flux that have been made during this work. The first attempts relying on the use of *chirped multilayer XUV optics* [64] led to the shortening of the pulses down to 170 as. The work in this direction supported a better understanding of the formation of XUV continua that, in combination with evolutions of the driving laser towards shorter visible pulses, helped to achieve isolated intense sub-100 as pulses based on *periodic multilayer mirrors* with a flat phase response over a bandwidth of more than 25 eV [89]. These developments are illustrated in section 3.5.

3.4.1 Powerful 170-attosecond XUV pulses generated with few-cycle laser pulses and broadband multilayer optics

As illustrated in Chapter 1, the time resolution required to track and control electron dynamics on the atomic scale is evolving on an attosecond timescale. Advances in ultrafast optics, foremost intense few-cycle laser pulses comprising merely a few well-controlled oscillations of the light field, (T_{pulse}~2.5 fs) have allowed – via high harmonic generation in an atomic gas reproducible production of isolated XUV attosecond pulses of 250-as duration at ~ 100 eV and 130-as duration at ~ 35 eV [57]. These durations correspond to only 1/10 and 1/20 of the field oscillation of a laser pulse, respectively. These pulses permitted a direct and complete characterization of light waveforms for the first time [57, 32, 47].

High harmonic generation in rare gases has been discovered as a powerful means of providing coherent extreme ultraviolet radiation from a compact laser-driven source long time ago [58, 59]. However, only few-cycle-laser pulses permitted efficient confinement of the emitted coherent, laser-like radiation within the laser oscillation cycle and extending the spectrum of this confined radiation to the water window and well beyond. With the advent of intense few-cycle near-infrared pulses, the isolation of sub-laser-cycle duration XUV light bursts (one burst per laser pulse) with well reproduced pulse parameters became feasible for the first time. As already pointed out, the controlled isolation of a single energetic harmonic pulse requires control of the amplitude of spectral components of the emitted XUV radiation over a broad (sev-

eral eV or more) spectral range. Furthermore, transform-limited XUV pulse production calls for precise control of the phase over the spectral band selected by bandpass filtering. Such a phase control has been demonstrated by utilizing the dispersion of materials near electronic resonances [60, 61]. However, the applicability of this approach is restricted to selected spectral domains. By analogy to broadband dispersion control of optical pulses in the visible and nearby spectral ranges with chirped multilayer dielectric mirrors, chirped multilayer metallic mirrors have been proposed and developed for the same purpose in the XUV spectral range [62, 50]. The generation of isolated 170-attosecond XUV pulses was demonstrated based on the utility of these techniques. As outlined in chapter 1, this result has been achieved by ionizing neon atoms with sub-5-fs near-infrared pulses without the need for polarization gating resulting in a substantially improved NIR-to-XUV conversion efficiency and photon fluxes useful for time-resolved spectroscopy. The advances described in the following section are motivated by the need for shorter and more powerful XUV pulses for improved studies on ionization dynamics as described in the previous section and in general for interrogating a wide range of fundamental electronic processes in matter evolving on a hyperfast, sub-100-as timescale [63].

Generation of attosecond XUV pulses

Following the ideas of the "three-step-model" introduced in chapter 1.2.1, the emission of XUV radiation by laser pulses interacting with atoms takes places around the maxima of the electric field oscillations. The maximum energy of the emitted photons can be estimated by $E_{max} = I_p + 3.17 U_p$ with I_p being the atomic ionization potential and U_p being the ponderomotive energy of the electron in the oscillating electric field of the laser. Since the ionization potential is an inherent atomic property, the only parameter that can be controlled in this process is U_p defining the highest energy photons emitted.

By setting the carrier envelope phase (CE-phase) of a few-cycle laser pulse such that the field maximum coincides with the maximum of the pulse envelope (resulting in a substantial modification of U_p for consecutive recombination events) - referred to as cosine pulse - it is possible to restrict the emission of the most energetic photons to take place only once per laser pulse. By contrast, in a sinusoidal-shaped laser field, two re-colliding electron wavepackets lead to emission at the highest photon energies, resulting in XUV bursts separated by half a period of the laser field.
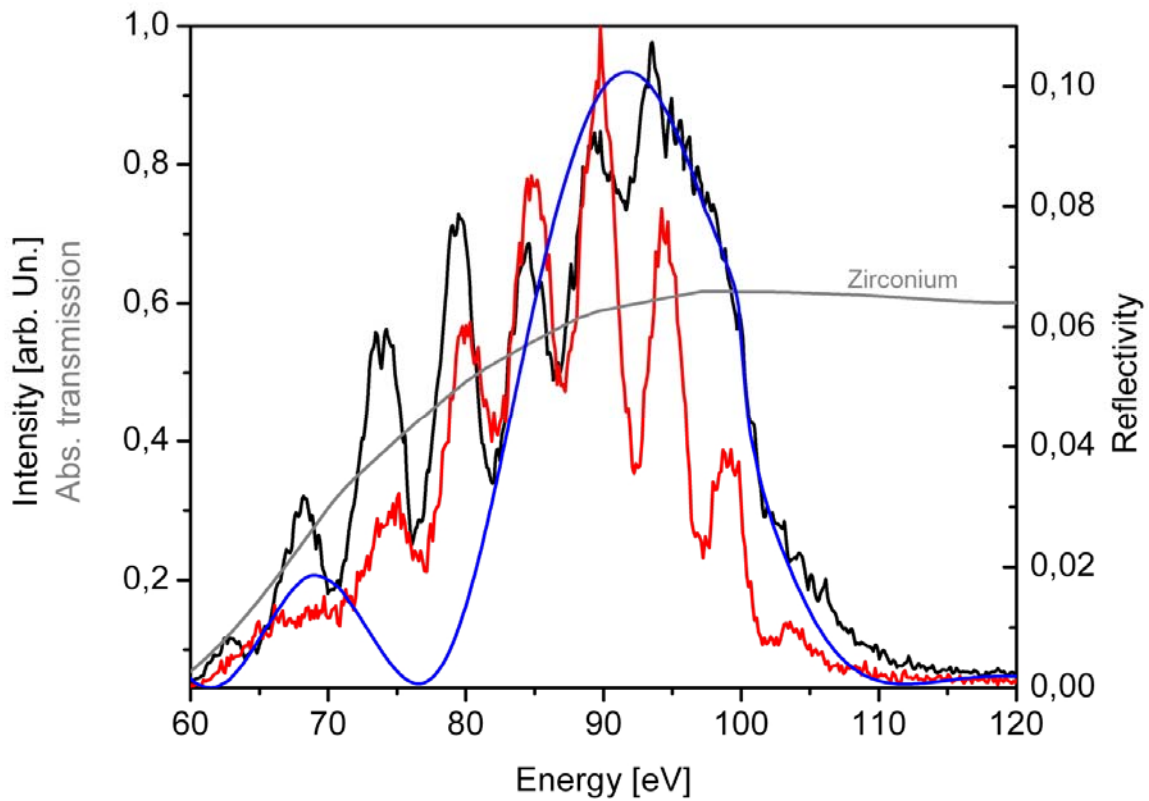
Fig. 3.14: XUV spectra emanating from the interaction of few-cycle phase stabilized laser pulses with Ne atoms after being transmitted through 1.5 μm of a free standing Zr foil. The spectra are integrated over ~300 shots of the laser. Red curve: Spectrum of the XUV pulses emitted by a sinusoidal few-cycle pulse while the black curve is the spectrum of XUV pulses generated by a cosine-pulse. The highly modulated spectrum associated to a sinusoidal waveform constitutes the spectra manifestation of a substantial amount of satellite in the time domain. The reflectivity of the 15.6 eV (FWHM) aperiodic multilayer mirror employed in the experiments presented here, is marked by a blue line. The grey curve shows the transmission of the 150 nm Zr foil used in the experiment (scale shown on left axis).

The extension of the XUV/X-ray spectrum associated with a single re-collision event and hence with the potential to form an isolated attosecond pulse is precisely linked to the intensity contrast between consecutive field maxima and thus *the duration* of the driving pulse. In the case of ~4.5-5 fs pulses utilized in this work, this contrast is expected to be approximately 20 eV and can therefore potentially support isolated XUV pulses down to a duration of less than 150 attoseconds. Figure 3.14 depicts XUV spectra integrated over 300 shots of the laser pulse for a carrier envelope phase of the driving field resulting in a >20 eV broad near-cutoff continuum (black line).

A CEP shift by π/2 with respect to the previous setting results in a highly modulated spectrum (red line). To fully utilize this extended continuum a *broadband* aperiodic multilayer mirror

was used, its reflectivity curve is shown in blue in Fig. 3.14. A secondary reflectance fringe (Kiessig fringe) in the lower energy part of the spectrum can be substantially suppressed by means of a thin Zr foil.

3.4.2 Isolation of a single attosecond pulse via spectral filtering with multilayer optics

The generation of isolated XUV attosecond pulse down to the sub-200 as regime has been hitherto limited by the lack of XUV optics and filters that could filter the continuum mentioned before and sufficiently suppress spectral components that lead to emergence of a satellite pulse.
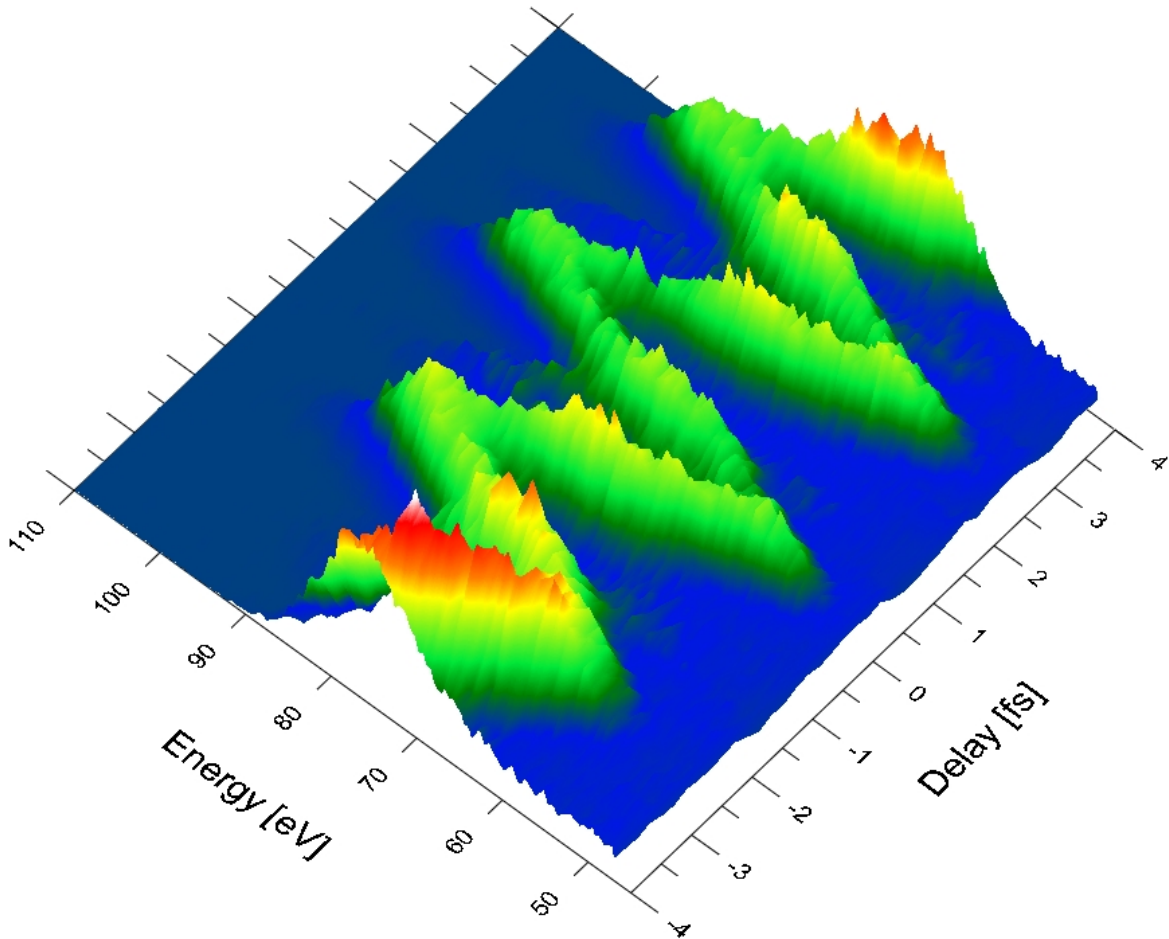
Fig. 3.15: Atomic transient recorder spectrogram generated by an XUV attosecond pulse shown in 3D contour representation. It comprises a series of ~70 electron spectra generated in Ne and recorded as a function of the delay between the XUV and the few-cycle laser pulse in steps of 100 as.

This limitation has been overcome in this work by using a specially designed aperiodic (i.e. *chirped*) Mo/Si multilayer mirror. Multilayer XUV mirrors consist of periodic or aperiodic stacks of alternating ultra-thin layers of two or more different materials (typical layer thick-

nesses 1-10 nm, typical layer numbers 10-500). Varying the layer thicknesses enables a controlled design of the center reflectivity, of the reflected bandwidth as well as of the spectral phase. The latter parameters affect the time response of the mirror upon reflection of an attosecond XUV pulse. While the bandwidth of a *periodic* XUV multilayer in first Bragg order is mainly limited by the number of contributing bi-layers N to $\Delta\lambda/\lambda = 1/N$ to be about 10 % of the reflected (cut-off photon) energy or less, broader reflection profiles can be realized by *aperiodic* multilayer stacks. Furthermore, the evolution of the spectral phase, which controls the spectral dispersion of the pulse and by that its temporal evolution, can be optimized and shaped by the interference structure of the multilayer mirror.
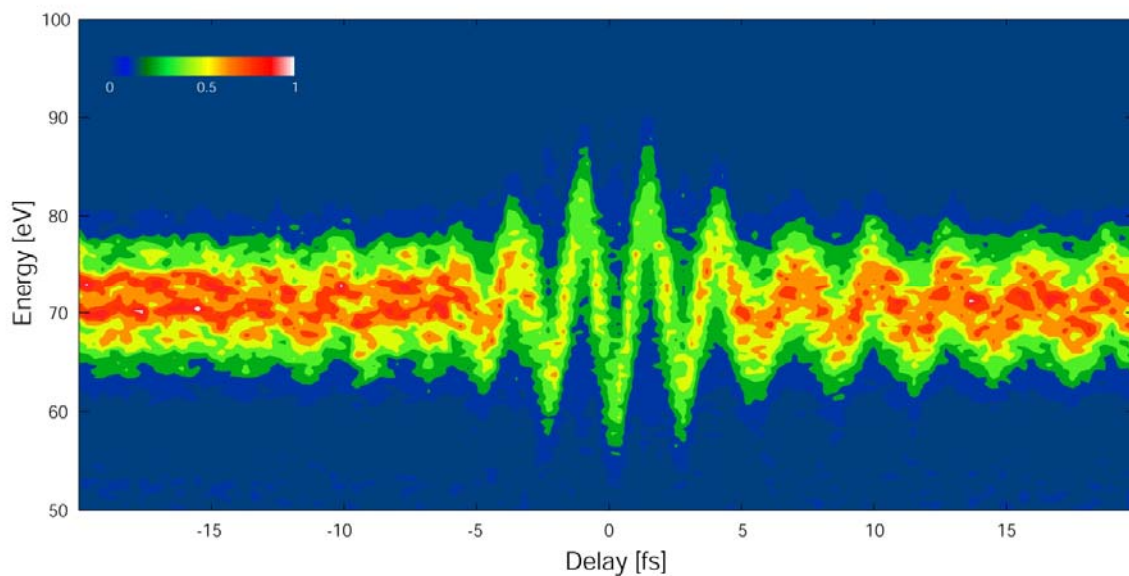
Fig. 3.16: Long range atomic transient recorder spectrogram generated by a 170 XUV attosecond pulse. A series of electron spectra generated in Ne have been recorded as a function of the delay between the XUV and the few-cycle laser pulse in steps of 300 as. The electron spectrometer is oriented such that it collects electrons emitted only in the direction of the polarization vector of the laser field utilizing the geometry presented in 3.1 . To ensure high resolving power, the streaking field is set to shift the electron distribution in energy by more than the half of the initial width, which corresponds to ~8 eV.

Over many years, small bandwidth, high reflectivity Mo/Si multilayer mirrors have been developed for the 80-100 eV photon energy range and have proven their capability for spectral filtering, dispersing and steering High Harmonics. While 250 as isolated XUV pulses have been generated and filtered at 93 eV by using a periodic Mo/Si multilayer with approx. 8.6 eV FWHM bandwidth, aperiodic multilayer mirrors can support a substantially broader bandwidth required for shorter XUV pulses. In this work, a coating design with a reflection bandwidth of ~16 eV FWHM and optimized dispersion characteristics was used, holding the po-

tential for producing isolated 150 as pulses. Even the compensation of an intrinsic spectral chirp of the incoming XUV pulse (resulting from the HHG process or propagation effects) by the group delay dispersion (GDD) of the XUV multilayer mirror ("chirped XUV mirror") over the whole reflected bandwidth is feasible. This will enable compression of the pulse to its Fourier limit.

3.4.3 Measurement of attosecond XUV pulses

The basic idea behind techniques developed for the characterization of XUV bursts, is the generation of a spectral replica of the attosecond pulse in a photoelectron bunch the temporal structure of which is probed by the ultrafast oscillation of the electric field of a laser pulse.

Assuming ionization of atoms by XUV attosecond pulses in the presence of a laser field $E_L(t)$ and detecting the generated electrons along the polarization direction of the field, an electron released at the moment t suffers a momentum shift Δp which is given by (cp. 1.3.2)

$$\Delta p(t) = e\int_t^\infty E_L(t')dt' = eA(t)$$

e: electron charge

$A(t)$: vector potential

Therefore, the ultrafast variation of the field amplitude maps the temporal evolution of the attosecond electron pulse to a corresponding momentum and electron distribution. These ideas are put into practice in a concept dubbed atomic transient recorder [33]. In practice, a series of electron spectra, acquired in different delay settings between the laser and the electron pulse (a spectrogram), offers the possibility of an accurate retrieval of the temporal structure of the electron pulse and consequently the XUV attosecond pulse, at the same time. The technique in that case is closely related to FROG (frequency resolved optical gating), where the gate for the characterization of the attosecond electron pulse is provided by the field oscillation. To this end, various reconstruction algorithms have been developed and allow not only the retrieval of the attosecond pulse but also the laser pulse (gate) simultaneously enabling metrology of optical fields.

For the characterization of the XUV pulses with the atomic transient recorder, the XUV continuum is reflected, filtered and focused by the multilayer mirror into a Ne gas nozzle along with the IR field. Two series of electron spectra as a function of the delay between the XUV and laser pulse are shown in false color representation in Figs. 3.15 and 3.16. Fig. 3.15 depicts a high resolution (100 as step in delay) high streaking field ($\Delta W > 10$ eV shift of the electron peak) scan. Fig. 3.16 shows a long range scan in delay with a scanning step of ~ 300 as.
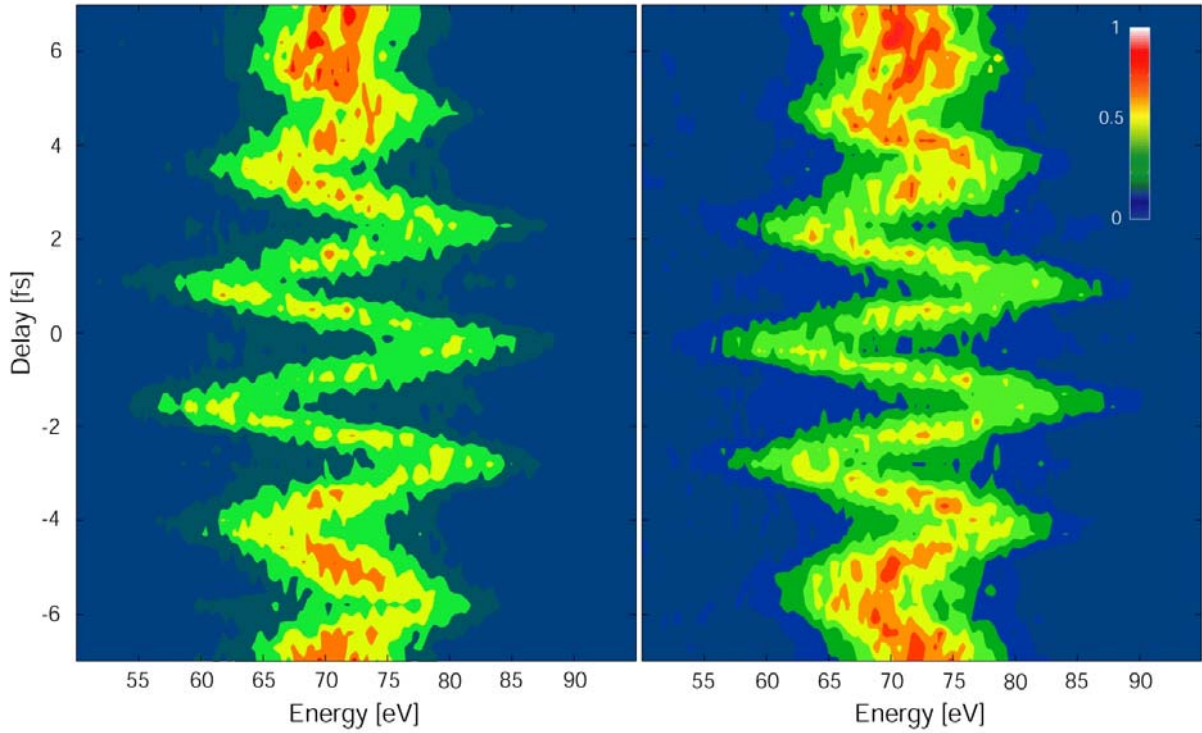
Fig. 3.17: Light wave oscillations of a phase stabilized few-cycle laser pulse recorded over a delay interval of ±7 fs around the envelope maximum of the laser field. The spectrogram showed in the left panel was taken for a certain setting of the carrier envelope phase close to a cosine-like pulse. The right panel shows the resulting spectrogram after repeating the measurement with the same settings after adding dispersion to change the waveform from a cosine to a -cosine pulse. The change by π of the carrier envelope phase results in the spatial inversion of the field oscillations of the NIR driver pulse as can be clearly observed by comparing the two spectrograms.

For the retrieval of the duration of the attosecond pulse, a software based on the theoretical and retrieval principles discussed and referred to in the previous section was developed. The algorithm accounts for possible satellite pulses, while all key parameters including the chirp of the attosecond pulse and the temporal shape of the laser field are left free to be reconstructed invoking the power of a genetic algorithm. The retrieved pulse duration was 170 ± 10 *as* and therefore approximately 5% longer compared to the transform limited pulse supported by the reflected spectral bandwidth (approximately 150 as). The satellite pulse was found to contain about 17 % of the total photon number.

As pointed out above, the electric field of the XUV attosecond pulse and that of the laser pulse can be reconstructed from the same spectrogram. However, the prerequisites regarding the spectrogram are not the same. The former can be characterized with sufficient accuracy utilizing solely spectra recorded over a delay range that spans one field oscillation; the latter

can be accessed only if the attosecond pulse samples at least the range of 5-10 field oscillations for a few-cycle laser pulse, necessary to probe its built-up and disappearance. The retrieved duration (FWHM) of the near-infrared laser pulse was 4.7 fs.

To demonstrate the degree of control and reproducibility of the waveform of the few-cycle pulses, the phase of the driving field was shifted by π (as to switch from a cosine to an anti-cosine driving waveform) and a similar scan as in Figure 3.16 was repeated but limited in delay within ± 7 fs around the peak of the pulse. Both series of spectra are depicted in Fig. 3.17.

A complete characterization of a new source always entails a photon yield measurement. Following the procedure described in detail in section 3.2.2, employing a yield-calibrated X-ray CCD and calculating the number of photons in the focus utilizing the tabulated transmission of the Zr filters, (48-62 % @ 80-100 eV) and the measured peak reflectivity (by Synchrotron Radiation reflectometry) of the 15,6 eV FWHM bandwidth multilayer ~5 %, the photon number was derived. The analysis yielded ~3.6 10^8 photons/sec for the attosecond pulse delivered into the target. The flux at the HHG source was more than an order of magnitude higher for the same spectral range suggesting that further improvements afford promise for substantially higher photon flux delivered to experiments. This photon flux is slightly higher than the flux generated by the previous source (250 as @ 95 eV, 8.6 eV FWHM) relying on short driver pulses and suggests that generating attosecond pulses with considerably shorter duration is attainable while maintaining other key parameters. The following section (3.5) elucidates the experiments triggered by this idea.

3.5 Progressing the resolution towards the atomic unit of time

As a result of the improvements of the laser source (cp. Chapter 2) used in the experiments introduced in this work, the generation of attosecond pulses confined to even shorter times was possible. This chapter presents the routine generation of isolated sub-100-as XUV pulses with a flux of greater than 10^{11} photons/s, exceeding by several orders of magnitude the flux of sources known so far. Profiting from the very high, reliable statistics in the recorded data, a 10% measurement accuracy in the sub-100 as regime suggests that the temporal resolution of this pump-probe sampling scheme approaches the atomic unit of time (~ 24 as, the estimated time the electron takes to revolve the atomic core once).

3.5.1 Identifying the best CE-phase

The findings on the formation of the high-harmonic-cut-off depicted in Fig. 3.4 along with detailed experiments on the carrier envelope phase dependence of the generated spectra are summarized in Fig. 3.18. The three left panels show representative NIR electric waveforms

$$E_L(t) = a_L(t)e^{-i(\omega_L T + \varphi)} + c.c.$$

for three different settings of the carrier-envelope phase φ with the ionization probabilities at the field oscillation peaks. For pulses this short the ionization probability almost vanishes outside the central wave cycle. Fig. 3.18 shows the calculated trajectories for the part of the launched wave packets with the highest energy. The spectral emission for these different half cycles is depicted in the panels on the right hand side of Fig. 3.18.

Fig. 3.19 shows measured spectra in accompaniment with a 1-D modeling of the single-cycle interaction of ionizing NIR radiation with an ensemble of neon atoms. The modeling (V. Yakovlev) was done using the NIR field shape retrieved from the streaking measurement shown in Fig. 3.20. Experimentally, only the spectrum formed by the superposition of the half-cycle contributions is accessible (see Section 3.1), the understanding of the formation, however, leads to the development of the ultrashort attosecond pulses presented here. As a direct consequence of the shortness of the driving NIR pulses, the generation of the broadest, continuous photon spectrum takes places in a regime antithetical to the established schemes. As can be seen in Fig. 3.18, the highest energetic photons are still produced by a cosine-shaped waveform (0° in the case depicted), nevertheless the broadest usable continuum is generated by an almost sinusoidal waveform (+70° is shown in the figure), where two wave

packets are launched with the same final energy but with a yield different by more than an order of magnitude. The little remaining modulation of the spectrum caused by the interfe-
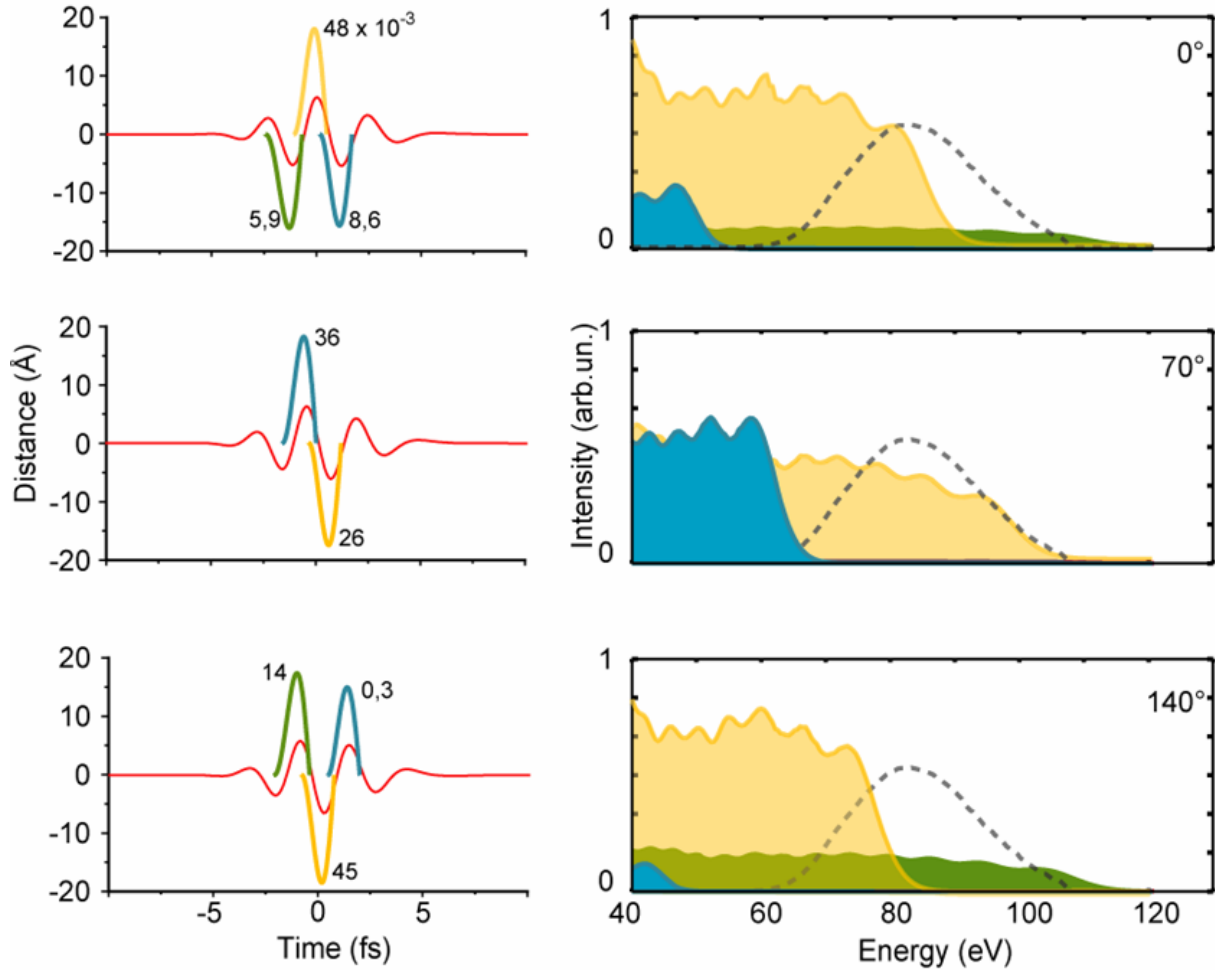

Fig. 3.18: Soft-X-ray emission driven by a quasi-monocycle laser pulse. Highest energy electron wave packets released at adjacent field maxima are driven by the laser field E(t) to re-collide with their parent ion some 2/3 of a period later and emit soft-x-rays. Whereas a near cosine pulse (upper panel) ($\varphi \sim 0°$) is generating the highest cut-off energy in agreement to previous experiments, the yield of the photoemission is poor due to the low ionization rate at the instance of release. Furthermore, within the mirror bandwidth (grey dotted line) the contribution of two half-cycle cut-offs leads to attosecond pulses with a strong satellite content. A waveform more close to sinusoidal shape (middle panel) generates two trajectories resulting in photons of a substantially different energy range. This phase setting favors the generation of attosecond pulses with higher intensity and low satellite content. The lower panel shows the situation for a phase setting where two trajectories contribute almost equally to the reflected light and therefore form a strong satellite pulse (c.p. Fig. 3.22). The curved colored lines in the left panels show the calculated excursion distances and trajectories for the wave packets re-colliding wit the ionic core. The given value describes the calculated absolute ionization probability for the respective half-cycle. The attosecond pulses presented here are produced for a carrier envelope phase setting in accordance with the setting depicted in the middle panel.

rence of those two contributions allows only for a sub-% satellite pulse after the low-pass-filtering. At the same time, the emission by the third trajectory is shifted to even lower energies, facilitating the use of an even more extended bandwidth for the formation of attosecond pulses virtually free of temporal satellites upon spectral isolation of the broadband emission. Fig. 3.19 shows a series of electron spectra generated by ionizing neon with the soft X-ray pulses as a function of the carrier-envelope-phase of the driving NIR light field. Simulations corresponding to the experimental parameters are shown in Fig. 3.19 b. Although there are aberrations between the measured and the simulated spectra, the general shape is very well re-
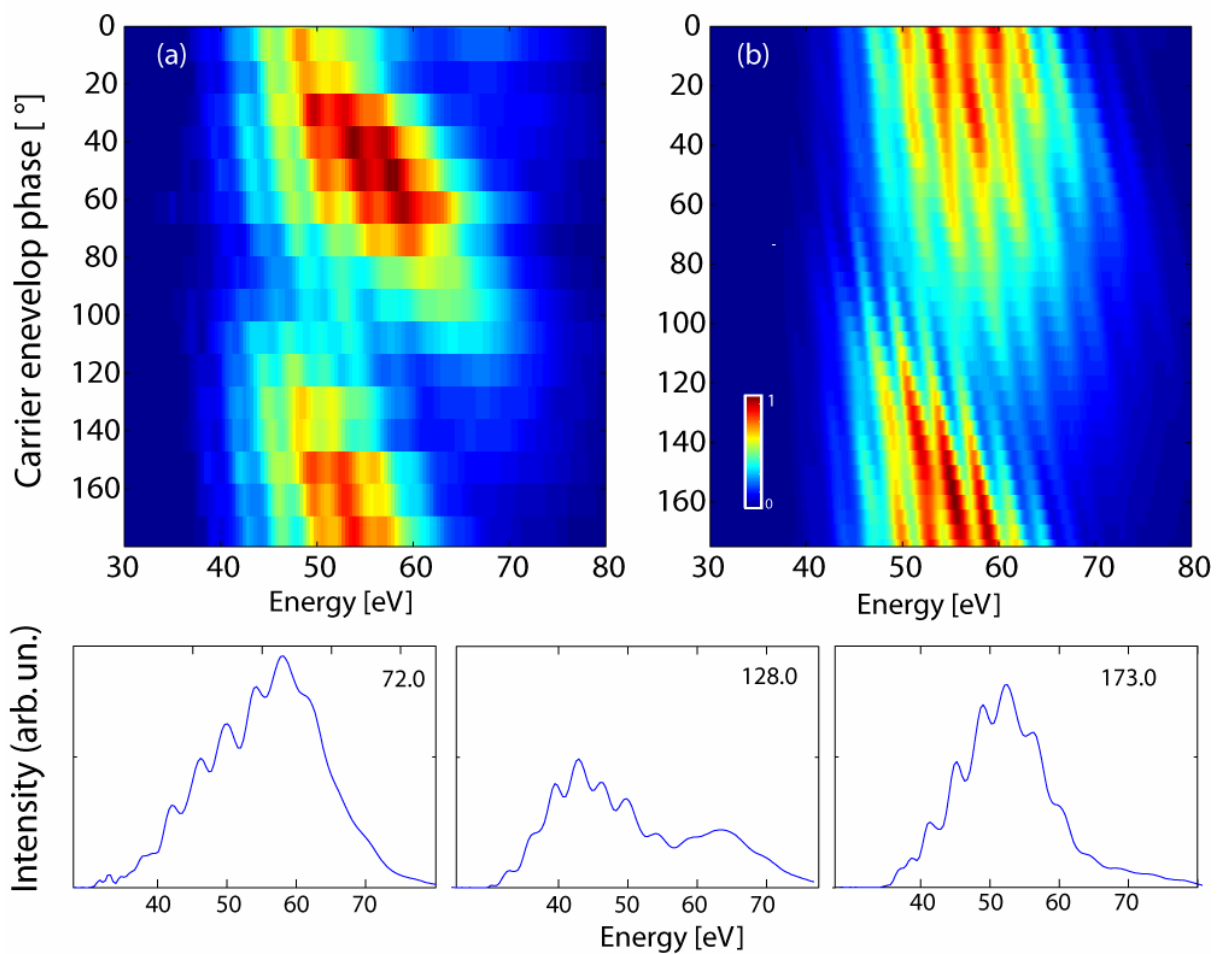
Fig. 3.19: Light waveform control of Soft-X-ray emission. The upper two panels show series of electron spectra recorded as a function of the carrier envelope phase (CEP) of the driving laser pulses (a) measured and (b) calculated. The lower panels show representative spectra at different phase settings (small number: phase setting in degree relative to a perfect cosine pulse). Whereas in the middle panel the phase is set to enhance the emission of more than one half cycle of the driving laser pulse, the first and the third panel correspond to emission primarily from one half cycle. This robust feature permits selecting a single soft–X-ray pulse with the minimum amount of satellite and the highest photon yield.

produced. In the small panels, representative line-outs of the electron spectrum for different phase settings are shown. Spectra recorded for the setting $\varphi = 128°$ correspond to the emission of two trajectories as manifested by the two-bump structure within the reflectance bandwidth of the multilayer mirror. Spectra recorded for CE-phases of 72° and 173° have a central energy being a little lower than in the other cases, the yield, however, is almost doubled and the appearance of only a single hump in the spectrum suggests that this setting is favorable for the generation of single as-pulses. For the presented experiment, the carrier-envelope phase of the laser field was adjusted to generate spectra similar to case 72° with a FWHM of ~ 27eV centered at 65 eV. According to the scheme of the atomic transient recorder [33, 47] the temporal characterization of the soft-X-ray supercontinuum was performed relying on the action of a dressing laser field to the photoelectron spectrum. The laser field in precise synchrony with the attosecond pulse streaks as explained in the section 1.3.2 the photoelectrons that are detected along the direction of the laser electric field vector. Fig. 3.20 shows a series of electron spectra recorded for different delays between the ionizing XUV-pulse and the streaking NIR-laser field. To ensure high resolution, the laser field strength is adjusted as to introduce a substantial energy shift (±15 eV) of the electrons if released at the peak of the laser electric field. Owed to the very high flux of the source and the improved signal acquisition techniques, it was possible to record these streaking spectrograms with unprecedented statistics and very fine delay steps (80 *as*) to achieve a reliable dataset for the analysis. In total, a high-resolution scan takes around 12 minutes with the new techniques, permitting in-depth studies of the influence of small changes in the CE-phase to the recorded spectrogram.

3.5.2 FROG retrieval of 80 attosecond pulses

Analysis of the spectrogram was performed by using an adaptive computer code that was developed in our group by J. Gagnon and V. Yakovlev. It is based on the generalized projection algorithm discussed in [65]. In analogy to the established pulse characterization techniques that have been used in the visible realm (as for example in Fig. 2.4), techniques are developed for the quantum-optical area. In particular, the technique used for the retrieval of the data presented here applies the concepts behind frequency-resolved optical gating (FROG) to attosecond electron streaking measurements. The FROG methodology is based on the acquisition of a spectrogram and its inversion into a pulse $P(t)$ and gate $G(t)$ function, both complex valued functions with t defining a delay between them.
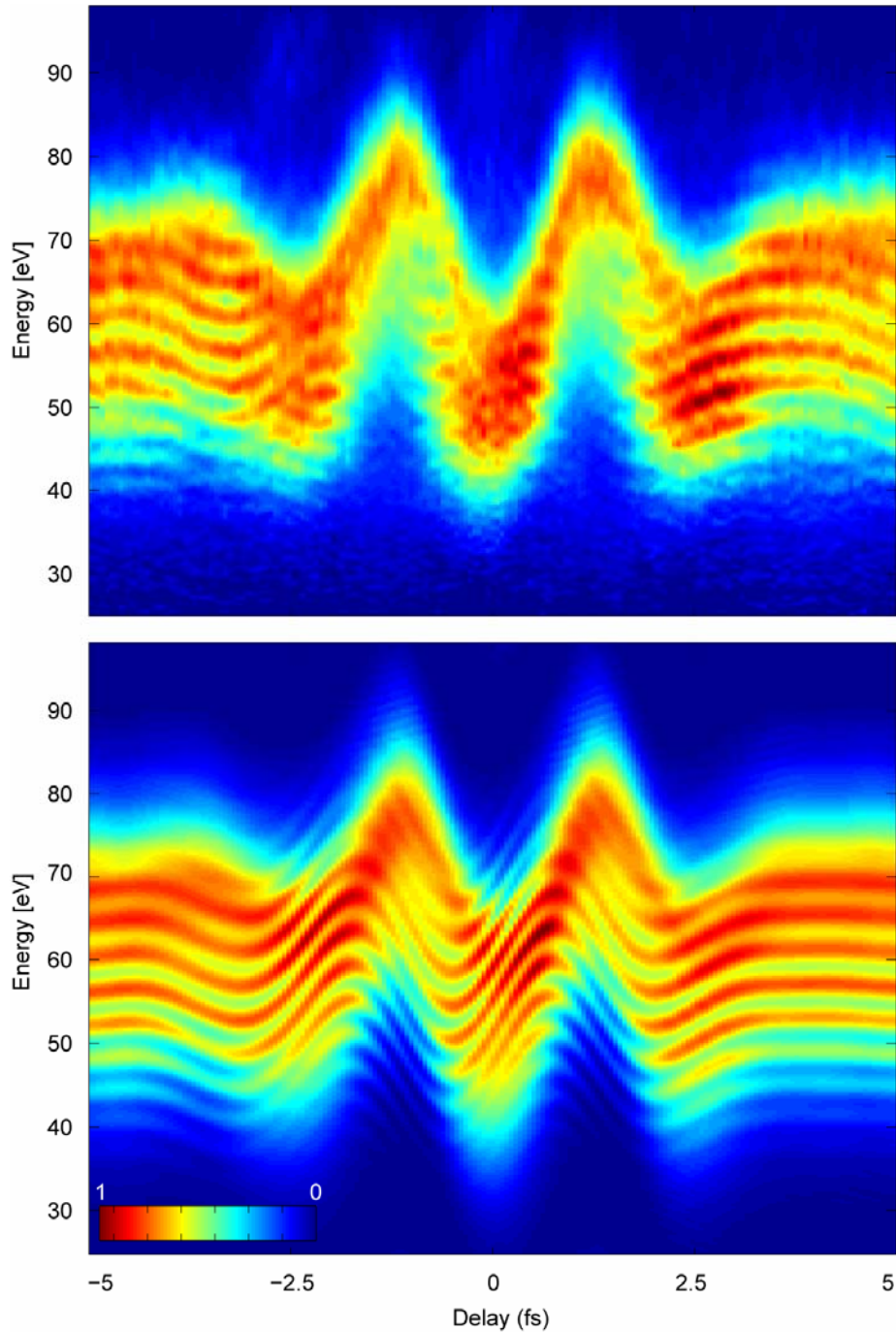
Fig. 3.20: Measured and reconstructed atomic transient recorder spectrograms of a sub-100 as XUV pulse. An electron wave packet released via the impulsive ionization of Neon atoms by a ~ 23 eV broad XUV attosecond pulse centered at 80 eV is recorded as a function of the delay (0.08 fs) between the XUV pulse and the quasi-monocycle laser pulse. The approximately 15 eV shift suffered by the electrons comprising a substantial fraction of its unperturbed width warrants sufficient temporal resolution to accurately resolve the temporal structure of the broadband photoemission. In the measured spectrogram (upper panel), the fringe contrast appearing due to the interference of the contributions of two subsequent half cycles is slightly enhanced; the periodicity of the fringes is close to the resolution of the spectrometer employed. The lower panel shows the reconstructed spectrogram after ~ 10^3 iterations of the LSGP (least square generalized projection) algorithm.

A spectrogram is composed by a pulse- and gate-pair according to

$$\tilde{S}(\omega,t) = \int\limits_{-\infty}^{\infty} P(t)G(t+\tau)e^{i\omega t}dt$$

and is therefore recorded as a sequence of spectra of a delay dependant signal. Upon taking the square of the modulus, all information about the phases of the individual functions is lost; it survives, however, in the spectrogram. The inversion of such a spectrogram is a two-dimensional phase retrieval problem that in general possesses a quasi-unique solution for *P(t)* and *G(t)* under the assumption of meaningful parameters for pulse and gate. For conventional FROG techniques this retrieval is further reduced to the characterization of one single function *P(t)* whilst *G(t)* is the result of the pulse function undergoing some nonlinear optical process.

To extend this technique to attosecond XUV pulses that, by definition, exhibit a large bandwidth and are therefore susceptible to chromatic dispersion and furthermore suffer by their little pulse-energy to trigger nonlinear processes, an alternative conceptualization was proposed [66].

The experimental implementation, known as *attosecond streak camera* [46, 66, 21], transfers the temporal structure of the XUV pulse into a kinetic energy spectrum of electrons photoionized in an atomic gas sample. The kinetic energy spectrum of these electrons can, under the assumptions connected to the strong-field-approximation and the additional assumption, that the final classical momentum of the photo-ionized electron is large compared to the streaking vector potential, be expressed as

$$S(\varepsilon,\tau) = \left| \int\limits_{-\infty}^{\infty} E_{xuv}(t)e^{-i\phi(t+\tau)}e^{i\varepsilon \cdot t}dt \right|^2$$

$$\phi(t+\tau) = \int\limits_{t+\tau}^{\infty} (\sqrt{2\varepsilon_0}\,A(t') + \frac{1}{2}A^2(t'))dt'$$

where units of electron energy ε have been used instead of momentum *p*. In this form, the electron spectrum *S(ε,t)* is an ample spectrogram as defined above, the XUV pulse E_{xuv} being gated by a complex phase factor $e^{i\Phi(t+\tau)}$. The laser pulse is described as *A(t)*, the vector potential connected to the light field oscillation and $\phi(t+\tau)$ is the quantum phase that the electron
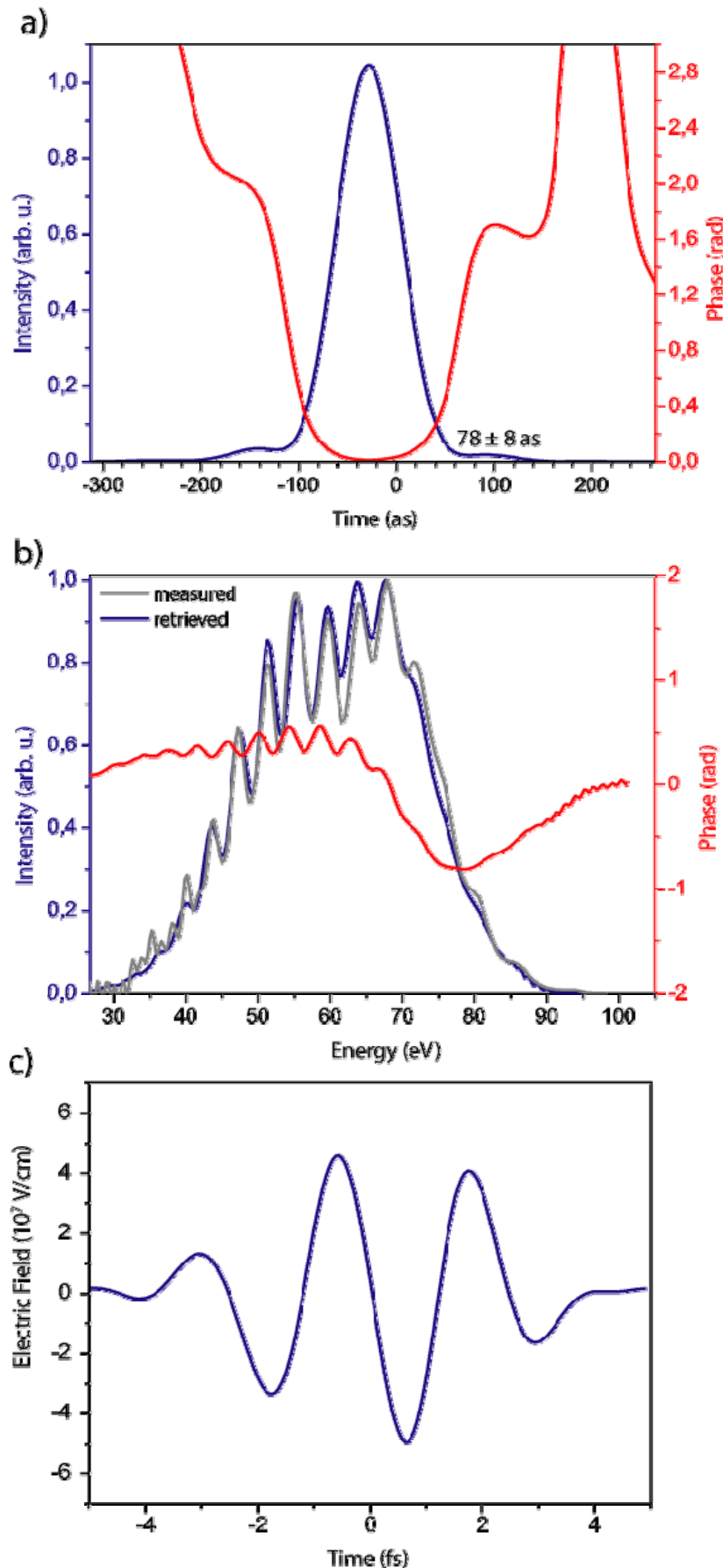
Fig. 3.21: Temporal profile and spectral phase of a sub-100 as pulse. The upper panel shows the temporal profile and phase of the retrieved pulse. The intrinsic chirp of the soft-X-ray emission is compensated by 300 nm of Zr foil introduced into the XUV beam. The pulse carries a slight positive chirp (~900 as^2) which is left uncompensated. This chirp has resulted in approximately 10% stretching of the pulse with respect to the Fourier limit which is approximately 70 as. Middle panel: Electron spectrum measured (grey) and retrieved (blue), and phase. The ripples in the spectral phase at the low-energy part of the spectrum indicate retrieval of a satellite pulse, whose retrieved intensity is below 2% with respect to the main pulse. The faint shadow in the measured spectrogram in Fig. 3.20 that is visible phase-shifted by π with respect to the main streaking trace can be attributed to this satellite emission. The lower panel shows the retrieved electric field evolution of the laser pulse used to generate the shown spectra. The waveform shows two field maxima with almost balanced strength, it is therefore rather a sine than a cosine pulse.

acquires during its interaction with the laser field, from the moment of its ionization into the continuum [68]. As pointed out in chapter 3, experimentally, the same IR pulse is used for the generation of the high-harmonic-radiation as well as for streaking. For the measurement presented here, the retrieved spectrogram is shown in Fig. 3.20 upper panel, the retrieved temporal profile and phase of the attosecond pulse are shown in Fig. 3.21. The very good agreement of measurement and retrieval is apparent in the almost perfect equivalence of measured and retrieved energy spectrum of the XUV pulses.

The ascertained duration of the attosecond pulse is 78±8 *as*, the pulse carries a small positive chirp of ~900 *as²* leading to a stretching of the pulse to approximately 6 *as* above the Fourier limited duration amounting to 75 *as*. By taking the dispersion of the 300 nm Zirconium foil, through which the pulse is transmitted into consideration, the inherent chirp of the attosecond pulse in the source can be backtracked. The filter is introduced into the beam to suppress low harmonic light on the one and laser light on the other hand and acts as spatial filter as explained in Section 3.1. Comparison with tabulated values shows that zirconium imposes a negative chirp to transmitted XUV light. For a 300 nm Zr-foil and for 80 eV photons, the chirp is in excess of -4000 as². This suggests a positively chirped emission (~140 as) at the XUV source for the bandwidth used here; a positively chirped emission dominated by the short trajectory is in agreement with the semi-classical picture for the formation of High-harmonic-radiation. Both the experimental and the retrieved spectrogram show fringes suggesting the presence of a satellite pulse. The algorithm allows for an accurate retrieval of the satellite pulse. Compared to the main XUV pulse, the satellite amplitude is about 1%.

Comparison of the measured and the retrieved spectrum in Fig. 3.21 emphasizes the accuracy of the retrieval of the spectral phase. The measured (grey) line shows only very little deviations from the retrieved photon spectrum (blue line) that is shifted by the ionization potential of neon. In connection with FROG techniques, usually the "FROG-error" is given as a measure for the quality of the retrieved data, although there is no clear definition for that number. The low number of $\sim 6 \times 10^{-2}$ that was achieved by the code used for the presented retrieval affirms the reliability of the acquired pulse characteristics further.
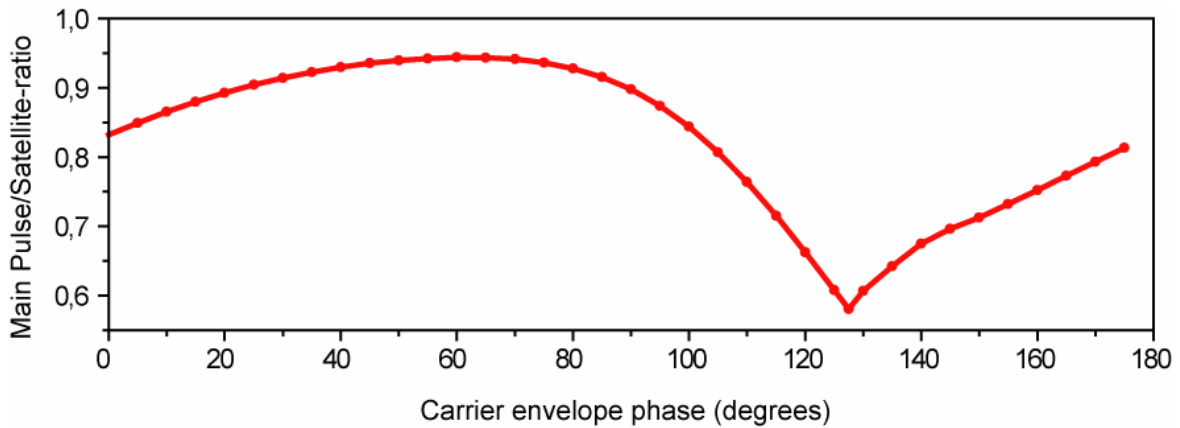
Fig. 3.22: The satellite content depending on the carrier-envelope-phase setting. For the scenario presented in Fig. 3.18 concerning the mirror bandwidth and the spectral extend of the generated harmonic-radiation continuum, the red line displays the satellite pulse content of the overall XUV intensity upon reflection on the multilayer mirror. As a result of the significant shorter laser pulses driving the harmonic generation and the favorable mirror-reflectivity / filter transmittance features of the presented experiment, in contrast to previous work only very few phase settings (around 127,5° with respect to a perfect cosine-like pulse) give rise to the emission of a considerable low amount of satellite pulse rivaling the intensity of the main pulse.

As the presented source establishes a technique to probe processes that evolve on an ultrashort timescale, the actual temporal resolution should be identified. The shortest feature discernible in the experimental trace is limited by the error inherent in the measurement of the experimental parameters. According to [68], an error bar on the retrieved pulse's amplitude and phase can be defined. Following this analysis, in the case of the measurement presented here, the error on the retrieved pulse duration is ±8 as. The error bars that are not shown in Fig. 3.21 due to the equivocality of their definition on the retrieved phase and amplitude would allow for only very little changes in the curves. The error bars show that the retrieved phase becomes more and more ambiguous as the pulse amplitude vanishes. Even more important information that can be derived from a detailed analysis of the experimental uncertainties is the delay-step-size required to resolve subtle features on the experimental trace. The attosecond pulse duration promises an unprecedented temporal resolution only in combination with small delay steps in the spectrogram. Small delay steps, however, put challenging demands on the long-term stability of the whole system.

3.5.3 Eliminating satellite pulses

A common feature of setups generating harmonic radiation is the occurrence of one or two small satellites at half an optical cycle away from the main pulse. Consequently, the spectral shifts the released photoelectrons undergo are offset by half a laser period. In the recorded photo-electron spectra this becomes visible as electrons that are accelerated and electrons that are decelerated at the same delay step. At zero-crossings of the vector potential, the spectra evoked by the main- and the satellite-XUV-pulse have common components and therefore interfere in the energy domain, causing the appearance of spectral fringes (Fig. 3.20). The behavior of this phenomenon is analyzed in [69]. Due to their sensitivity, the fringes are easily affected by defects in the acquisition process. Since their spacing is twice the laser photon energy, a sufficient energy resolution of the electron spectrometer has to be ensured. More-over, the spectral position of the fringes changes under the influence of the streaking field (cp. Fig. 3.20 b). To ensure a reliable retrieval based on the FROG algorithm, it is essential to re-solve the fringes for at least most of the delay steps in the spectrogram implying a condition on the delay-step-resolution required. In the areas where the fringes are steep, the distance between minimum and maximum can be estimated as

$$\partial\tau \approx \frac{1.5}{\Delta E}$$

where $\delta\tau$ is measured in fs and ΔE denotes the spectral shift in eV with respect to the central energy of the electrons. In experimentally useful units this amounts to

$$\Delta\tau \approx \frac{1.7 \cdot 10^9}{\lambda_L \sqrt{E_0 \cdot I_L}} \ .$$

λ_L laser wavelength [nm]

E_0 central energy [eV]

I_L laser intensity [W/cm²]

This equation sets an upper limit on the delay step that can be used to properly record the in-terference fringes in a streaking spectrogram; the step size of 80 as used to record the spectro-gram in Fig. 3.20 complies with this demand.

Different waveforms characterized by means of the attosecond streak camera showing fea-tures like uncompensated higher order dispersion (Fig. 3.23) or chirped XUV emission (Fig. 3.24) are depicted below. Fig. 3.25 shows a series of recorded spectrograms while changing the CEP setting and thus affecting the temporal structure of the generated attosecond pulse.
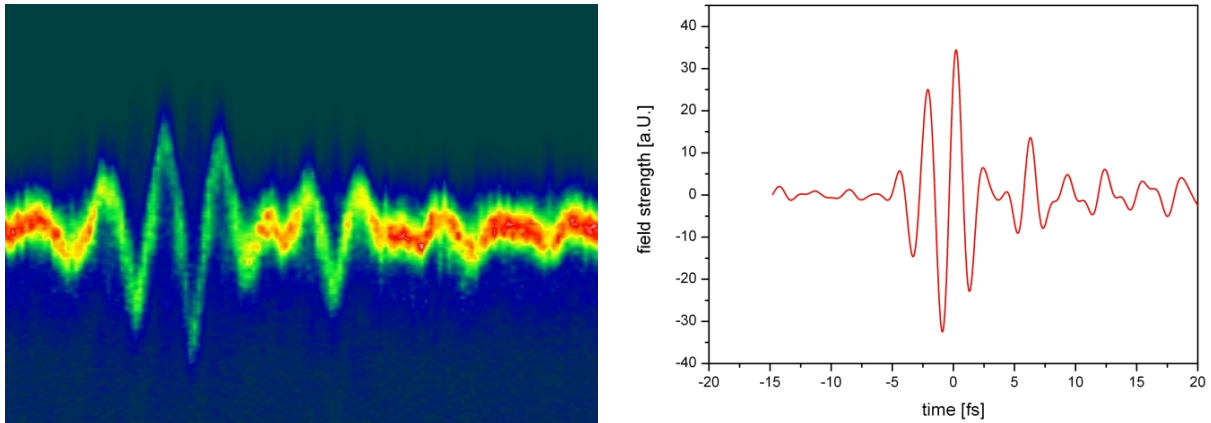
Fig. 3.23: Curious waveforms under investigation. Streaking spectrograms (here: like introduced before electron energy vs. temporal delay) characterize the soft-X-ray pulse as well as the waveform used to streak the released electrons. In contrast with other techniques (ACF, FROG) that investigate visible laser pulses, the measurement gives direct access to the time- and amplitude-evolution of the pulses (precisely: the vector potential) and is by definition not limited in bandwidth. The left panel shows the spectrogram created by a short (3,9 fs FWHM) NIR waveform. The smaller revival of the field oscillation after the main pulse is the manifestation of a substantial amount of uncompensated higher-order phase components. The right panel shows the derivative of the first momentum of the spectrogram, i.e. the electric field of the investigated pulse. The streaking spectrogram shown left is taken using a multilayer mirror with a relatively narrow bandwidth of ∼ 11 eV centered at 90 eV. The Fourier limit for such a spectral extend is around 190 as. The huge applied streaking field shifts the electron spectra around its peaks by more than 30 eV, advertising the large temporal resolution of the atomic transient recorder.
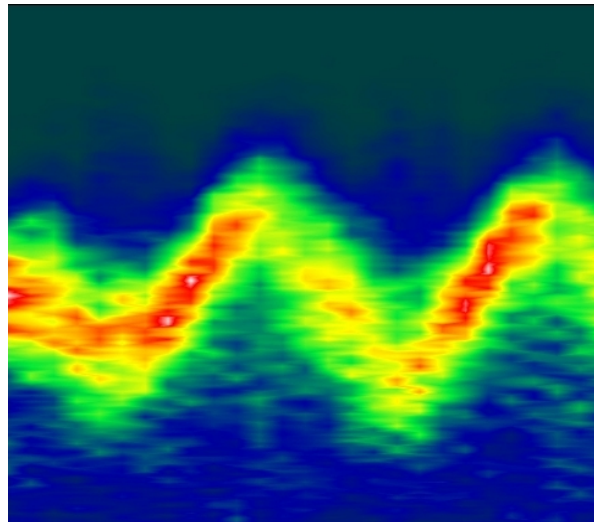
Fig. 3.24: Curious waveforms under investigation II. A possible chirp of the attosecond pulse used to generate a spectrogram leads to spectral broadening or compression of the field-free photoelectron spectrum depending on the sign of the laser field. The recorded spectrogram shown here exhibits alternating a compression of the spectrum at the rising and a broadening at the sloping edge of the laser electric field, a clear indication of (positive) chirp of the attosecond pulse employed in this measurement (cp. Fig. 1.7).
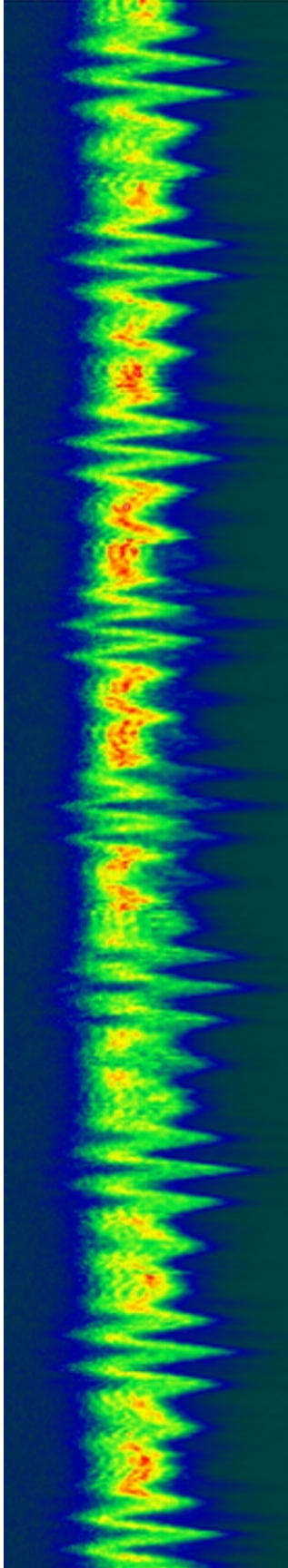
Fig. 3.25: Sensitivity of the streaking spectrogram to changes in the carrier-envelope-phase. The figure shows 9 spectrograms taken subsequently. After each spectrogram, the carrier envelope phase of the driving NIR laser field was changed by $\pi/8$ such to record a full cycle of π. To form the attosecond pulse, the same set of 300 nm Zirconium filter and the broadband multilayer mirror as for the 80 as measurement was used. By attenuating the intensity of the NIR driver laser, the cut-off energy of the harmonic radiation was lowered to reduce the effective bandwidth of the mirror (cp. Fig. 3.5). The bandwidth demonstrated here (~15 eV), holds the potential for the generation of 140 as pulses, provided the setting of the carrier-envelope-phase of the laser field is well chosen. For the very short NIR driver pulses employed in this experiment, the phase setting that performs best in terms of main-XUV-pulse- / satellite-contrast is, as pointed out above (cp. Fig 3.18), not defined by a cosine-shaped field evolution but rather by a electric field that is characterized by a sinusoidal waveform. The streaking spectrograms on the left hand side, showing the vector-potential of the employed pulses support this idea: the cleanest streaking traces (e.g. the second trace from above) show two oscillations with almost balanced intensity. In the context of the short driver pulses another fact can be extracted from the figure: The emission of an isolated, clean attosecond pulse is favored by the experimental setting described above. For only a carrier-envelope-phase range comprising $\pi/4$ (two spectrograms at step size $\pi/8$), the breakdown of the single emission can be observed (5th & 6th trace from above). In contrast to measurements presented so far, that rely on the same technique but where using longer driver pulses, this novelty drastically releases the demands on the phase-stability and makes the overall experimental technique more reliable and stable.

Chapter 4

Studies on laser ionization and inner-atomic electron-electron interactions

Exposing atoms to intense light fields generally results in the deliberation of electrons from the atomic electron sheath; the field ionization. The established understanding describes this process as tunneling of the electron through the binding potential that is suppressed by the light field. The present experimental knowledge about ionization in general is integrated over time and intensity. After summarizing the achievements regarding better time resolution in the previous chapter, this chapter is devoted to the description of the experiments that were performed in the course of this work to surmount these limits:

1. The first real time study on electron tunneling [70]

2. Time resolved studies on the electron-electron interaction populating shake-up states

3. First intensity selective studies on laser ionization

4.1 Attosecond real-time observation of electron tunneling in atoms

Light-induced electron tunneling is the most elementary process in strong-field interactions. With the advances in ultrashort light pulse generation, light fields with strength comparable to the potential energy of electrons bound to the nucleus are routinely available. For an intense laser pulse near the peaks of its oscillations, the electric field rivals the binding potential of the nucleus; for a cosine like laser pulse, whose intensity is adjusted to overcome the ionization threshold only within the central, most intense half cycle, the ionization is confined to a single time interval lasting less than 500 as (cp. Fig. 4.1). During this time-interval, the laser electric field suppresses the binding potential of the nucleus so strongly, that electrons can tunnel through the remaining coulomb barrier. The liberation of electrons from their atomic bound state, or more general, the interaction of electrons with light in the presence of an atom, is the primary step in strong field interactions. The proposal that tunneling through the atomic binding potential is the underlying process was made by Keldysh [71] and successors on this idea. The Keldysh theory predicts, that ionization is confined to short time intervals around the pulse peaks if the dimensionless parameter

$$\gamma = \frac{\omega_L \sqrt{2mW_b}}{|e|E_0}$$

is less than one. The amplitude and the angular frequency of the laser field are included as E_0 and ω_0. W_b, e and m are the binding energy, the charge and the mass of an electron, respectively. It should be noted that γ scales inversely with the laser electric field. The expression is valid under the assumption that the binding potential is significantly larger than the photon energy and assumes a laser field according to $E_L(t) = E_0 \varepsilon(t) \cos(\omega_L t + \varphi)$ with $\varepsilon(t)$ the amplitude envelope function.
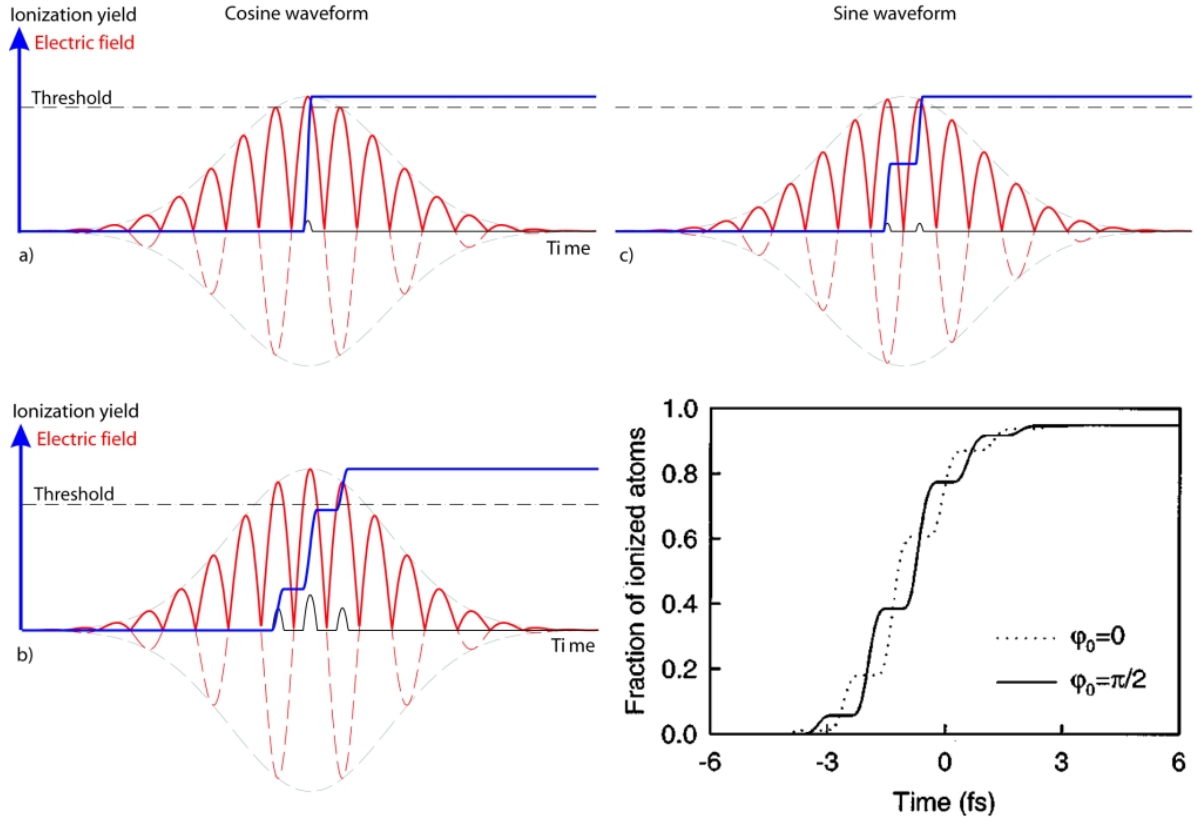

Fig. 4.1: The observed tunneling ionization is strongly intensity dependent and sensitively responds in the case of few-cycle pulses to changes in the carrier envelope phase. Panel a) and b) show different intensity settings for a cosine-shaped waveform. Whereas in the first panel, the ionization potential is only exceeded by one half-cycle, leading to a single step in the measured ion yield, the second one clarifies the occurrence of multiple steps for higher NIR probe intensities. Panel c) shows the phase dependence, a sine shape waveform exceeds the ionization potential even-numbered times; the ion yield therefore features at least two steps. The last panel shows the calculated phase dependence for ionization of helium assuming a laser pulse with τ_L = 5 fs, I_0 = 4 x 10^{15} W/cm² and λ_L = 800 nm. [5]. The dotted and the dashed line correspond approximately to a cosine and a sine pulse.

Recently, it turned out, that tunneling remains the dominating process in laser ionization even for γ-values up to three [72], representing conditions where the binding potential and the ionizing light field vary during tunneling (non-adiabatic regime).

4.1.1 Attosecond probing of electron dynamics

Different options for attosecond sampling of electron motion in the scope of the techniques presented in this work are illustrated in Fig. 4.2. A subfemtosecond XUV pulse triggers the motion by exciting a valence or core electron, the unfolding excitation and relaxation is probed by a time delayed NIR (near infrared) pulse. In principle, the probe pulse could be a replica of the excitation pulse, however, the low flux of the available subfemtosecond pulse sources and the low absorption cross sections suggest the use of a controlled few-cycle wave of NIR light. In combination with a process that is highly nonlinear in its response to the intensity, the laser pulses may replace the second subfemtosecond pulse in starting or probing electron dynamics. Here, the nonlinear interaction of the light wave with bound electronic states is studied. Ionization of weakly bound states occurs in subfemtosecond steps and hence holds the potential of probing intra-atomic electron dynamics by means of *attosecond tunneling*. Energetic photo-excitation as well as subsequent rearrangement via Auger decay are usually accompanied by transitions to unoccupied orbitals via "shake-up" (Fig. 4.2 d-f). The population of these states is probed via optical field ionization by a strong, few-cycle, visible laser pulse of variable time delay Δt with respect to the XUV excitation by measuring the evolution of the ion yield of the different charge states resulting from the XUV-pump/NIR-probe exposure (Fig. 4.2 d) as a function of Δt.

As diagrammed in Fig. 4.2 d-f, the shake-up process usually populates a range of states that can be ionized by the NIR wave. Therefore, the measured ion yield consists of a signal integrated over the contribution of different states up to a certain binding energy that equals the peak field strength of the NIR probe pulse. Considering this fact, the technique allows to distinguish the population dynamics for states with different binding energy by repeating the pump-probe measurement with different NIR intensities or by observing temporal separation of the depletion of states in the same delay scan. Since the shake-up states are exposed to the NIR-field from the moment of their creation until the end of the probe pulse, the ion yield constitutes a time integrated signal. The extend of this time interval is adjusted via the time delay Δt between the population of the states (arrival of the XUV excitation pulse) and the advent of the NIR light wave at the sample atoms.
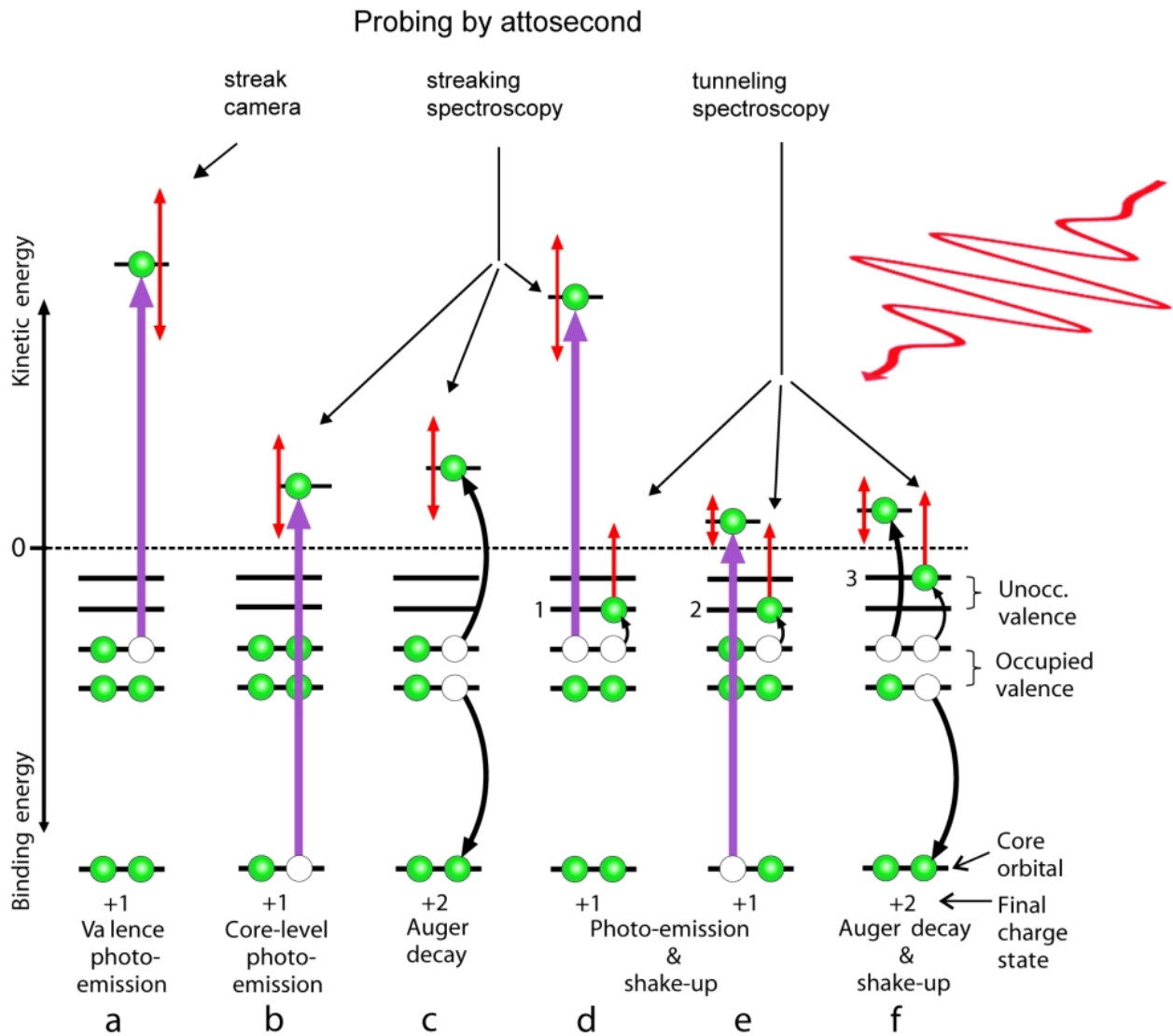
Fig. 4.2: By inducing valence (process a) or core photoelectron emission (process b), a XUV attosecond pulse triggers the inner-atomic motion. The temporal evolution of photo- and Auger electron emission (process c) can be probed via attosecond streaking (section 4.2) to retrieve the XUV pump pulse or the sampling NIR field. The XUV photoemission is usually connected to the population of previously unoccupied "shake-up"-states by another electron (case d, e). This process manifests itself in electron energy spectroscopy as electrons emitted at lower energies compared to the ones originating from valence photoemission. The curved black arrows represent the difference energy that is used to shake-up the electron remaining in the atom. For a sufficiently strong laser field, tunnel ionization can liberate the shake-up electrons. The temporal evolution of the tunneling current reflects the population dynamics of the shake up states on atto- and femtosecond timescales. In contrast to *attosecond streaking* (section 4.2), where the final charge state of the atom remains unchanged, for *attosecond tunneling spectroscopy*, the final charge state of the atoms under scrutiny is increased. As advertised in chapter 3, the observable in the later case is the number of ions in the different charge states, in the case of streaking it is the momentum distribution of the released electrons.

According to the scan sequence starting at *Δt<0* (NIR probe first) and proceeding towards *Δt>0* (XUV pump first), the yield of the engendered ions starts increasing at *Δt<0* evoked by

ionization at the trailing edge of the NIR pulses and continues increasing with growing Δt because the shake-up states are exposed to increasing NIR-probe intensities. For a system chosen not to undergo Auger decays, shake-up exclusively results from photoexcitation. The time-dependent ionization dynamics (Fig. 4.2 d) then can be examined by measuring the yield of doubly charged ions as a function of delay between the XUV pump and the NIR probe light field. The temporal gradients in the expected steps are the result of a convolution of the excitation duration (XUV pulse length), a possibly delayed response of the shake-up state formation and the tunneling dynamics. Suppositional an extremely short excitation, the measurement provides direct insight to temporal evolution of both the shake up process as well as light field induced tunneling.

Due to the absence of Auger decays for the experimental parameters dictated by the available attosecond pulse source with photon energy around 93 eV, neon turned out to be the model sample to prove the virtue of this concept. To estimate for which states the strong-field ionization in the tunneling regime can be observed over a few laser cycles, the needed NIR probe intensity is estimated in the following.

The main limitation that prevents observation of the tunneling ionization from certain states stems from the fact that once the laser intensity is significantly larger than the intensity needed to suppress the Coulomb barrier (I_s) the state will be depleted either before the field oscillation reaches its maximum value, or, for laser intensities too low, the depletion happens in only one half cycle so that no multiple step structure occurs. Combining the Keldysh parameter defined in section 4.1 in atomic units ($|e|=1$) with the expression for the electric field that suppresses the ionization potential defined as (Z: charge of the remaining ion)

$$E_0 = \frac{W_b^{\,2}}{4Z}$$

leads to the Keldysh parameter for the barrier-suppression intensity

$$\gamma_s = \frac{4\sqrt{2}\omega_L Z}{W_b^{\,3/2}}$$

Tunneling ionization prevails for $\gamma \leq 1$, rewriting this condition based on the above formula results in

$$W_b \geq 2^{5/3}(\omega_L Z)^{3/2}$$
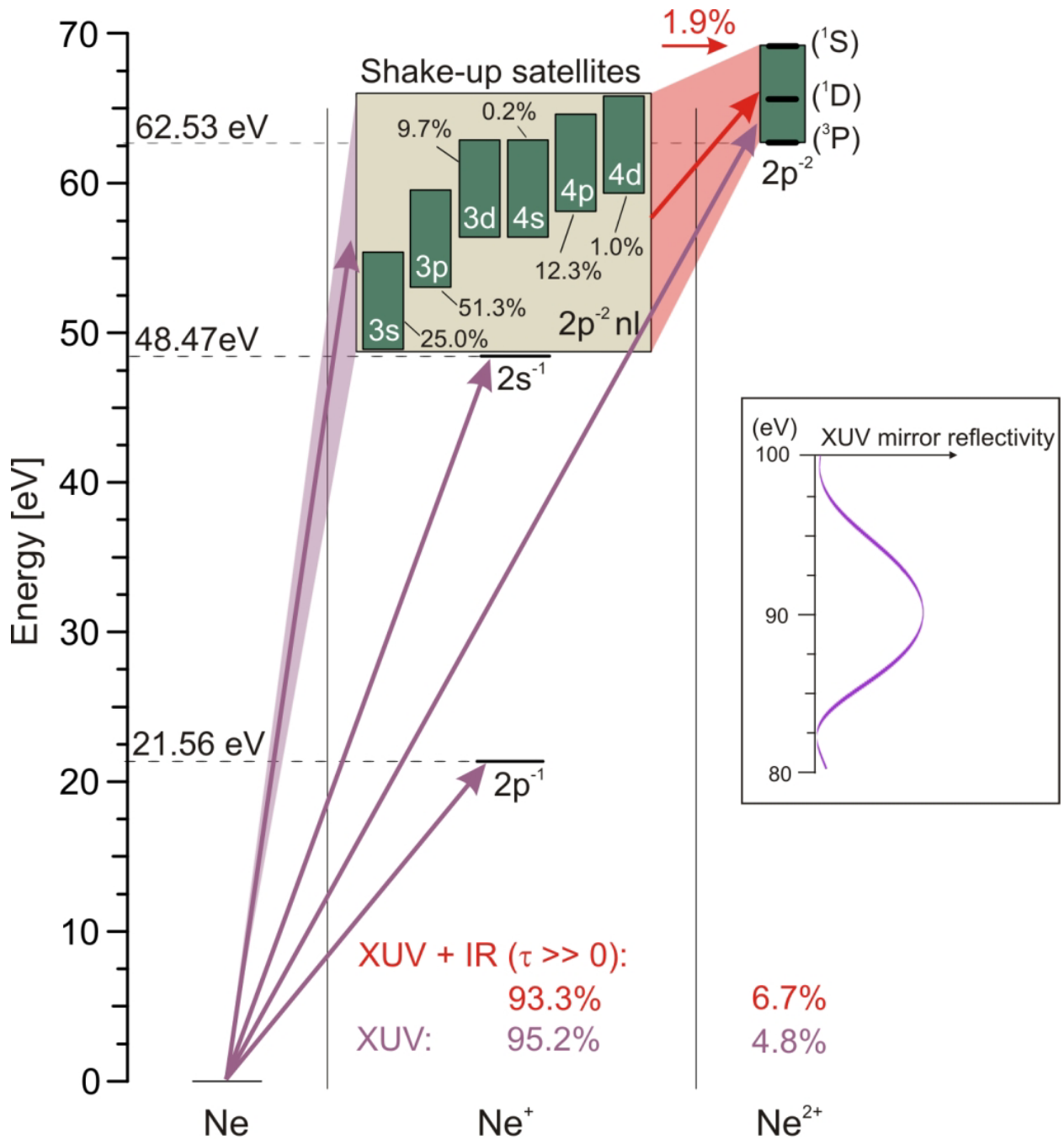
Fig. 4.3: Neon energy levels and transitions relevant to the measurement. The energies needed to single- and double-ionize are represented and the possible shake-up levels that are populated after the XUV pump excitation are also shown. The XUV photons in this experiment are centered at 91 eV (see inset: mirror reflectivity) and can produce singly or doubly charged ions, a small fraction of the singly charged ions is produced in *2p⁻² nl* configurations. The relative population ratios are known from electron spectroscopy. The few-cycle NIR probe pulse can ionize electrons from these states following the XUV pulse (*Δt>0*) and thus increase the probability for the creation of Ne²⁺. The absolute changes in the Ne²⁺/Ne⁺-ratio are given. 1,9% laser induced change in the Ne²⁺ yield imply, that a substantial fraction of the populated shake up states are ionized by the light field.

The binding potentials W_b of the individual shake-p-states according to [70] are smaller than the value achieved for $\lambda_L = 800\ nm$ and $Z=2$ (21.6 eV), the $\gamma \leq 1$ regime is not accessible for any of the states. Tunneling ionization, however, remains significant even for $\gamma > 1$, just the efficiency for multi photon ionization increases for higher γ-values.

Fig. 4.3 shows the neon energy level structure in the region of interest and the transitions relevant in the experiment. Neon atoms are ionized employing 250 as (~9 eV bandwidth) XUV pulses centered around 93 eV as probe (inset Fig. 4.3). The core shell is not accessed by the XUV photons. The threshold energies for single and double ionization are 21.56 eV and 62.53 eV, respectively. In good accordance with cross sections identified in synchrotron experiments, the count rate ratio between Ne^+ and Ne^{2+} ions created was (19.7±0.5) : 1 (Fig. 4.4). A few percent of the Ne^{1+} ions were promoted into $2p^{-2}nl$ (principal quantum number n: 3 or 4; quantum orbit l: s, p or d) configurations (Fig. 4.4).
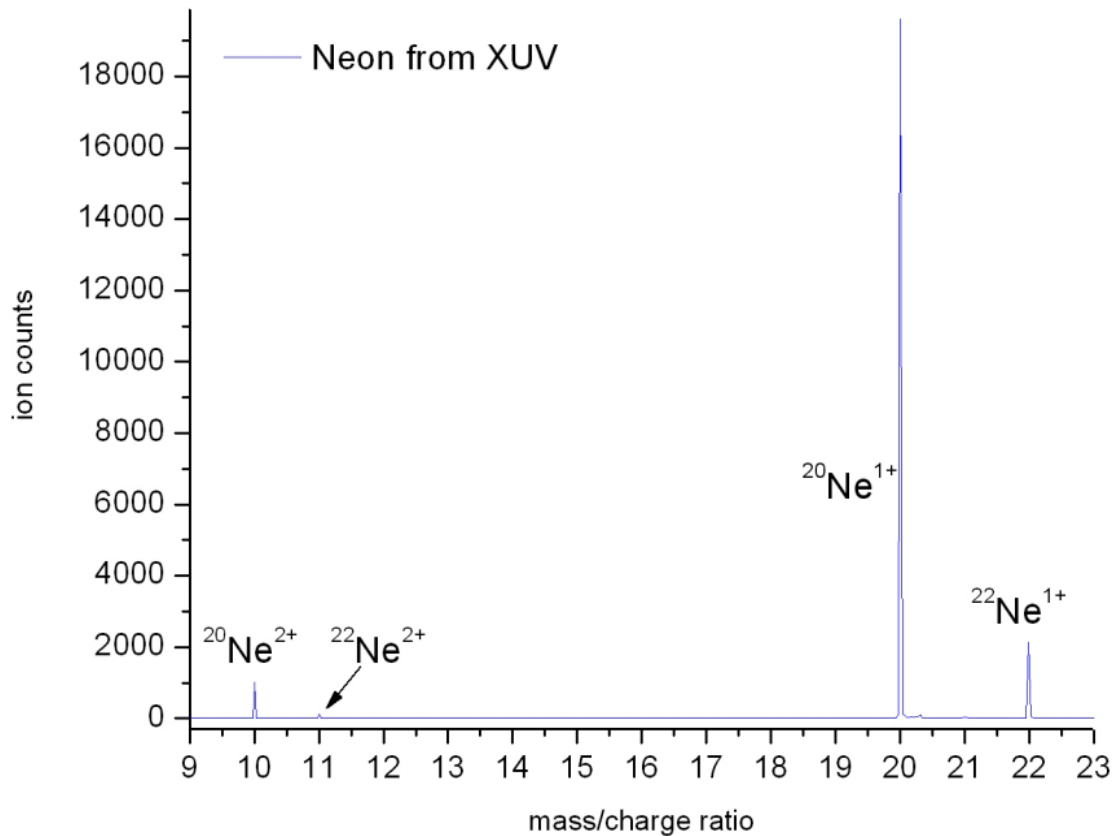
Fig. 4.4: Mass spectrum recorded after XUV pump excitation of neon. The relative countrate represents the absorption cross section for 91 eV photons and compares well with data available from synchrotron measurements. In the analysis of the measurements, the countrate of the two isotopes is always summed to increase the effective countrate. The observed effect is not expected to be isotope-sensitive.

This states decay radiatively on picosecond timescale. The NIR filed intensity was adjusted not to double-ionize Ne, the XUV- generated Ne^{2+} yield measured was therefore not affected by the NIR probe for $\Delta t << -\tau_L$ (τ_L: NIR pulse duration). For Δt approaching zero and becoming positive, the Ne^{2+} yield was significantly enhanced by the laser field. The NIR-induced Ne^{2+} yield enhancement amounted to $(40 \pm 4)\%$ of the XUV-produced Ne^{2+} yield at a NIR peak intensity of $(7 \pm 1) \times 10^{13}$ W cm^{-2}. The absence of this enhancement for $\Delta t << -\tau_L$ clearly indicates that the laser sets electrons free from the states excited by the XUV pulse. The laser-induced change in the Ne^{2+} yield amounts to some 2% of the XUV-produced Ne^{1+} ions. This implies that a substantial fraction of the population of the $2p^{-2}nl$ shake-up satellites must have been depleted by field ionization.

Fig. 4.5 a shows the number of Ne^{2+} ions detected as a function of delay Δt between the XUV pump and NIR probe. Fig. 4.5 b compares the prediction of the Yudin–Ivanov theory computed by V. Yakovlev (lines) with the experimental data (squares). In our modeling, the shake-up states were populated instantly during XUV photo-ionization (details on this in publication [70]). The calculations are in reasonable agreement with our measurements and reveal how the different shake-up states are depleted sequentially by laser-field ionization. The signal starts increasing at large negative delays owing to depletion of the $2p^{-2}4p$ state (relative population ~12%) and the $2p^{-2}3d$ state (~10%) at NIR intensity levels reached some 10 and 6 fs after the peak of the NIR probe ($\Delta t \sim -10$ and -6 fs), respectively. A more dramatic increase in the Ne^{2+} yield is observed as the delay approaches zero, as a consequence of the depletion of the most highly populated $2p^{-2}3p$ (~50%) and $2p^{-2}3s$ (~25%) states. In spite of their relatively high binding energy (~10 and 13 eV, respectively), these states are also depleted before zero delay. That is, by the field oscillation cycles comprised in the trailing edge of the pulse, leaving no room for increasing the Ne^{2+} yield with increasing Δt beyond 0. This main contribution to the Ne^{2+} yield emerges within approximately one and a half wave cycles of the NIR field, $\sim(3/2)T_L = 3\pi/\omega_L$, in several sharp steps that are spaced by $\sim T_L/2$; this clearly shows that field-induced tunnelling is the main cause of the observed increase in the Ne^{2+} yield. This conclusion is also supported by the disappearance of the steps in a pump–probe scan performed with a randomly varying carrier-envelope phase of the NIR probe pulses (grey line in Fig. 4.5 a).
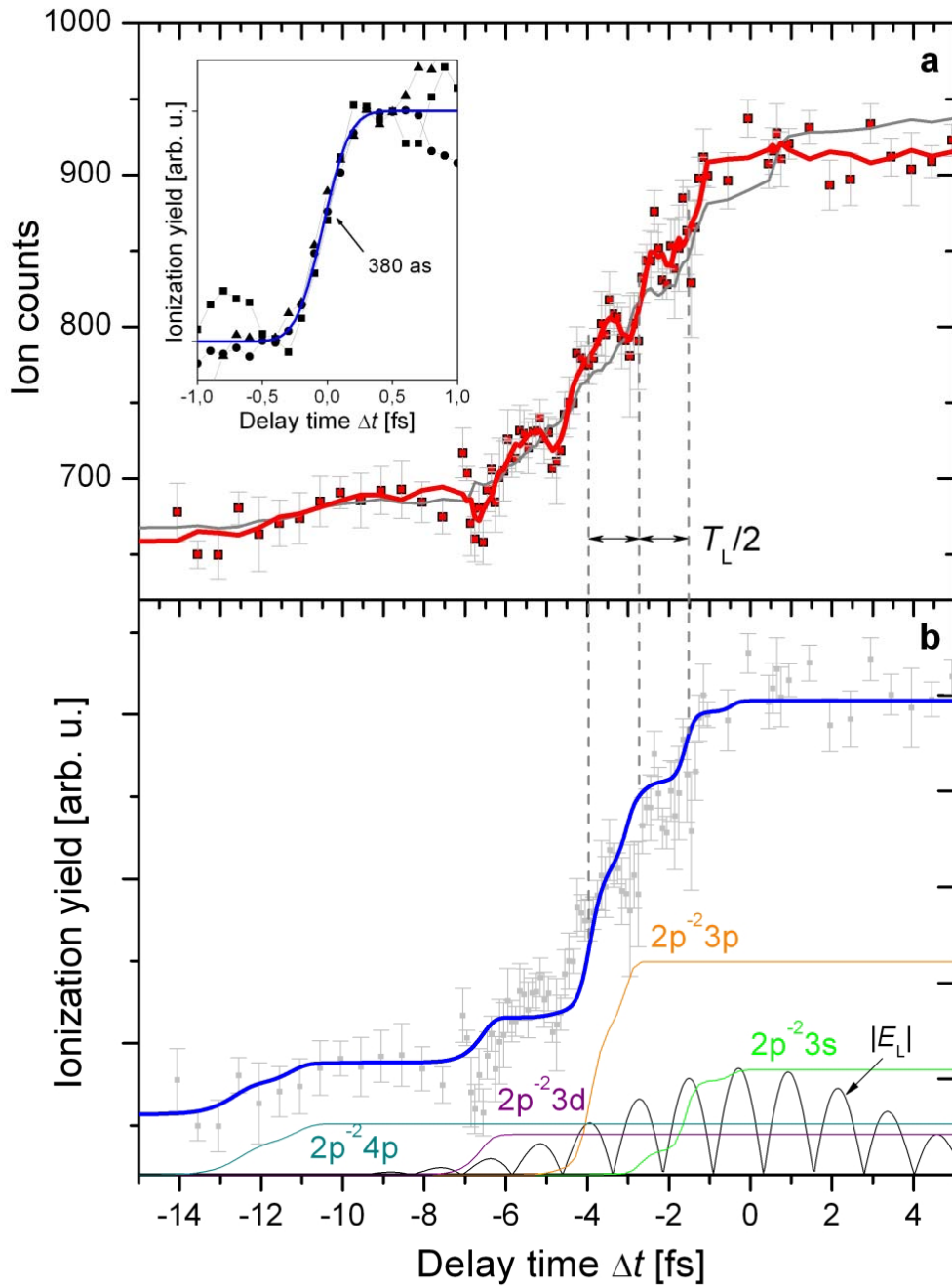
Fig. 4.5: The Ne^{2+}yield as a function of the delay between XUV pump and NIR probe pulse. Panel a) shows the experimentally obtained trace by repeating six scans under the same conditions. Every point is integrated 18 s (3 x 6) in total, squares and error bars represent the average and the standard error of the six measurements. The thick red line shows the 5-point adjacent averaging, the grey line the same but recorded for NIR probe pulses with randomly varying CE-phase. The inset shows the normalized ionization step of three independent measurements with an error-function fit yielding a rise time of 380 as. Panel b) shows the result of simulations based on the non-adiabatic theory of tunnel ionization for the states involved. The thick blue line is the sum over the fractional contributions of the individual states depicted by thin colored lines. The absolute value of the NIR probe field is represented as black solid curve.

4.2 Inner atomic timing – Attosecond streaking spectroscopy

The application of attosecond spectroscopy to the study of ionization of atoms bears the potential to investigate processes involving more than one electron. Time resolution approaching the atomic unit of time, as pointed out in the previous chapter, allows for the first time addressing intra-atomic electron energy transfer in real time. The ability to explore the time evolution of intra-atomic processes touches fundamental questions. Among a wide range of possible fields of interest are the following considerations:

• How do electron-electron interactions happen deep inside atoms?

• How do electrons extracted from an atom transfer part of their energy to electrons that remain bound to the core?

• How do electrons, remaining bound to the core, rearrange after the ionization?

Based on these questions, the following section shows how the techniques presented so far can be extended and used to explore dynamics of the electron-electron interplay in a nuclear binding potential.

4.2.1 Attosecond streaking spectroscopy of photoelectrons

In atoms and molecules, a superposition of the ion core potential and the potential formed by the individual electrons governs the motion. Even under unperturbed condition, without external fields and therefore with fixed total energy of the system the electrons move, interact and exchange places on the attosecond timescale. This multi-electron dynamics, the entanglement of all electrons with each other, is observable as a result of energetic collisions with electron or ions or by absorption of high-energetic (e.g. XUV) photons. Before an electron is detached from the core, it interacts with the electrons that remain in a bound state of the atom. The interaction of the electrons affects both the final momentum and the temporal evolution of the emission of the outgoing (ionized) electrons [73]. So far, only the later could be characterized experimentally and therefore provided access to the electron-electron interactions. In contrast to conventional collision physics where only final states of the scattered particles are subject to detection, attosecond spectroscopy opens access to intermediate states and their temporal evolution. First, the collision is precisely timed with the time-dependant field driving it [21, 74, 75]. The collision therefore can be timed relatively to a pump pulse and such act

as a probe [76] implying the possibility to exert optical coherent control to the system to be probed by collision. Secondly, the charged fragments decay in the presence of a synchronized time-dependant field. That means, that from the phase dependant momentum change the fragments undergo in the field, their time of birth can be reconstructed [77]. This application area of optical-field-driven streak camera to the photo ionization of neon is shown in Fig 4.7. As can be extracted from a high-resolution photo-electron spectrum recorded close to the photon energies utilized in this experiment (Fig. 4.6), neon emits two species of photoelectrons. After absorbing a XUV photon (~100 eV), electrons from two states ($2p$ and $2s$) can be liberated, appearing in the photoelectron spectrum as two narrow peaks.
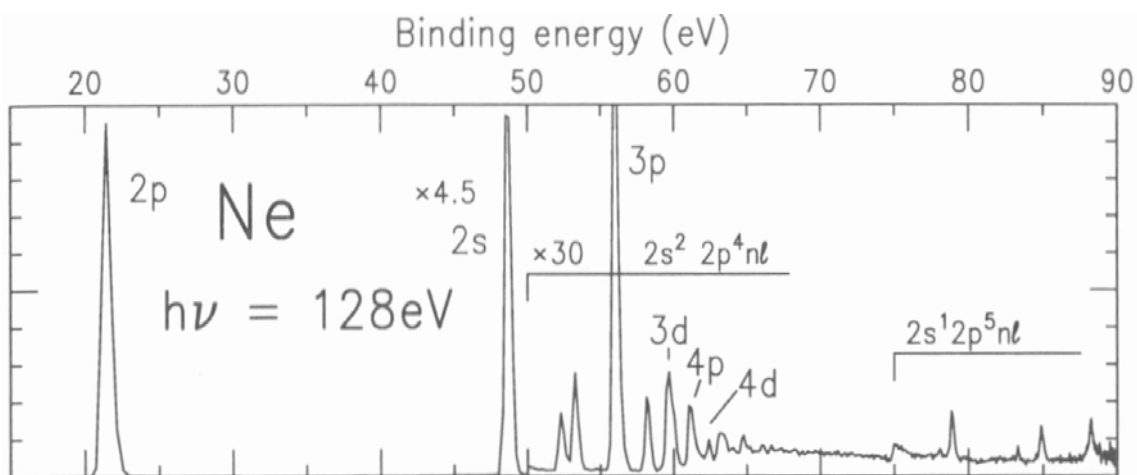

Fig. 4.6: High resolution photo-electron spectrum of neon excited at 128 eV [78]. The spectrum shows the $2p$ main line and the $2s$ line as main contributions to the spectrum. In contrast to the helium spectrum (Fig. 4.8), both the 2p and the 2s photo line are the result of a direct photo ionization and therefore not expected to have a difference in emission time.

After careful adjustment and by increasing the sensitivity of the electron time of flight spectrometer for the detection of low-energetic electrons, it was possible to record photo electron spectra showing two features in accordance with Fig. 4.6. For the measurements presented here, a Mo/Si-multilayer mirror was employed with central energy of 112 eV at a bandwidth of ~ 20 eV and a peak reflectivity of 7% (see purple curve in Fig. 4.9). This characteristics are a trade-off between high photon flux at lower energies (<100eV) on the one hand, and a clear separation of the second photo electron peak from the ATI background created by the laser pulses on the other hand. Applying a sufficient strong, time-delayed laser field in analogy to the streaking measurements presented so far, a streaking spectrogram as shown in Fig. 4.7 can be measured. With respect to spectroscopic measurement techniques, a narrower peak structure would be preferable; the highest temporal resolution, however, is only supported by a

large bandwidth. In the experiment, the bandwidth should be adjusted such that the two lines are clearly separable and the energetic overlap in the streaking spectrogram should be minimized. As shown in the Figure, both emission lines are "streaked" and their relative timing
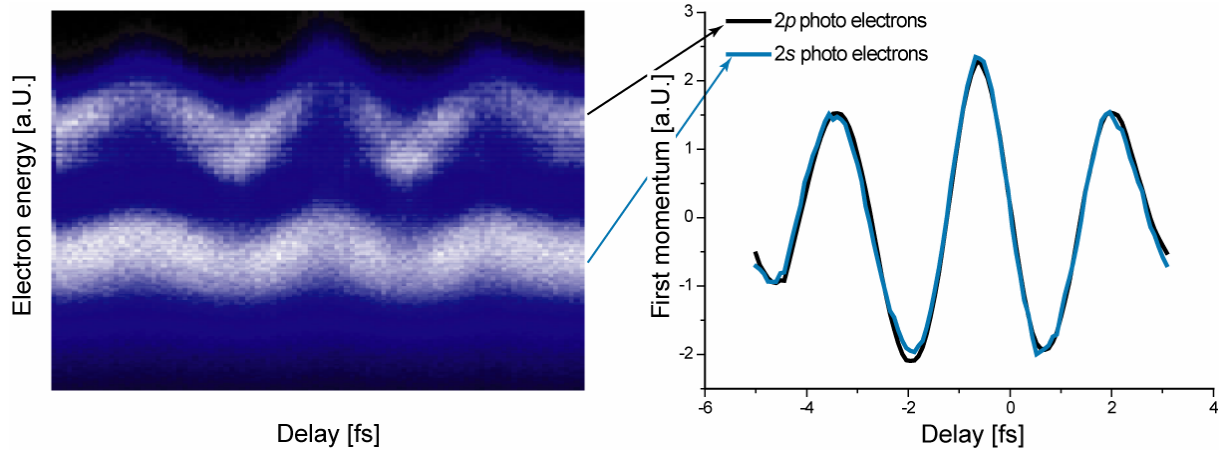

Fig. 4.7: Attosecond streaking spectroscopy (ASTS) in neon. The left panel shows the streaking spectrogram with the two emission lines. Due to the non-uniform sensitivity enhancement of the electric lens in the electron spectrometer, the relative countrate does not reflect the ratio of the partial cross-sections according to Fig. 4.6. The right panel shows the center of gravity retrieved from the two contributions to the spectrogram. In accordance with the expectation that the two independent direct photo emissions are synchronized, the trace in the left panel shows no temporal shift within the resolution of the measurement. The retrieved center of gravity is normalized and scaled to allow a direct comparison; the delay step size is 80 as. The small step size and the retrieved XUV-pulse duration of ~180 as according to an evaluation like presented in Section 3.5 set a strict upper limit for a possible timing difference of the two emissions.

with respect to the emission from the atom can be extracted from comparison of the two oscillating curves. Here, a simple first-momentum analysis is shown. Due to their different emission energy (cp. estimations in chapter 1.7), the electrons suffer a momentum change proportional to their initial momentum. The evaluated first momenta hence are scaled to have the same amplitude and normalized for easy comparison. Even with the small delay step size of 80 as (measurements with 20 as confirmed the result), no delay is apparent as expected for two independent direct photo-electron emissions. The upper limit for a yet possible delay is a convolution of the XUV pulse duration (~180 as) and the step size employed to record the spectrogram.

4.4.2 Attosecond streaking spectroscopy of shake-up states

XUV photons interacting with atoms can, in addition to the valence-band photoelectrons, also liberate electrons from inner shells of atoms. Typically, inner shell vacancies decay rapidly through an assortment of processes including electron-electron interactions. These interactions may eject secondary (Auger) electrons and/or promote others to excited bound states through a process referred to as shake-up. These quasi-stable excited atomic states are present in a manifold of atom-field and atom-atom interactions. Hence, insight to the time-evolution of the population of those states is an objective of time resolved studies since the first short-pulse laser sources are available. So far, attosecond technology allowed probing Auger electrons directly in the time domain as described in Section 4.1 (attosecond tunneling spectroscopy) or [9]. The study of the time evolution of shake-up states, in principle, follows the same route. The dynamics are triggered by an attosecond XUV excitation and measured by the strong, synchronized field of the laser pulse previously used for the generation of the attosecond pulse.
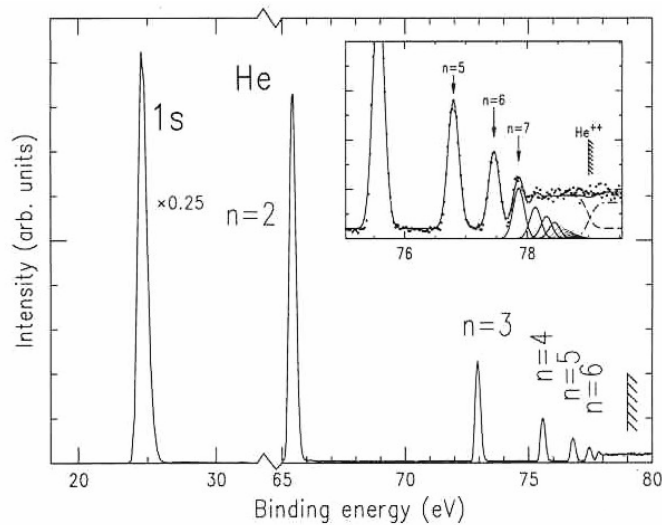
Fig. 4.8: High resolution photoelectron spectrum of helium excited at 89.5 eV [78]. The spectrum shows the 1s main line after photoexcitation along with a series of satellite lines (n=1-7). The relative peak-heights roughly reflect the partial cross-section for the different processes. An important feature of the spectrum making helium an ideal target for streaking spectroscopy is the large energy separation (~40 eV) of the direct- and the first shake-up-line and the negligible contribution of higher satellites at the relevant photon energies.

Theoretically, the investigation of shake-up effects is of great interest. Shake-up effects accompanying transitions in the electron shells are widespread and are, in fact, manifestations of the reaction of a many-electron system to a sudden change in the state of a part of the system. The mathematical treatment of shake-up processes requires the description of three-particle-

problems that usually withstand analytical studies. Much theoretical effort was spent on reducing shake-up processes to generalized formalisms that allow estimating the transition probabilities [79] in the frame of a formalism that is a extension of perturbation theory. This approach necessarily neglects the time evolution of the process and solely predicts the transition probabilities.

Recent work, based on non-perturbative time-dependant calculations that are based on the direct propagation of the time-dependant Schrödinger equation, for the first time is capable of addressing the question of timing [80].

4.4.3 Streaking Spectroscopy in Helium

In photo-electron spectra strong "main-line" peaks (as the two observed photo lines in Neon in the previous section) are accompanied by weak satellite peaks (Fig. 4.8). The satellite transitions lead to final ionic states that cannot be created simply by removing a single electron from the nominal ground-state configuration [81]

$$He(1s^2(^1S)) \rightarrow He^+(2s,2p) + e^-$$
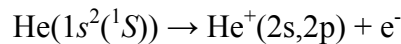
instead of the configuration for the direct photo emission

$$He(1s^2(^1S)) \rightarrow He^+(1s) + e^-.$$
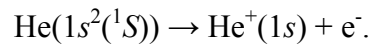
According to the shake-up theory [82] the more or less abrupt change in the atomic potential that accompanies the photoelectron's departure provides a perturbation which may shake one of the passive electrons into an excited orbital. In this phenomenological picture, the probability of reaching an excited (satellite) final state in the ion depends on the time for the hole to be created and hence on the kinetic energy of the photoelectron. In the framework of this description, two limits are assumed. At the satellite threshold, in the adiabatic limit, the orbitals of the passive electrons can relax into their final-state form during photoemission, accelerating the photoelectron. In this limit, the satellite transition probability has its minimal value. For high photon energies, sudden limit, the satellite transition's intensity approaches a constant fraction of the main-line intensity. This scenario is represented in Fig. 4.8 where the *n=2* satellite electrons leave the atom with a remaining excess energy of ~25 eV, safely within the sudden limit.
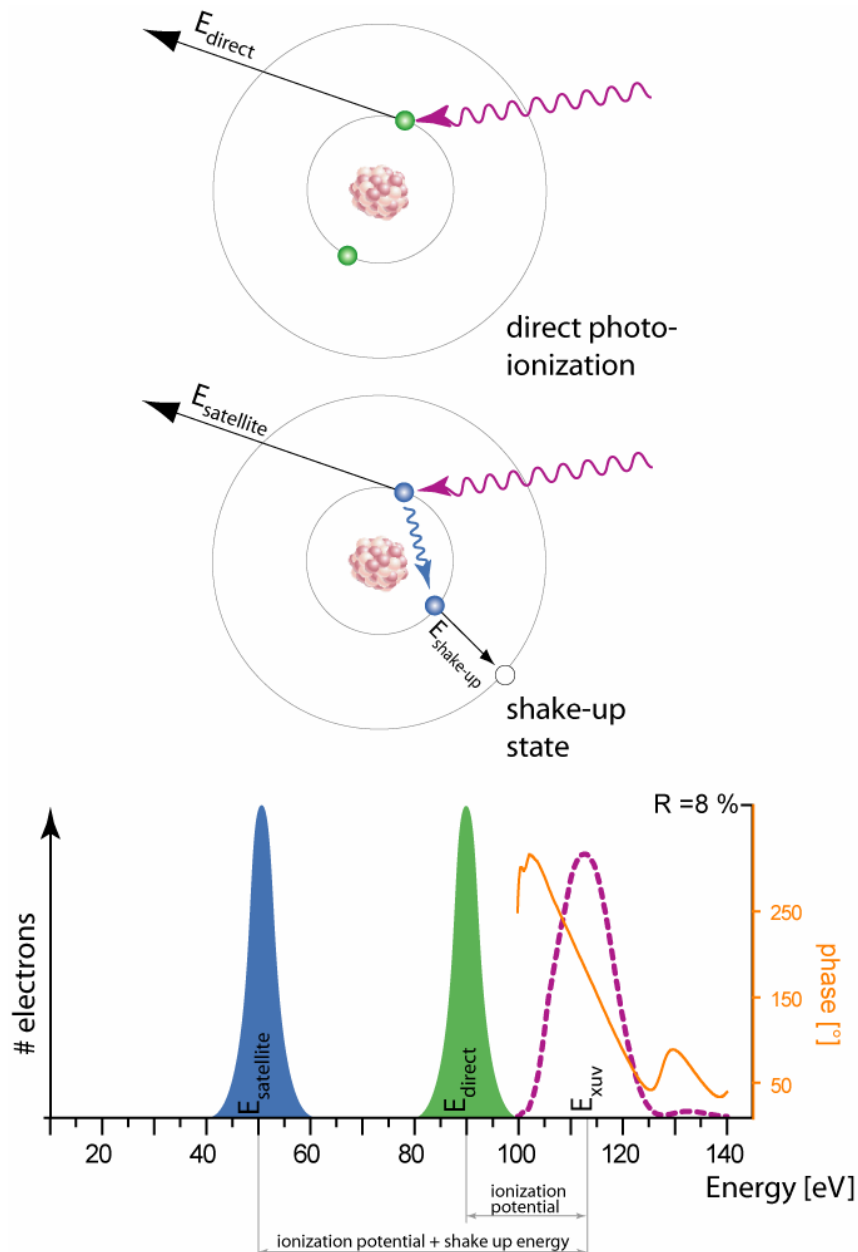
Fig. 4.9: Attosecond STreaking Spectroscopy (ASTS). Photo ionization at XUV photon energies in helium can take two different pathways. Besides the direct photo ionization (upper panel) that releases an electron with the energy of the incoming light pulse lowered by the ionization potential, the photoelectron spectrum reveals the presence of a second effect. After absorbing a XUV photon, the electron leaving the atom can share a part of its energy with the second electron (panel in the middle) remaining in the atom. The excitation of the second electron (referred to as shake-up satellite) determines that the electron that leaves the atom carries less kinetic energy than the direct photo electron. The schematic photo-electron spectrum shows the experimental situation. The bandwidth of the XUV pulse (mirror reflectivity: purple dotted line / mirror phase response: orange line) is reflected by the bandwidth of the photoelectron line corresponding to the direct emission. At even lower energies a second line appears formed by the electrons that undergo the shake-up interaction.

91

In the case of Helium at photon energies around 100 eV, the cross section for the direct and the *n=2* satellite line are 5 x 10^{-1} Mb and 5 x 10^{-2} Mb, respectively. High resolution measurements [83] allow to deconvolve the n=2 line into the contribution of the 2*s* and 2*p* configuration. For the photon energies employed in the experiment, the 2*s* is governing the satellite/main-line intensity ratio while the 2*p* branching ratio almost vanishes for energies above 80 eV. Fig. 4.9 shows the situation for Helium.
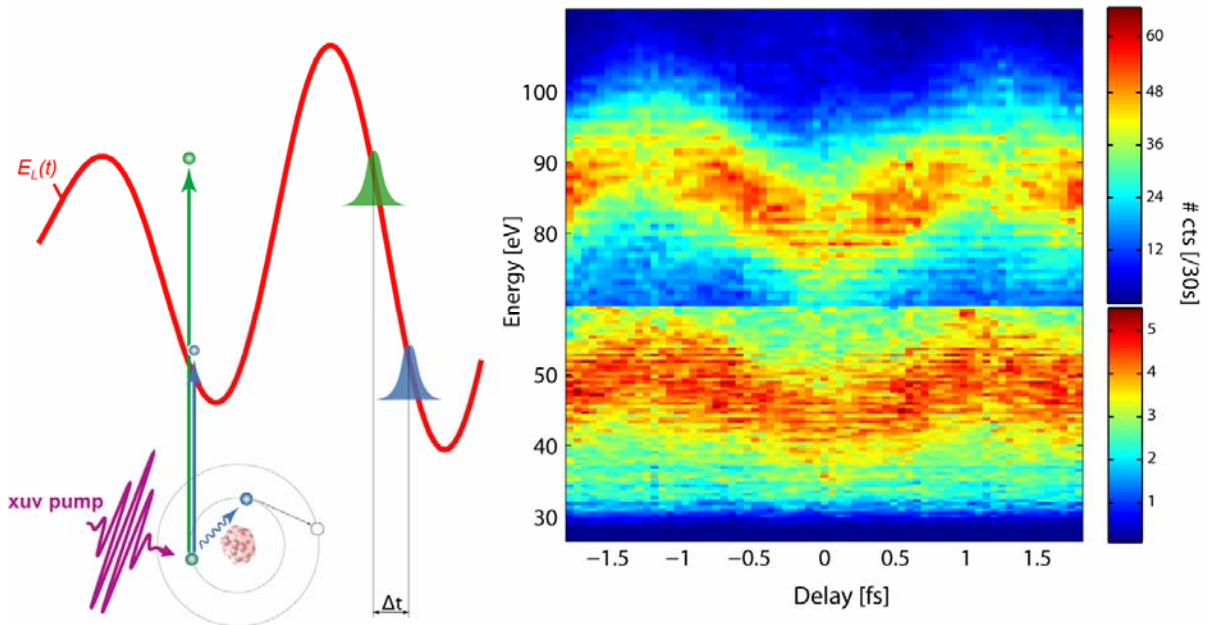
Fig. 4.10: ASTS in helium. The right panel shows the streaking spectrogram with the two emission lines with independent color coding for better visibility. The left panel symbolizes how a possible delay between the emission times of the two electron species would be observable in the streaking spectroscopy. A time delay in the electron emission would lead to a temporal offset of the two streaking curves recorded in the same measurement.

Experimentally, a manifold of requirements is imposed on the atomic system to study. First of all, the available detection scheme should allow the separate observation of direct photoelectrons and those that sustain a loss of energy due to the shake-up interaction. The electron spectrum therefore has to be clean from resonance lines in the energy range of interest and the shake-up emission line should have a cross section that is at least comparable to the cross section of the direct photoelectron ejection. Furthermore, to make use of the unprecedented temporal resolution that attosecond spectroscopy can offer, the excitation necessarily comprises a substantial bandwidth. Thus, the energetic spacing between the direct photo line and the shake-up line has to be larger than (two times half) the bandwidth of the exciting XUV pulse. The electrons ejected subsequently to the ionization by the XUV radiation are liberated in the presence of the laser field and accumulate a change in their final momentum just as in the

conventional streaking spectrograms. To distinguish clearly between the two contributions in the recorded electron time-of-flight spectrograms, an even larger distance between the two lines is desired. Another important aspect that has to be considered when performing an experiment is the creation of above-threshold-electrons (Section 1.3) through ionization taking place in the laser field. Since they appear in the electron spectrum at low energies, they possibly overlap with the shake-up line in the spectrum, making the analysis of the data more difficult. This is the reason why target materials with highest possible ionization potential are preferred. The second strategy to avoid ATI background within the region of interest in the electron spectra is to shift the excitation to highest possible photon energies. The second line in the presented experiment appears centered at ~ 45 eV, safely above the background electrons. Besides low energetic electrons are susceptible to magnetic and electric influences and thus harder to detect accurately, this large separation between signal and background leaves enough range to apply a strong laser field to streak the emission lines substantially and exploit the temporal resolution of the technique. This is in perfect accordance to the procedure presented in chapter 3.5, where only the strong streaking field allowed the application of the FROG retrieval with adequate certainty and resolving power.

In this respects, helium is the perfect atomic system to demonstrate the power of streaking spectroscopy. Of course, the best possible compliance with all the requirements pointed out above is not coming free of expense; the count rates for helium are more than a factor of ten lower compared to measurements performed in neon.

Fig. 4.10 clarifies the idea of *At*tosecond *ST*reaking *S*pectroscopy (*ASTS*) in Helium. If the emission of the two electron species is not an instantaneous response to the XUV excitation, the ejection of the electrons happens at different instances of the laser electric field. The change in the final momentum of the electrons, depending on their birth-time in the laser field, therefore encodes the relative timing of the two emissions. A streaking spectrogram recorded under these premises allows accordingly the observation of a time delay as a relative shift of the two streaked electron lines in the spectra. In Fig. 4.10, the right panel shows such a spectrogram (delay step size: 60 as) with the two emission lines energy calibrated and scaled
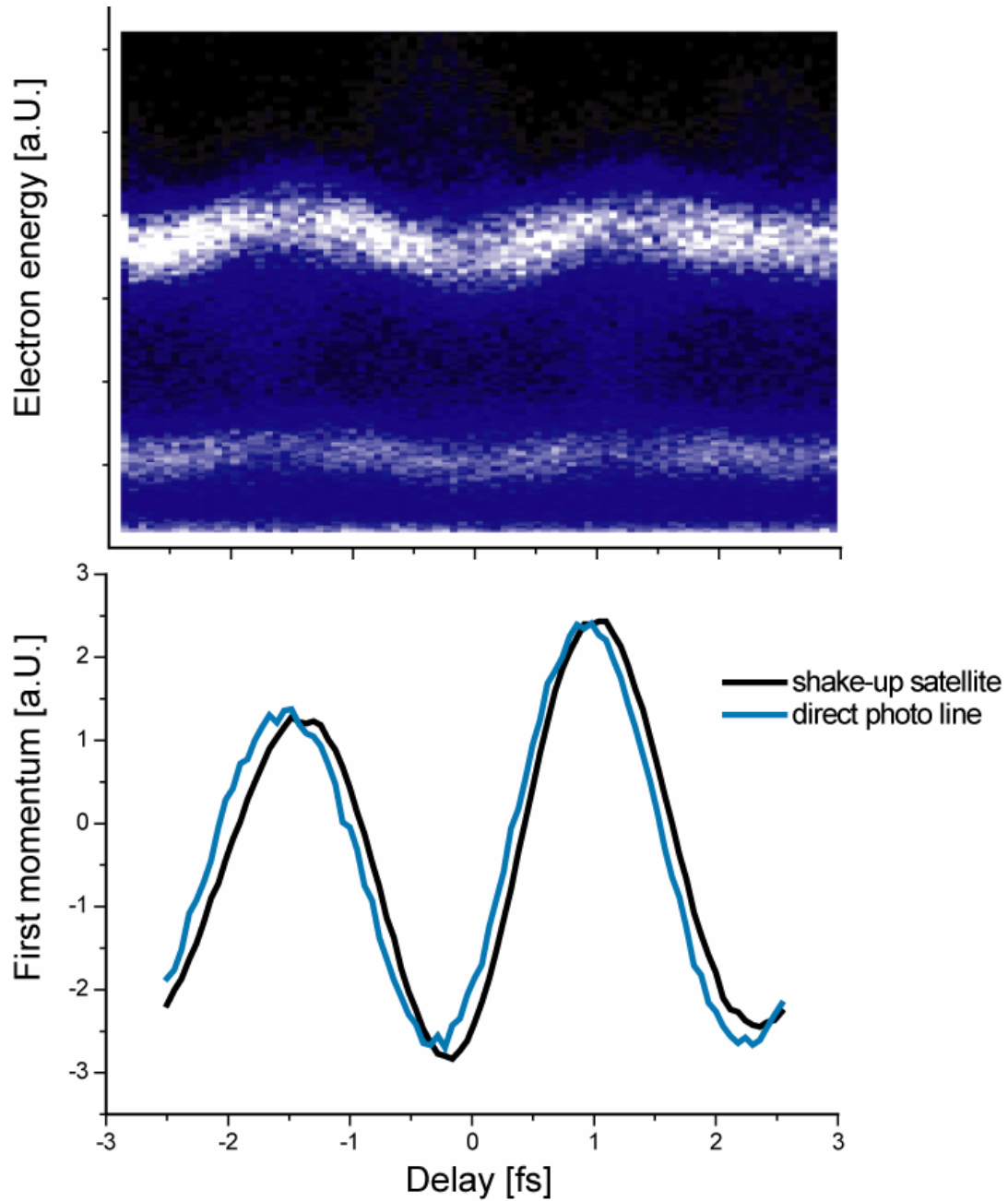
Fig. 4.11: ASTS in Helium. The upper panel shows the streaking spectrogram observed in Helium with the two lines corresponding to the 1*s*- and the *n=2*-satellite emission in Fig. 4.8. The electron time-of-flight spectrometer uses an electrostatic lens to enhance the detection efficiency within a certain energy band. The setting for the presented measurement is such that preferentially the shake-up satellite electrons are detected. The count-rate ratio therefore is not appropriate to the partial cross sections. The lower panel shows the resulting center of gravity evaluated from the above data. The offset between the two curves in this preliminary data suggests a possible delay between the two emissions on the order of ~100 as. It should be noted that the sign (as well as the amount) of the delay can not be directly extracted from the above curve and is object to a more detailed analysis.

independently for comparability. It is obvious, that a small possible shift on the order of less than ~ 500 as is not immediately visible to the naked eye. Fig. 4.11 shows a first-momentum analysis like for neon in the previous chapter, suggesting a delay between the two emissions of ~ 100 as. This trend is confirmed by a variety of scans taken in helium at different streaking fields, however, a detailed analysis of the recorded data has to prove (or disprove) the result.

The preliminary analysis of the data in terms of first momentum retrieval incorporates several uncertainties that prevent the conclusions from being reliable and undoubtedly. A much more reliable analysis based on the FROG algorithm is presented in chapter 3.5.2. The algorithm can treat the double emission as triggered by a XUV pulse possessing two peaks in the time domain with a certain time delay (corresponding to the time delay between the two emission lines in the photo-electron spectrum) and two peaks in the spectral domain as well (corresponding to the energy difference of the two lines). First test have proven the ability of the algorithm to deal with such a composite spectrogram. The retrieved pulse has a double-hump structure; each hump has a different carrier frequency (observable as difference of the slopes of the phases under each hump). As directly evidenced by the delay in the streaking patterns for both peaks, it seems that the algorithm has the ability to deal with the delay given to the low-energy photo ionization peak. Further work has to be carried out in this direction before reaching a final conclusion.

Experimentally, a planned improvement is the introduction of a very thin waveplate in the laser beam after the generation of the XUV light to polarize the laser pulse slightly elliptical. The breaking of the symmetry leads to a dramatically reduced probability for above-threshold ionization while barely affecting the streaking effect. This idea, allowing for much higher streaking fields, will further improve the resolution of the technique.

4.5 Intensity selective ionization studies

The present knowledge about ionization occurring in high-intense laser foci is based on measurements that spatially average the ion-yields. Based on those data, that are the result of a convoluted action of many intensities affecting the atoms under scrutiny in a rather complex focal geometry, it is therefore hard to accurately describe saturation effects. Exceeding a certain intensity, low charged ionic states are expected to be depleted in favor of the formation of higher charged particles. The experimental techniques presented so far are incapable to observe such a behavior since the signature of such a depletion is buried under the signal arising from the extended generation volume. The following section introduces a new technique to study spatial distributions of ions in the focus of a laser beam of ultrashort, intense pulses in all three dimensions.

4.5.1 Laser ionization and charge state distribution above the saturation level

An unavoidable property of studies performed in focused laser light is the presence of a broad range of peak intensities across the focal region. Experimentally, this results in the acquisition of a volume-integrated product yield $S(I_0)$

$$S(I_0) \sim \int_0^{I_0} P(I) \left| \frac{dV(I,I_0)}{dI} \right| dI$$

I : peak intensity

$P(I)$: propability to ionize at intensity I

$V(I,I_0)$: Volume where $I > I_0$

The probability $P(I)$ that should be investigated is therefore different from the measured yield $S(I_0)$ due to the volumetric weighting. Even though the focal geometry might be described analytically, the unambiguous deconvolution of the measured yield according to the above formula is prevented by the lack of precise knowledge about the ionization process. Since for intensities above the assumed saturation intensity (for which $P(I) \rightarrow 1$), the measured yield becomes proportional to $I^{3/2}$, the decrease of $P(I)$ for higher intensities is camouflaged in the acquired signal. This behavior is widely studied in experiments dealing with the generation of highly charged ions in intense laser foci [84, 85] and several efforts where attempted to confine the detection volume at least along on dimension like intensity selective detection (ISS) [86, 87]. The direct measurement of $P(I)$ requires the confinement of the detection region to a volume explicitly smaller then the extension of the laser focus.
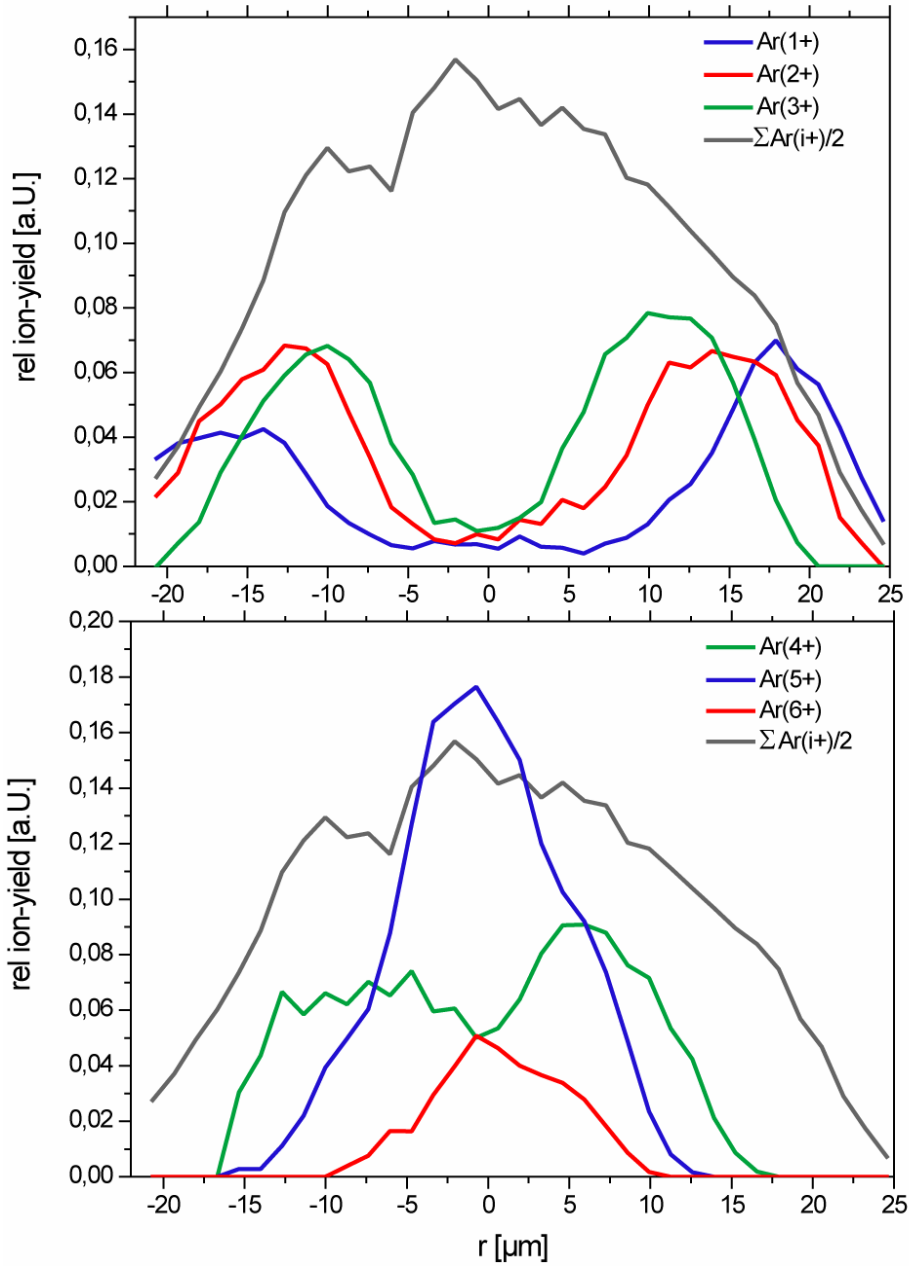
Fig. 4.12: Intensity selective detection of ions in a focused laser beam. The upper panel shows the occurrence of Ar^+, Ar^{++} and Ar^{3+} across the focus of 1,8 µJ, 48 fs laser beam along with the sum over all generated ions. It is clearly visible, how the higher charged states are generated in a more and more narrow area around the beam-axis. The lower panel shows the higher charged states (Ar^{4+} - Ar^{6+}) again along with the sum over all ions. Up to Ar^{4+}, the observed ion yield drops around the beam center, i.e. for high intensities. This clearly indicates saturation of the process and constitutes a direct measurement of intensity dependant ionization probability. The survival of lower charge states in the beam center where Ar^{6+} is generated is a challenging observation. The occurrence of lower charge states in the focus can not be attributed to beam inhomogeneities and pointing instabilities as witnessed by in-depth studies of the laser focus and the beam-pointing-stability with optical methods.

The measurements presented here rely on the reflectron mass spectrometer presented in chapter 3.3.2 and make use of its capability to trace back the origin of ions along the spectrometer axis as encoded in their arrival time on the detector. To confine the detection volume in the two dimensions transverse to the laser beam, the spectrometer was equipped with a 10 μm wide entrance aperture. In total, the detection region was constricted to a cylindrical volume of 10 μm diameter and < 5 μm height. A comparison of the measured traces with a simple model yielded a half-width of the focused beam of 14 μm, detailed optical measurements of the laser focus have not yet resulted in a conclusive number. It should be noted, that the saturation of the lower charge states sets in already at distances distinctively larger than the given half-width.
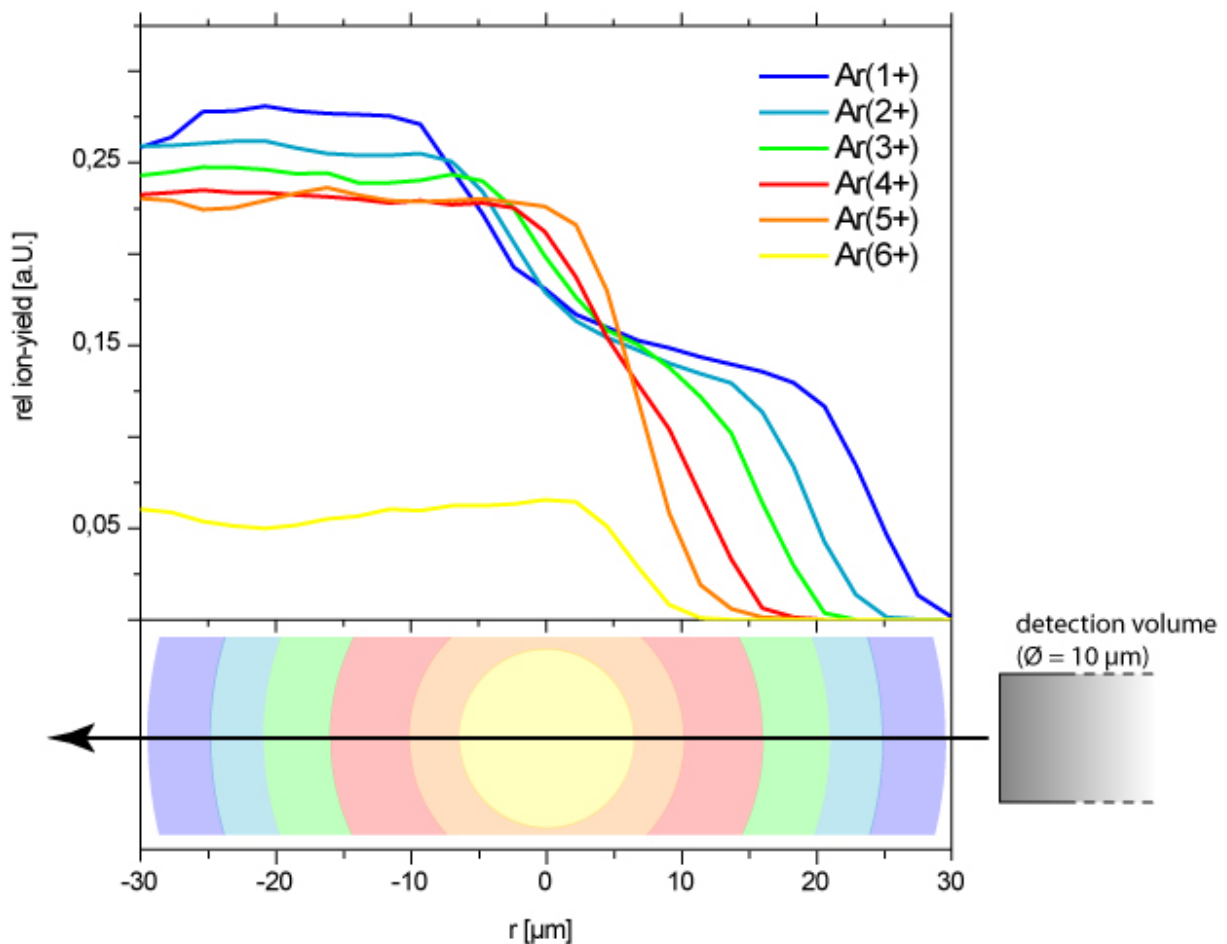

Fig. 4.13: Ion-knife-edge. The upper panel shows data acquired by scanning the position of the detection volume across the beam. The charged states set in according to the extent of their respective generation volume that is large for low-charged states. The kink in the traces of Ar^+ - Ar^{3+} is indicative for the depletion of these states in the center of the focus.

In addition, the focus appears in the optical imaging not to be a perfect Gauss-mode; a complex intensity rise in the slopes of the laser focus on the other hand dramatically influences the occurrence of the different charged states. In contrary, the measured yields give a handsome tool to observe the extent of the focus and its structure with μm resolution. This fact suggests the application of the described technique to analyze focal intensity distributions. The measurements confirm the known rise of the signal with increasing intensity, but furthermore allow investigating the observed drop of the signal if the intensity becomes larger then the saturation intensity.

Across the confined, μm-sized detection volume, the variation of the local peak intensity is tolerable enabling direct measurements of $P(I)$ for the first time. In Fig. 4.12, the detected yields across the laser focus is shown for Argon ions generated by a focused laser beam with 1,8 μJ pulse energy at a duration of 48 fs. The repetition rate is 1 kHz. The focusing is achieved by a achromatic lens with f=15 cm. The measurement was performed at a pressure of 3 x 10^{-7} mbar and with a peak intensity on-axis of 5 x 10^{15} W/cm². The detection volume is moved by scanning the voltage settings of the ion-reflector in the spectrometer and thus scanning the generation volume across the laser beam. From the voltages applied to the R-TOF spectrometer (cp. Fig. 3. 12) the ion-flight-time dispersion-relation can be extracted and thus the actual displacement of the detection volume. The axis in both Fig. 4.12 and 4.13 are given in μm and highlight the spatial resolution the technique offers, exceeding by far any method to investigate intensity distributions in the focus that is based on optical imaging. In addition, the method is applicable to the full beam without any need for attenuation as optical methods in general are.

Fig. 4.13 shows the result of a connatural idea: The detection volume in this case is an elongated cylinder perpendicular to the laser beam. This idea, similar to knife-edge methods that are employed in optics, is put into practice by stepwise moving the on one side sharply bordered detection region (i.e. the energy filter acceptance range of the R-TOF) in the laser focus. The charge states appear subsequently as the beam-axis is approached according to the concentric alignment of their generation volumes. The lower panel of the figure shows how the structure of the generation volumes can be imagined. By approaching the laser focus from the side, first Ar^+ ions are detected since their formation requires the least intensity. By further moving the detection range to the beam axis, the cloud in which the intensity is high enough to generate doubly ionized Argon is adding contributions to the signal.

As a consequence of the small confinement of the area from which ions are collected, the measurements presented here, in principle, are in the position to clarify quantitatively how the depletion of low charged states in the most intense part of the laser focus takes place. To this end, space charge effects have to be efficiently excluded, what, according to the latest findings, is only ensured for pressures below $\sim 5 \times 10^{-7}$ mbar [88]. The data presented in Fig. 4.14 are taken at a pressure of 1×10^{-6} mbar and show a charge state distribution that becomes broader as the overall charge is increasing (at high intensities many charge states are present). However, the charge-state distribution is necessarily very susceptible to space charge effects.
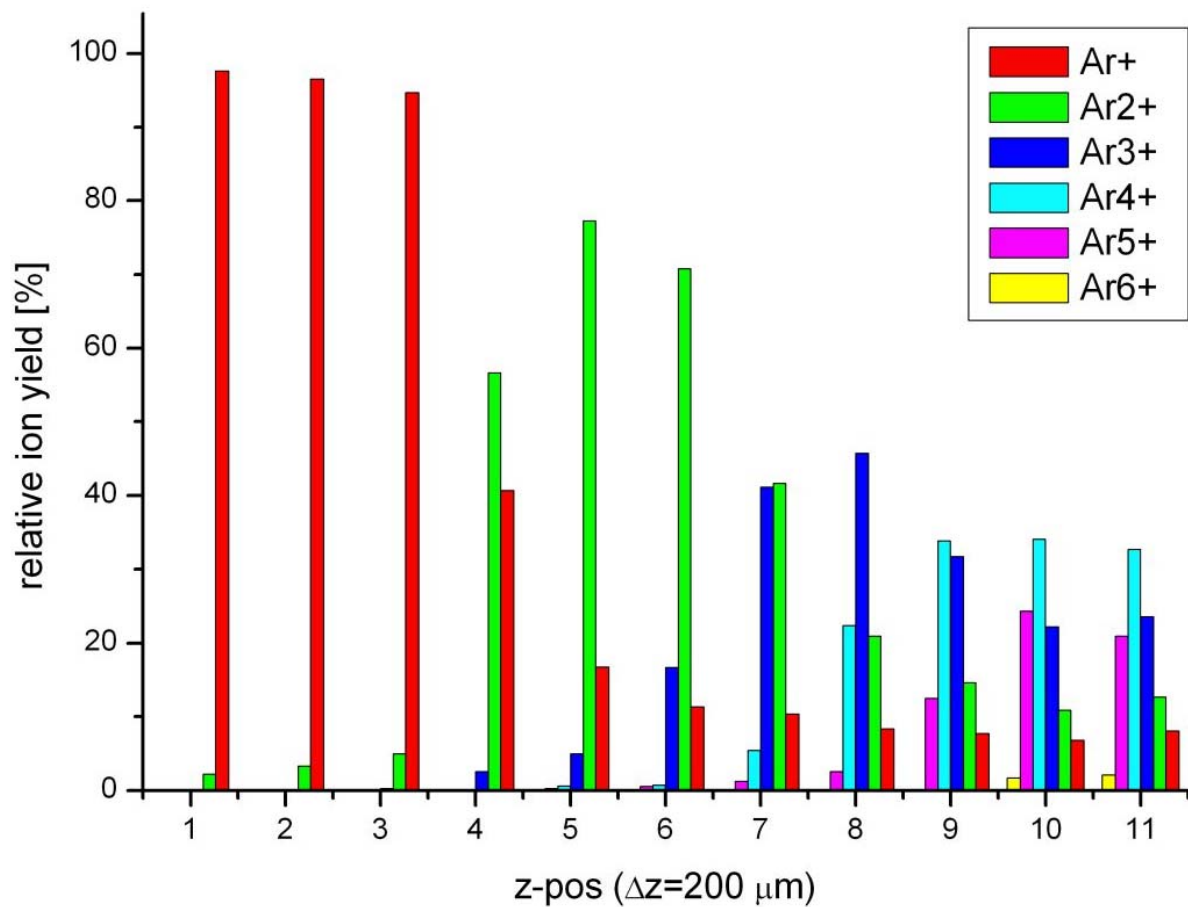
Fig. 4.14: Charge state distributions inside the laser focus. By shifting the detection volume (here 60 x 20 x 10 μm) along the beam axis through the focus, effectively the constant intensity inside this volume is changed. The different z-positions correspond to different intensities, position 11 relates to the highest intensity (i.e. the geometrical focus). Obviously, even for the highest intensities, lower charged states survive suggesting the presence of re-neutralization processes (e.g. High-harmonic-generation, recollision, plasma effects).

In the future, detailed studies on this have to be performed with a low pressure ensuring the absence of space-charge effects. So far, measurements at very low pressures have already proven that a complete depletion of ions in a specific area is detectable based on the presented technique. For Oxygen, a diatomic molecule that breaks apart before being ionized, no recollision channels like for Argon atoms are possible (i.e. re-neutralization is prohibited). The first measurements focused on this idea showed an entirely vanishing O^+ signal in a volume that roughly corresponds to the generation volume of Ar^{5+} and Ar^{6+}.

Conclusion

This work presents the experimental realization of different methods to study processes in atoms and molecules with attosecond resolution. Based on the principles of pump-probe measurements previously demonstrated, a new apparatus was developed aiming on the improvement of several bottlenecks that were identified in the precursor setup. Improved UHV-conditions, better vibration damping and several advancements towards higher XUV photon flux enabled the extension of attosecond time-resolved studies towards more complex systems on the one hand and the acquisition of more reliable data on the other hand.

The implementation of new techniques to upgrade the laser system led to a significant shortening of the pulses available in the experiment and subsequently provided the opportunity to boost the temporal resolution by a factor of 3. It was possible to present an improved scheme for the carrier-envelope phase stabilization, an absolute exigency for attosecond time resolved studies that helped to increase the long- and short-term stability significantly and enabled in-depth-studies of influences of incremental changes in the CE-phase on the formation of attosecond pulses.

Summarized under the headword "*attosecond tunneling spectroscopy*", the experiment presented in chapter 4.1 provided insights to the temporal evolution of light-induced electron tunneling (upper limit for the time it takes an electron to tunnel < 400 as) and the population dynamics of short lived transient states. This processes, so far only studied in spectroscopic measurements, for the first time revealed their complex temporal behavior.

Detailed investigations of the harmonic radiation generated by atom-light interaction with laser pulses approaching the single-cycle limit and analyzing the influences of the carrier-envelope phase setting to the emitted spectrum enabled the isolation of single attosecond XUV pulses with a duration down to ~80 *as* [89] in an energy range that allows to address many interesting questions concerning electronic time evolution inside atoms and molecules.

First experiments based on a technique dubbed "*attosecond streaking spectroscopy*" inquired a possible timing in a very basic property of matter: the release of electrons from the atomic core that before leaving the atom potential interact with the remaining bound electrons. Almost no intra-atomic process rearranging the electronic configuration is thinkable without those shake-up transitions; the presented measurement addresses the temporal characteristics for the first time.

Outlook

The following lines summarize the perspectives of the presented experiments in the foreseeable time ahead and point out the major, more future-oriented goals that the developed experimental techniques shall allow to tackle. In order to avoid reiterating the reflections given in the introductory paragraphs of the experiment-chapter, the overview is given in form of a list.

• Tunneling spectroscopy

Experimental evidence gained in the presented work suggests an upper limit for the tunneling time. An immediate consequence is that revisiting the tunneling spectroscopy experiment with the in the meanwhile threefold improved temporal resolution will either set a new (i.e. lower) upper limit for the tunneling time, or hopefully (and, at the same time more physical) enable one to investigate this timing; i.e. to observe electrons tunneling through a barrier. Besides the vast implementations that the demonstration of such a capability would have in all sorts of time-resolved experiments on the atomic scale, this question touches fundamental quantum mechanical assumptions. As pointed out before, timing in quantum mechanics is an experimentally almost unexplored field. A more specific question, that would be worthwhile to investigate with the improved experimental tools, is the occurrence of "dips" in the measured step-like structure of the ion-yield presented in chapter 4.1 also predicted by TDSE calculations.

• The shortest attosecond pulse

Isolating ever shorter attosecond pulses relying on visible femtosecond laser pulses is close to its limit. By approaching the single-cycle regime (1.5 cycles presented in this work), only a marginal further shortening of the driver pulses is possible. To create a distinctive broader spectral range associated with a single recollision (cut-off radiation) and hence the ability to create even shorter pulses than demonstrated in chapter 3.5 is therefore unfeasible. In contrast to the limit in the time domain, the spectral domain comprises a wide area of possible further developments. Employing new laser systems generating pulse energies clearly exceeding the mJ-level, the XUV radiation will be shifted towards higher photon energies enabling experimental studies on previously unexplored intermolecular- and atom-dynamics. In addition, the ability to tailor the attosecond pump to electronic transitions in molecules will allow selective studies on the often unclear dynamics that unfold subsequent to an excitation.

• Attosecond streaking spectroscopy

After the successful demonstration of the resolving power of the technique, the future work will focus on resolving a timing in shake-up systems like demonstrated for helium. Besides the unprecedented temporal resolution, the intrinsic timing in the measured traces is superior to many other time-resolved measurement schemes. Streaking spectroscopy is not limited to atomic targets but can be applied to molecules and solids and help to enlighten the time evolution of all sorts of phenomena that are fundamental for the interplay of matter. In order to study molecules and solids, a new generation of interferometric attosecond beamlines will allow shaping the laser pulse after the high-harmonic-generation. Shifting its carrier frequency to photon energies between 3-10 eV and shaping its time structure to drive transitions in the molecule efficiently and selectively, will provide novel powerful tools to investigate all sorts of charge dynamics that are the base of any chemical reaction.

• Intensity selective ionization

The presented ion detection scheme allows intensity selective studies on laser ionization above the saturation level for the first time. Measurements of ionization with short pulses, so far always limited by the volume effect, can clarify interesting questions. The existing theoretical treatments of laser ionization do not account for re-neutralization processes or, in particular in the context of few-cycle pulses, for the liberation of more than one electron per laser half-cycle. A new ion spectrometer imaging the charge state distribution in the laser focus with nm-resolution will open the field of ion-microscopy and support many open questions on the formation of ionized states in a laser field. Either the ionization up to highly charged states in short, intense laser pulses is suppressed or the electrons released during one half cycle necessarily have to be correlated. This bears important consequences for strong-field physics and possibly sheds light on the reliability of the so far assumed sequential ionization. As a more technological but also important aspect, the developed technique allows to investigate high-intense laser foci with a resolution by far better than the laser wavelength. To clarify a sub-wavelength intensity structure in the focused laser beam has major implications on almost any high-intensity laser applications like plasma-, small scale filamentation-, bubble acceleration and ionization-experiments.

Bibliography

1. M. Protopapas, C.Keitel, and P. Knight. Atomic physics with super-high intensity lasers. *Rep. Prog. Phys* **60**, 389 (1997).

2. J. Posthumus. The dynamics of small molecules in intense laser fields. *Rep. Prog. Phys.* **67**, 623 (2004).

3. J.H.Eberly, J.Javanainen and K.Rzazaewski. Above-threshold ionization. *Phys. Rep.* **204**, 331-383 (1991).

4. B. Sheehy and L. F. DiMauro. Atomic and Molecular Dynamics in Intense Optical Fields. *Annu. Rev. Phys. Chem.* **47**, 463 (1996).

5. T. Brabec and F. Krausz. Intense few-cycle laser fields: Frontiers of nonlinear optics. *Rev. Mod. Phys*. 72, 545 (2000).

6. N. B. Delone and V. P. Krainov. Multiphoton Processes in Atoms. Springer-Verlag (1994).

7. G. Mainfray and C. Manus. Multiphoton ionization of atoms. *Rep. Prog. Phys.* **54,** 1333 (1991).

8. P. Agostini, F. Fabre, G. Mainfray, G. Petite, N. K. Rahman. Free-Free transitions Following Six-Photon Ionization of Xenon Atoms. *Phys. Rev. Lett.* **42,** 1127 (1979).

9. Y. Gontier and M. Trahin. The role played by the level-shift operator in above-threshold ionisation. *J. Phys. B: At. Mol. Opt. Phys*. **13,** 4383 (1980).

10. L. V. Keldysh. Ionization in the field of a strong electromagnetic wave. *Sov. Phys. JETP* **20,** 1307 (1965).

11. F. Faisal. Multiple Absorption of Laser Photons by Atoms. *J. Phys. B: At. Mol. Opt. Phys.* **6,** L89 (1973).

12. H. R. Reiss. Effect of an intense electromagnetic field on a weakly bound system. *Phys. Rev. A* **22,** 1786 (1980).

13. M. V. Ammosov, N. B. Delone, and V. P. Krainov. Tunnel ionization of complex atoms and atomic ions by an alternating electromagnetic field. *Sov. Phys. JETP* **64**, 1191 (1986).

14. S. Augst, D.D. Meyerhofer, D. Strickland, S.L. Chin. Laser ionization of noble gases by Coulomb-barrier suppression. *J. Opt. Soc. Am. B* **8**, 858 (1991).

15. C. Winterfeldt, C. Spielmann, and G. Gerber. Optimal control of high-harmonic generation. *Rev. Mod. Phys*. **80**, 225 (2008).

16. J. Seres, E. Seres *et al.* Laser technology: Source of coherent kiloelectronvolt X-rays. *Nature* **433**, 596 (2005).

17. R. Landauer, Th. Martin. Barrier interaction time in tunneling. *Rev. Mod. Phys.* **66**, 217 (1994)

18. E.H. Hauge, J.A. Stoevneng. Tunneling times: a critical review. *Rev. Mod. Phys.* **61**, 917 (1989).

19. P. Corkum. Plasma perspective on strong-field multiphoton ionization. *Phys. Rev. Lett.* **71**, 1994-1997 (1993).

20. M. Lewenstein, P. Balcou, M. Y. Ivanov, A. L'Huillier, P. Corkum. Theory of high-harmonic generation by low-frequency laser fields. *Phys. Rev. A* **49**, 2117-2132 (1994).

21. P. Agostini, L. DiMauro. The physics of attosecond light pulses. *Rep. Prog. Phys* **67**, 6, 813-855 (2004).

22. A. Gordon, F. Kärtner. Scaling of kev hhg photon yield with drive wavelength. *Opt. Exp.* **13**, 8, 2941-2947 (2005).

23. J. Tate *et al*. Scaling of Wave-Packet Dynamics in an Intense Midinfrared Field. P*hys. Rev. Lett.* 98, 013901 (2007).

24. B. Shan, Z. Chang. Dramatic extension of the high-order harmonic cutoff by using a long-wavelength pump. *Phys. Rev. A* **65**, 011804(R) (2002).

25. K. Schiessl, K. Ishikawa, E. Persson, J. Burgdörfer. Quantum path interference in the wavelength dependence of high-harmonic generation. *Phys. Rev. Lett.* **99** (25) (2007).

26. T. Ditmire, J.K. Crane, H. Nguyen, L.B. DaSilva, M.D. Perry. Energy-yield and conversion-efficiency measurements of high-order harmonic radiation. *Phys. Rev. A* **51**, 2 (1995).

27. T. Hänsch. A proposed sub-femtosecond pulse synthesizer using separate phaselocked laser-oscillators. *Opt. Commun.* **80**, 1, 71-75 (1990).

28. G.Farkas, G. Toth. Proposal for attosecond light-pulse generation using laser-induced multiple-harmonic conversion processes in rare-gases. *Phys. Lett. A*, **168**, 5-6, 447-450 (1992).

29. Ph. Antoine, B. Piraux *et al.*Generation of ultrashort pulses of harmonics. *Phys. Rev. A* **54**, R1761-1764 (1996).

30. P. Tzallas, D. Charalambidis *et al.* Direct observation of attosecond light bunching. *Nature* **426** (6964), 267-271 (2003).

31. T. Pfeifer, D. Walter, C. Winterfeldt, C. Spielmann, and G. Gerber. Controlling the spectral shape of coherent soft x-rays. *Appl. Phys. B* **80**, 277-280 (2005).

32. J. Itatani, F. Quéré, G. L. Yudin, M. Yu. Ivanov, F. Krausz and P.B. Corkum**.** "Attosecond Streak Camera". *Phys. Rev. Lett*. **88**, 173903 (2002).

33. M. Drescher, M. Hentschel, R. Kienberger, G. Tempea, C. Spielmann *et al.* X-ray Pulses Approaching the Attosecond Frontier. *Science* **291**, 1923-1927 (2001).

34. R. Kienberger, E. Goulielmakis, M. Uiberacker, A. Baltuška, V. S. Yakovlev *et al.* Atomic transient recorder. *Nature* **427**, 817-821 (2004).

35. R. Kienberger et al. Steering Attosecond Electron Wave Packets with Light. *Science* **297**, 5584, 1144-1148 (2002).

36. T. Fuji, J. Rauschenberger, A. Apolonski, V. S. Yakovlev, G. Tempea *et al.* Monolithic carrier-envelope phase-stabilization scheme. *Opt. Lett.* **30**, 332-334 (2005).

37. J. Rauschenberger, T. Fuji, M. Hentschel, A.-J. Verhoef, T. Udem *et al.* Carrier-envelope phase-stabilized amplifier system. *Laser Phys. Lett.* **3**, 37-42 (2006).

38. T. Fuji, J. Rauschenberger, C. Gohle, A. Apolonski, T. Udem *et al.* Attosecond control of optical waveforms. *New J. Phys.* **7**, 116 (2005).

39. C. Gohle, J. Rauschenberger, T. Fuji, T. Udem, A. Apolonski *et al.* Carrier envelope phase noise in stabilized amplifier systems. *Opt. Lett.* **30**, 2487-2489 (2005).

40. A.L. Cavalieri, E. Goulielmakis, B. Horvath, W. Helml, M. Schultze, M. Fieß, V. Pervak, L. Veisz, V.S. Yakovlev, M. Uiberacker, A. Apolonski, F. Krausz and R. Kienberger. Intense 1.5-cycle near infrared laser waveforms and their use for the generation of ultra-broadband soft-x-ray harmonic continua. *New J. Phys.* **9,** 242.

41. V. Pervak, A. V. Tikhonravov, M. K. Trubetskov, S. Naumov, F. Krausz *et al.* 1.5-octave chirped mirror for pulse compression down to sub-3 fs. *Appl. Phys. B* **87**, 5-12 (2007).

42. C. Rullière (editor). Femtosecond Laser Pulses: Principles and Experiments. Springer, New York, USA (2005), second edition.

43. D. Kane, R. Trebino. Characterization of arbitrary femtosecond pulses using frequency-resolved optical gating. *IEEE J. Quantum Electron.* **29**, 571-579 (1993).

44. T. Udem, J. Reichert, R. Holzwarth, T. W. Hänsch. Accurate measurement of large optical frequency differences with a mode-locked laser. *Opt. Lett.* **24**, 881-883 (1999).

45. M. Zimmermann, C. Gohle, R. Holzwarth, T. Udem, T. W. Hänsch. Optical clockwork with an offset-free difference-frequency comb: accuracy of sum- and difference-frequency generation. *Opt. Lett.* **29**, 310-312 (2004).

46. M. Hentschel, R. Kienberger, C. Spielmann, G. A. Reider, N. Milosevic *et al.* Attosecond metrology. *Nature* **414**, 509-513 (2001).

47. E. Goulielmakis, M. Uiberacker, R. Kienberger, A. Baltuška, V. S. Yakovlev *et al.* Direct Measurement of Light Waves. *Science* **305**, 1267-1269 (2004).

48. M. Schnürer, Z. Cheng, M. Hentschel, F. Krausz, T. Wilhein, D. Hambach, G. Schmahl, M. Drescher, Y. Lim, U. Heinzmann. Few-cycle-driven XUV laser harmonics: generation and focusing. *Appl. Phys. B* **70** (7), 227 (2000).

49. L. Poletto, G. Tondello, P. Villoresi. High-order laser harmonics detection in the EUV and soft x-ray spectral regions. *Rev. Sci. Instr.* **72**, 2868 (2001).

50. A. Wonisch, U. Neuhäusler, N. M. Kabachnik, T. Uphues, M. Uiberacker, V. Yakovlev, F. Krausz, M. Drescher, U. Kleineberg, and U. Heinzmann. Design, fabrication, and analysis of chirped multilayer mirrors for reflection of extreme-ultraviolet attosecond pulses. *Applied Optics*, **45**, 17, 4147-4156 (2005).

51. F. Lindner, G.G. Paulus, H. Walther, A. Baltuska, E. Goulielmakis, M. Lezius, and F. Krausz. Gouy phase shift for few-cycle laser pulses. *Phys. Rev. Lett*. **92**, 113001 (2004).

52. T. Harada, H. Sakuma, K. Takahashi, T. Watanabe, H. Hara, and T. Kita. Design of a High-Resolution Extreme-Ultraviolet Imaging Spectrometer with Aberration-Corrected Concave Gratings, *Appl. Opt*. **37**, 6803-6810 (1998).

53. N. Nakano, H. Kuroda, T. Kita, and T. Harada. Development of a flat-field grazing-incidence XUV spectrometer and its application in picosecond XUV spectroscopy. *Appl. Opt*. **23**, 2386-(1984).

54. The Center for X-Ray Optics at the Lawrence Berkeley National Laboratory; *http://www-cxro.lbl.gov/*.

55. Time-of-flight (TOF) Spectrometers manufactured by Stefan Kaesdorf. Geräte für Forschung und Industrie. *http://www.kaesdorf.brd.de/*.

56. M. Wagner, H. Schröder. A novel 4 grid ion reflector for saturation of laser multiphoton ionization yields in a time-of-flight mass-spectrometer *Int. J. Mass Spectrom.* **128**(1-2), 31-45 (1993).

57. G. Sansone, E. Benedetti, F. Calegari, C. Vozzi, L. Avaldi *et al.* Isolated Single-Cycle Attosecond Pulses. *Science* **314**, 443-446 (2006).

58. P. Paul, E. Toma, P. Breger, G. Mullot, F. Auge, P. Balcou, H. Muller, P. Agostini. Observation of a Train of Attosecond Pulses from High Harmonic Generation. *Science* **292** 1689–1692 (2001).

59. A.L. Huilier, P. Balcou. High-order harmonic generation in rare gases with a 1-ps 1053-nm laser. *Phys. Rev. Lett*. **70**, 774-777 (1993).

60. P. Johnsson et al. Attosecond Electron Wave Packet Dynamics in Strong Laser Fields . *Phys. Rev. Lett*. **95**, 013001 (2005).

61. B. Henke, E. Gullikson, J. Davis. X-ray interactions: photoabsorption, scattering, transmission, and reflection at E = 50-30,000 eV, Z = 1-92. *At. Data Nucl. Data Tables* **55** 349 (1993).

62. A.-S. Morlens, R. López-Martens, O. Boyko, P. Zeitoun, P. Balcou, K. Varjú, E. Gustafsson, T. Remetter, A. L'Huillier, S. Kazamias, J. Gautier, F. Delmotte and M.-F. Ravet. Design and characterization of extreme-ultraviolet broadband mirrors for attosecond science. *Opt. Lett*. **31**, 1558 (2006).

63. T. Morishita, S. Watanabe, C. D. Lin. Attosecond Light Pulses for Probing Two-Electron Dynamics of Helium in the Time Domain. *Phys. Rev. Lett.* **98**, 83003 (2007).

64. M. Schultze, E. Goulielmakis, M. Uiberacker, M. Hofstetter, J. Kim, D. Kim, F. Krausz and U. Kleineberg. Powerful 170-attosecond XUV pulses generated with few-cycle laser pulses and broadband multilayer optics. *New J. Phys*. **9** 243 (2007).

65. Y. Mairesse and F. Quéré, Frequency-Resolved Optical Gating for Complete Reconstruction of Attosecond Bursts. *Phys. Rev.* A, **71** (2005) 0011401(R).

66. F. Quéré, Y. Mairesse and J. Itatani. Temporal characterization of attosecond xuv fields. *Journal of Modern Optics* **52**, 339-360 (2005).

67. M. Kitzler, N. Milosevic, A. Scrinzi, F. Krausz, and T. Brabec. "Quantum theory of attosecond XUV pulse measurement by laser dressed photoionization. *Phys. Rev. Lett.* **88**, 173904 (2002).

68. J. Gagnon, E. Goulielmakis, V. Yakovlev. Advances toward the accurate FROG characterization of attosecond pulses from streaking measurements. Submitted to *NJP* (2008).

69. F. Lindner, M. G. Schätzel, H. Walther, A. Baltuška, E. Goulielmakis *et al.* Attosecond Double-Slit Experiment. *Phys. Rev. Lett.* **95**, 040401 (2005).

70. M. Uiberacker, T. Uphues, M. Schultze, A.-J. Verhoef, V. S. Yakovlev *et al.* Attosecond real-time observation of electron tunnelling in atoms. *Nature* **446**, 627-632 (2007).

71. L. V. Keldysh. Ionization in field of a strong electromagnetic wave. *Soviet Physics JETP* **20**, 1307-1314 (1965).

72. G. L. Yudin, M.Yu Ivanov. Nonadiabatic tunnel ionization: looking inside a lasercycle. *Phys. Rev. A* **64**, 013409 (2001).

73. M. F. Kling, C. Siedschlag, A.-J. Verhoef, J. I. Khan, M. Schultze *et al.* Control of Electron Localization in Molecular Dissociation. *Science* **312**, 246-248 (2006).

74. P. B. Corkum, F. Krausz. Attosecond science. *Nat. Phys.* **3**, 381-387 (2007).

75. P. B. Corkum. A plasma perspective on strong field multiphoton ionization. *Phys. Rev. Lett.* **71**, 1994–1997 (1993).

76. D. Zeidler *et al.* Controlling attosecond double ionization dynamics via molecular alignment. *Phys. Rev. Lett.* **95**, 203003 (2005).

77. M. Weckenbrock *et al.* Electron–electron momentum exchange in strong field double ionization. *Phys. Rev. Lett.* **91**, 123004 (2003).

78. U. Becker, D.A. Shirley. *VUV and Soft-X-Ray Photoionization*. Plenum Press, New York (1996)

79. V. I. Matveev and É. S. Parilis. Shake-up processes accompanying electron transitions in atoms. *Sov. Phys. Usp.* **25** 12, 881-897 (1982).

80. L. A. A. Nikolopoulos, P. Lambropoulos. Time-dependent theory of double ionization of helium under XUV radiation. *J. Phys. B* **40** 7, 1347-1357(11) (2007).

81. P. A. Heimann, U. Becker, H. G. Kerkhoff, B. Langer, D. Szostak, R. Wehlitz, D. W. Lindle, T. A. Ferrett, D. A. Shirley. Helium and neon photoelectron satellites at threshold. *Phys. Rev. A* **34**, 3782 (1986).

82. T. Åberg. Theory of X-Ray Satellites. *Phys. Rev.* **156**, 35-41 (1967).

83. P. R. Woodruff, J. A. R. Samson. Measured Cross Sections for Photoionization of Ground-State He to HE$^+$ (n=2). *Phys. Rev. Lett.* **45**, 110-113 (1980).

84. K. Yamakawa et al. Many-Electron dynamcis of a Xe Atom in Strong and Superstrong Laser Fields. *Phys. Rev. Lett.* **92**, 123001 (2004).

85. S. Larochelle, A. Talebpour and S. L. Chin. Non-sequential multiple ionization of rare gas atoms in a Ti:Sapphire laser field. *J. Phys. B* **31**, 1201 (1998).

86. M. A. Walker, P. Hansch, L. D. Van Woerkom,. Intensity-resolved multiphoton ionization: circumventing spatial averaging. *Phys. Rev. A* **57**, R701–R704 (1998).

87. W. A. Bryan *et al*. Atomic excitation during recollision-free ultrafast multi-electron tunnel ionization. *Nature Physics* **2,** 379-383 (2006).

88. J. Strohaber, C.J.G.J. Uiterwaal. In Situ measurement of Three-Dimensional Ion Densities in Focused Femtosecond Pulses. *Phys. Rev. Lett.* **100**, 023002 (2008).

89. E. Goulielmakis, M. Schultze, M. Hofstetter, V.S. Yakovlev, J. Gagnon, M. Uiberacker, A.L. Aquila, E.M Gullikson, D.T. Attwood, R. Kienberger, F. Krausz, U. Kleineberg. Single-cycle nonlinear optics. Submitted to *Science*.

90. E. Goulielmakis, S. Koehler, B. Reiter, M. Schultze, A.J. Verhoef, E. Serebryannikov, A.M. Zheltikov and F. Krausz. Ultra-broadband, coherent light source baesd on self-channeling of few-cycle pulses in He. Submitted to *Optics Letters*.

91. Th. Uphues, M. Schultze, M. F. Kling, M. Uiberacker, S. Hendel, U. Heinzmann, N. M. Kabachnik, M. Drescher. Ion.charge-state chronoscopy of cascaded atomic Auger decay. *New Journal of Physics* **10**, 2 (2008).

Ehrenwörtliche Erklärung

Die Promotionsordnung verlangt die Abgabe folgender, ehrenwörtlicher Erklärung:

Hiermit versichere ich an Eides statt, daß die vorliegende Arbeit mit keinen, außer dem betreuenden Hochschullehrer bekannten Hilfsmitteln selbstständig angefertigt wurde, und alle benutzten Hilfsmittel unter Angabe der Literaturstellen kenntlich gemacht sind.

19. April 2008   Martin Schultze

Die Redlichkeit verlangt die Angabe derer, ohne die ich diese Arbeit nicht hätte anfertigen können. Die folgende Aufführung umfasst die Personen, denen ich für ihre Unterstützung verbunden bin, sie ist notwendigerweise unvollständig und Ausdruck meiner Hoffnung auf Vergebung durch die ungerechterweise Unaufgeführten.

Danksagung

Ich danke Prof. Ferenc Krausz für die Möglichkeit in der von ihm geführten Gruppe am Max-Planck-Institut für Quantenoptik zu arbeiten und für seine unermüdlichen Anstrengung, für ideale Forschungsbedingungen zu sorgen – technologisch und menschlich.

Reinhard Kienberger danke ich für seine wohlwollende Unterstützung sowie Matthias Uiberacker, Eleftherios Goulielmakis und Thorsten Uphues für die mehr als angenehme Zusammenarbeit in den vergangenen drei Jahren im Labor und außerhalb. Vladislav Yakovlev und Justin Gagnon danke ich für die begeisterte Arbeit an der Analyse und Interpretation der experimentellen Daten.

Ich danke Prof. Ulf Kleineberg und Andreas Hofstetter für die Herstellung beinahe unzähliger Multilayer Spiegel und für ihr unentwegtes Streben nach optimierten Schichtsystemen um die Experimente bestmöglich zu unterstützen.

Hartmut Schröder danke ich für seinen Ideenreichtum im Umgang mit dem Reflektron-spektrometer im speziellen und der Physik im allgemeinen.

Weiterhin schulde ich aus einer Vielzahl von Gründen einer Vielzahl Personen meinen Dank, einige sind im folgenden aufgeführt:

Sasha Apolonski, Alois Böswald, Martin Centurion, Markus Fieß, Manfred Fischer, Takao Fuji, Ullrich Graf, Ivanka Grguras, Martin Gruber, Harald Haas, Nikolay Kabachnik, Matthias Kling, Thomas Metzger, Jens Rauschenberger, Peter Reckenthäler, Walther Ritt, Claudia Schenker, Karl Schmid, Thomas Strobl, Simon Trinkgeld, Aart Verhoeff, Monika Wild, ...

Curriculum Vitae

Martin Schultze
Max-Planck-Institut für Quantenoptik
Hans-Kopfermann-Str. 1
85748 Garching
Tel.: 0049 89 32905236
Martin.Schultze@mpq.mpg.de
www.attoworld.de

Personal data

Date of birth: 11.03.1979
Place of birth: Bad Hersfeld
Citizenship: German
Marital status: unmarried

Education

09/2004 – present	Graduate student in the Group of Prof. Krausz at Max-Planck-Institute of Quantum Optics, Garching, Germany
10/2003 – 05/2004	Diploma thesis in the Group of Prof. Esslinger at Swiss Federal Institute of Technology (ETH), Zurich, Switzerland Subject: *Waveguide for Atoms*
10/1999 – 10/2003	Undergraduate studies in physics at Swiss federal Institute of Technology (ETH), Zurich, Switzerland
06/1998	Abitur (high school graduation) in Bad Hersfeld

Extra-educational experience

10/2003 – 05/2004	Undergraduate teaching assistance at the Physics Department, ETH Zurich for the course "Physics for mechanical engineers"
08/2001 – 06/2003	Graduate assistant at the Institute for Building Materials, Corrosion and Durability, ETH, Zurich Subject: *Optimization of an scanning electro-chemical microscope (SECM)*
03/2000 – 04/2000	Internship at ISEL automation www.isel.de
06/1999 – 08/1999	Internship at Logosol, Inc. Sunnyvale, USA. www.logosolinc.com
07/1998 – 05/1999	Military service